# Structural Analysis of CavAb,
# a Prokaryotic Voltage-Gated Calcium Channel

Teresa Mae Swanson

A dissertation submitted in partial fulfillment
of the requirements for the degree of

Doctor of Philosophy

University of Washington

2016

Reading Committee:

William A. Catterall
Ning Zheng
William Zagotta

Program Authorized to Offer Degree:

Department of Pharmacology

University of Washington

## ABSTRACT

# Structural Analysis of CavAb, a Prokaryotic Voltage-Gated Calcium Channel

Teresa Mae Swanson

Chair of the Supervisory Committee:

Professor William A. Catterall
Pharmacology

Voltage-gated calcium channels are large membrane proteins that coordinate the movement of calcium into and out of the cell in response to changes in membrane potential, mediating signaling processes such as muscle contraction and synaptic transmission. We used CavAb, a bacterial calcium channel, as a structural model for three Cav channel characteristics; ion selectivity, drug binding, and disease mutations. First, CavAb reveals three binding sites for hydrated calcium within the selectivity filter of the channel, confirming the theory of a "knock-off" mechanism of calcium selectivity. Second, CavAb mimics mammalian Cav antagonist binding properties, providing visualization of bound drug molecules and potential direction for structure based drug design. Finally, the addition of Timothy Syndrome disease mutations into CavAb shows small conformational changes, highlighting the potential importance of channel regulation by lipids. Even though CavAb is a distant ancestor to the mammalian calcium channels, it has proven to be a valuable tool for answering classic calcium channel questions.

# TABLE OF CONTENTS

# ACKNOWLEDGEMENTS

First and foremost, a thank you to my advisors, Bill Catterall and Ning Zheng, who gave me this space to grow as an academic and scientist. Their guidance and experience provided an unending wealth of knowledge to learn from and for that, I am grateful. I would also like to thank their many lab members for their support, and conversation. They made every day in lab inclusive, enjoyable, and real.

My sincerest appreciation to Gilbert Martinez, without whom I could not have survived. Gilbert started as a mentor and will forever be a friend. He quickly learned how to push my buttons and encourage me beyond my own expectations. I have no doubt that his unwavering diligence has helped me complete this degree in a timely fashion, despite my best efforts to procrastinate. He was kind enough to sit through my complaints and excuses, and nurse me back to happiness with beer and whiskey when necessary. I cannot imagine a more supportive mentor, and am honored to have worked by his side. He won’t admit it, but he is truly one of the good guys.

Bill Zagotta’s love of all things science was always a breath of fresh air, Sharona Gordon is an inspiration to women everywhere. I always walked out of her office feeling confident and ready to take on the world. To Ron Stenkamp, who so patiently put up with the shenanigans of Shannon and I in reciprocal space, and the healthy dose of realism every academic should possess. Thank you also to the Department of Pharmacology administration staff, and particularly Diane Schulstad, for being a bright light in that dreary old hallway.

Shannon Nangle, who has looked past my carnivorous diet and seen the true person inside. I'm certain her accomplishments will extend beyond this world, and I'm over the moon to watch her get achieve them. My close lab mates, Eedann McCord and Rachael Stein, who are some of the most intelligent, creative and grounded women I've ever met—they also know the best happy hours, sushi or otherwise. Christine Cheah, for encouraging my chocolate habits. Karthik Ramanadane, who could not have annoyed me more at first, but whose positivity is infectious.

My parents, Mark and Carol Swanson, for teaching me to question everything (much to their frustration, I'm sure). My sister, Kelsey Swanson, for reminding me to keep my logical life artistic. My cousins, Kat Traxler and Nikki Freeman, for the constant stream of hilarity, love and companionship. Lisa Chesner, that college lab mate who I never could find a replacement for, and never will. Chris Carhart, who kept me exercised and well-fed. Charlie and Ailea Boisner who lured me away from the Midwest, you two are a riot (and I'm never going back!). To Miss Karly Smith, and her clan- Ezrealla, Savion, Aeris, and Avionah. Your hard work and dedication are incredible. Your girls are the future generation of thinkers, and their future is bright. I will always cherish the memories of Ezi in lab with me, and continue to be astounded by her wisdom, individuality and spunk. And finally, to Richard Davalos, the man who makes me smile every day, no matter what I'm going through. Thank you from now to the end of time, for your acceptance, partnership, compassion, and stability. You're more than a dream come true.

# DEDICATION

To the future of scientific discovery, may it be accessible to anyone and everyone.

And to our future generations, may they achieve beyond our wildest dreams.

*"What if you get it wrong?"*

*"Well, you have to wait for somebody who gets it right," said Luna.*

*"That way you learn, you see?"*

*"Yeah... Trouble is, we can't really afford to wait for anyone else, Luna."*

*"No, I see what you mean"' said Luna seriously.*

*"Well then, I think the answer is that a circle has no beginning."*

*"Well reasoned," said the voice, and the door swung open.*

*-J.K. Rowling, Harry Potter and the Deathly Hallows*

# 1 INTRODUCTION

## 1.1 Excitable cells

Communication between cells can happen in a variety of chemical, mechanical and electrical ways. Chemical communication is important for processes such as hormone regulation or gene expression, while mechanical communication is important for hearing or sensation. Effective regulation of cardiac function, muscle contraction and synaptic transmission, relies on electrical signals between cells, to name a few. Cells that use electricity, or changes in the charge across their cell membrane are known as excitable cells, and are present throughout the body.

Excitable cells are able to sense and respond to the charge across the cell membrane because of the presence of proteins in the membranes called voltage-gated ion channels (Hille, 1992). These channels allow ions to flow from the extracellular space to the cytoplasm modulated by the charge across the cell membrane, or the membrane potential. There are three main classes of voltage-gated ion channels (VGIC); potassium, sodium and calcium, which are named for which ions they allow through the membrane. These channels are related evolutionarily, but the potassium channels are most diverse and distant from the sodium and calcium channels that this thesis will focus on (Figure 1.1).

## 1.2 The Cardiac Action Potential

The pulsing electrical signal used to communicate between excitable cells is called the action potential (Hille, 1992). This signal is transmitted down nerves to allow information to travel quickly from the periphery to the central nervous system. All action potentials are self-propagating and regenerative. Once the action potential reaches its destination, the electrical signal is converted into a chemical one.

The propagation of the action potential is localized to the cellular membrane, and is a concert of different voltage-gated ion channels opening and closing in order to change the ionic concentrations, and therefore the electrical charges across the cell membrane. Resting membrane potentials in mammalian cells range from -40mV to -100mV, indicating a positive charge outside and negative charge inside the cell. The membrane potential will change as ions move across the membrane through ion channels. Each ion channel has a threshold potential that the membrane must reach for it to open.

The first channels that open in response to a change in membrane potential are the sodium channels, which then allow positive sodium ions to flow into the cell (Figure 1.2). This raises the membrane potential very quickly, called depolarization, triggering other ion channels to open as the potential reaches their thresholds. The sodium channels inactivate quickly, and if calcium channels are present, they will be triggered next which allows calcium to enter the cell and act as a secondary messenger. Potassium channels are the final ion channels that open, and these channels allow positive potassium ions to flow from the inside of the cell to the outside, thus helping return the membrane potential to the resting state, or repolarization. This repolarization often overshoots the resting membrane potential. Different proteins called ionic pumps, can exchange sodium inside the cell for potassium outside the cell to maintain concentration gradients. The specifics of how the action potential functions are dependent on the subtype of ion channels that are present in the cells carrying the electrical signal.

## 1.3 Voltage-gated sodium channels

Research into voltage-gated sodium channels, Nav, began over 60 years ago with investigations into the electrical activity of the giant squid axon by Hodgkin and Huxley (Hodgkin & Huxley, 1952b; 1952a; 1952c). They showed that the electrical signal propagation along the axon was dependent on the voltage dependence of sodium current; experiments that are still taught in beginning physiology classes across the world. Soon after, it was hypothesized that sodium currents, as well as other ionic currents, were due to specific proteins in the membrane that were selective for sodium ions. Through a variety of investigations, different drugs and toxins were found to change the behavior of sodium channels (Catterall, 1980). These toxins lead to the discovery of the identity and purification of the sodium channel protein by photoaffinity labeling (Beneski & Catterall, 1980). They were functionally reconstituted (Catterall, 2012b) and subsequently cloned and sequenced (Catterall, 2005; 2012b). Sodium channels were shown to contain a large 24-transmembrane segment $\alpha$-subunit, as well as smaller associated $\beta$ subunits which are related to known cell adhesion proteins.

It has since been discovered that there are 10 sodium channel $\alpha$ subunit genes, which produce the proteins Nav1.1 through Nav1.9 and Nav1.x. The protein expression patterns vary, but are found throughout the body with four main isoforms in the central nervous system (Nav 1.1, 1.2, 1.3 and 1.6), three in the periphery (Nav1.7, 1.8 and 1.9), one in the skeletal muscle (Nav1.4) and one in the heart (Nav1.5) (Catterall, 2005). Nav1.x is involved in salt-sensing and is found in the central nervous system (Watanabe, Fujikawa, & Matsunaga, 2000). There are four known β subunit genes, which don't seem to be targeted to specific α subunits.

Physiological roles of sodium channels are centered around the initiation of an action potential. The variety in sequence and location of the Navs determines which type of signal the action potential propagates. For example, in sensory neurons, Nav1.7 is associated with pain transmission, and in the heart, Nav1.5s role in the cardiac action potential keeps the heart beating (Catterall, 2005; 2012b).

### 1.4 Voltage-gated calcium channels

While calcium channels are similar in topography and basic biophysical properties to sodium channels, their physiological role is quite different. Calcium ions that flow through the channels not only act to change the membrane potential as sodium does, but more importantly serve as secondary messengers inside of a cell. Cellular concentrations of calcium remain low throughout the cytoplasm. This allows calcium to be a fast acting signal when calcium concentrations increase locally, and translates electrical signals into chemical ones within the cell. Calcium is used as a messenger to trigger a wide variety of processes including synaptic transmission and muscle contraction, as well as hormone release, enzyme regulation and even gene expression (Catterall, 2012a).

There are 10 different Cavs, grouped by their calcium current properties. The L-type channels are Cav1.1-1.4, characterized by their high voltage of activation and slow voltage-dependent inactivation (Catterall, 2012a). These channels are primarily found in the muscle tissues such as the cardiac, smooth and skeletal muscles. They're targeted by many clinically used drugs, including the phenylalkylamines, dihydropyridines and benzothiazepines. These drugs are used to treat hypertension and arrhythmias, among other things (Catterall, 2011).

The Cav2.1, 2.2 and 2.3 channels are mainly neuronal in nature and are responsible for neurotransmitter release (Catterall, 2011; Hille, 1992). Their currents are described as N-, P/Q- and R-type, respectively and tend to have intermediate properties between the Cav1.x and Cav3.x channels. These channels are the main targets of spider toxins, but their currents vary quite a bit.

The Cav3.1, 3.2 and 3.3 channels are possibly the least studied group of calcium channels and are characterized by their T-type currents, which are transient (Catterall, 2011; Hille, 1992). These channels close quickly and open repetitively, and are thus involved in pacemaker activity. Specific pharmacological blockers have been difficult to identify, but not due to lack of effort; these channels play prominent roles in seizure activity and migraines.

## 1.5 Ion channel structure and function

Sodium and calcium channels share an overall fold of their α subunit, comprised of about 2000 amino acids and an astounding 24 transmembrane helices. These helices are separated into four homologous domains, each with six transmembrane segments. Each domain is then separated even further into a voltage sensing domain consisting of segments one through four, S1-S4, and a pore domain formed with segments five and six, S5-S6, and the connecting P loop (Yu & Catterall, 2004) (Figure 1.3). The voltage-sensing and pore domains are separated by a helical S4-S5 linker. Potassium channels are slightly different in that their α1 subunit is instead a tetramer of a single subunit that contains the voltage-sensing and pore domains.

Each pore domain is situated around the central axis of the protein, with the intervening P-loops coming close together, as well as the bottoms of the S6 segments crossing each other in an inverted teepee fashion (Hille, 1992). These characteristics form important functional regions of the proteins. The central axis forms the pore and central cavity of the channel, where the ions pass through to traverse the membrane and enter the cell. The close proximity of the P loops creates a narrow neck on the extracellular side of the pore called the selectivity filter. The amino acids in these loops help select which ion will be allowed to pass through the channel, the namesake characteristic for each type of channel. Just below the selectivity filter is a large central cavity that the ions must pass through before reaching the "top" of the teepee, or what's known as the activation gate.

Each voltage-sensing domain (VSD) is located around the outside of the pore domain in a domain-swapping fashion (Hille, 1992; Payandeh, Scheuer, Zheng, & Catterall, 2011a). Each VSD is closely associated with the pore domain of the next homologous subunit or domain in the amino acid sequence, not the one within its own section. The defining structure of the voltage-sensing domains is the S4 segment, which contains several positively charges arginine residues that can sense the electrical charge on the membrane. The S4 will move either up or down in the membrane according to the attraction/repulsion of the charges. This movement is coupled to the pore domain and is what controls the opening and closing of the activation gate through the S4-S5 linker. This linker is helical and lies horizontally in the membrane, connecting the bottom of the S4 helix to the bottom of the S5 of the pore domain.

At rest, the positive charge outside the cell will repel the positive charges on the S4 segment of each voltage-sensing domain, causing it to remain low in the membrane, positioned towards the intracellular space. When the S4 segment is low, the activation gate is closed-the S6 segments are crossed-and the channel is not passing ions. When the charge outside the membrane is negative, the S4 will be pulled through the membrane towards the extracellular space. The change in structure is transferred to the pore domain and the activation gate twists open, allowing ions to flow through into the cell.

Both mammalian sodium and calcium channels require additional subunits to regulate the function of the $\alpha 1$ subunit (Hille, 1992). For sodium channels, the $\beta$ subunits are transmembrane glycoproteins that fine tune channel gating. Calcium channels contain a transmembrane glycoprotein $\alpha_2\delta$ as well as intracellular $\beta$ subunits and sometimes $\gamma$ subunits. The $\alpha_2\delta$ subunit affects expression and gating of the Cav channel, while the $\beta$ changes channel expression and the $\gamma$ subunit doesn’t seem to be involved in protein trafficking or regulation.

Both the intra- and extracellular loops of Cavs have post-translational modification sites for glycosylation and phosphorylation. The intracellular domain of the calcium channels houses many different structures including protein-interaction domains; domains for $\beta$-subunit binding, AKAP binding (A-kinase anchoring protein), and calmodulin binding.

## 1.6 Ion Channels and Disease

Diseases that are caused by disruptions to ion channel genes are called channelopathies (Catterall, 2012a). When mutations arise in sodium channel $\alpha$ subunits, the resulting diseases are tissue dependent. Mutations in skeletal muscle channels lead to periodic paralyses, which are characterized by periodic muscle weakness, while mutations in cardiac muscles lead to Long QT syndrome, characterized by erratic heartbeats. When the $\beta$ subunits are mutated, seizures are often seen. A common trend among channelopathies is that mild mutations in the channels will lead to diseases with mild symptoms, but more severe mutations or even truncations will lead to more severe diseases and comorbidities. One well-known epileptic channelopathy is Dravet syndrome (Catterall, 2012a), in which Nav1.1 is truncated and expression is affected in inhibitory neurons. Dravet syndrome has a lot of severe comorbidities including autism and anxiety, which reflect the severe nature of the truncation in the sodium channel.

Calcium channel mutations also result in a wide variety of channelopathies, depending on the location of channel expression. In muscles, calcium channelopathies can lead to episodic ataxia, periodic paralysis or spinocerebellar ataxia. In neurons, mutations can cause migraines. As with sodium channelopathies, it seems that the more severe the mutation or truncation, the more severe the disease manifests. Mild mutations will cause less severe ataxias, while truncations will produce severe ataxia or degeneration.

One example of a severe mutation in calcium channels is Timothy Syndrome (Splawski, Timothy, Priori, & Napolitano, 1993), in which the activation gate of Cav1.2 gains a charged amino acid. Timothy Syndrome causes a loss of inactivation of the calcium channel and leads to Long QT syndrome along with syndactyly and autism spectrum disorder. Timothy Syndrome will be discussed more in depth in Chapter 5.

## 1.7 Prokaryotic Channels

The first prokaryotic sodium channels studied was NaChBac, discovered by Clapham and colleagues in 2001 (Navarro, Xu, Yue, Shi, & Clapham, 2001). NaChBac and other prokaryotic channels (BacNavs) are the ancestors to both the mammalian Nav and Cav channels. Sequence analysis has shown that although BacNavs are sodium selective, their overall sequence is more similar to Cav channels than Nav channels (Yu & Catterall, 2004). Structurally, BacNavs are much simpler than their mammalian descendants, they contain only the α1 subunit, which in this case is a homotetramer of a single voltage-sensing domain and pore domain (Figure 1.3). Functionally, the kinetics of bacterial channels are slower than Nav channels, which is also the case for Cav channels.

BacNavs do not require other subunit proteins to function properly, such as the β, δ, or γ subunits seen associated with mammalian sodium or calcium channels (Navarro et al., 2001). Prokaryotic channels do not seem to be modified post-translationally, and contain vastly smaller intracellular and extracellular loops. The bacterial C-terminal domain is comprised mostly of a four-helix bundle extending directly into the cytoplasm, which is vastly different from the mammalian channels that tend to have more globular C-terminal structures.

High-resolution structures have been reported for a variety of both prokaryotic and eukaryotic voltage-gated potassium channels (Zhou & MacKinnon, 2003) over the last 15 years, but the structures of voltage-gated Nav and Cav channels have remained elusive. It is only within the last five years that the structure of a BacNav channel NavAb has been solved to 2.7 Å, among other BacNav structures (McCusker et al., 2012; Payandeh, El-Din, Scheuer, Zheng, & Catterall, 2012a; Payandeh, Scheuer, Zheng, & Catterall, 2011b; Shaya et al., 2014; Zhang et al., 2012).

## 1.8 NavAb Structure

Published in 2011 (Payandeh, Scheuer, Zheng, & Catterall, 2011a), the NavAb structure revealed the relative organization of the VSD and pore domains to be as expected, with the VSDs surrounding the pore in a domain-swapping fashion—the VSD of one subunit is associated with the pore domain of the next subunit (Figure 1.4). The homotetramer is symmetric, with the S5 and S6 helices lining the central pore. The S4-S5 linker is helical, but runs perpendicular to the membrane, connecting the bottom of the S4 helix with the beginning of the S5 helix, cutting across another subunits pore domain. In the NavAb structures, the S4 helix is sitting in a more extracellular position in the membrane that would mimic a positive charge inside the cell.

The pore domain of NavAb is in a closed state. Starting from the extracellular side, the channel has a funnel shape that leads to the top of conducting pore. The selectivity filter is lined by the side and main chains of the local amino acids, which are a part of the P-loop. The entire pore, through the selectivity filter and into the central cavity is water-filled, but separated from the intracellular space by the closed activation gate near the bottom of the S6 helices.

## 1.9 NavAb constructs

Two different constructs of NavAb have been crystallized, and a third is used for electrophysiological studies. The first construct published by Jian Payandeh was NavAb-I217C (Payandeh, Scheuer, Zheng, & Catterall, 2011a), where a cysteine mutation was introduced into the activation gate of the channel, which was more easily crystallized (Figure 1.4). This construct crystallizes most readily, and produces a nearly four-fold symmetrical structure, including the pore domain. To the naked eye, all four subunits of this channel are identical and arranged symmetrically around the conductance pathway of the pore. The C-terminal domain, specifically the final 45 residues, was not visible in this published structure, despite their presence in the crystallized protein. NavAb-I217C is reported to be in the pre-open open state; the S4 segment is raised in the membrane, presumably mimicking a positive charge on the outside of the cell membrane, the selectivity filter is available for ion binding, but the activation gate is closed and unable to pass ions to the intracellular space.

The second NavAb construct to be crystallized and published by Payandeh *et al.* was the wildtype NavAb, NavAb-WT (Payandeh, El-Din, Scheuer, Zheng, & Catterall, 2012b). This construct was more difficult to successfully crystallize and the data was of worse quality- specifically the crystal was twinned (see Chapter 4.3.4 for a discussion on twinning). The individual voltage-sensing domains of this construct were identical to NavAb-I217C, but there was a new asymmetry induced in the pore, which propagated to the orientation of the VSDs to the pore domain. The pore was now two-fold symmetric, and the selectivity filter was partially collapsed by movement of two S6 toward the pore axis and two away from it, making it no longer able to accommodate hydrated sodium ions. The activation gate was still closed, and the C-terminal domain of the construct still missing from the diffraction data. This collapsed selectivity filter was interpreted as the inactivated state of the channel.

The final construct of NavAb has yet to be crystallized, but is useful in the functional studies of NavAb, NavAb-N49K (El-Din, Martinez, Payandeh, Scheuer, & Catterall, 2013). This construct removes a functional characteristic referred to as “late slow inactivation” from NavAb, allowing for easier biophysical characterization by electrophysiology (Figure 1.5). Use-dependent inactivation is when the channel inactivates during successive pulses, and limits the frequency and duration of pulses able to be used in functional studies. NavAb-N49K also produces a +75 mV shift in the voltage-dependence of activation. All functional work associated with the structural studies in this thesis were done using NavAb-N49K and performed by Catterall lab member, Tamer Gamal El-Din, PhD.

### 1.10 NavAb as a model channel

NavAb was chosen as a model to structurally study voltage gated calcium channels for a few reasons. First, attempts at the crystallization of mammalian Nav channels have been unsuccessful and no structural data exists on the pore of these channels, but NavAb can be easily crystallized. Second, NavAb is easily manipulated by molecular biology, making mutational studies easier to access than more complicated channels. Third, previous computational models of Cav channels antagonists had been calculated using the bacterial potassium channels KcsA (Tikhonov & Zhorov, 2012) and KvAP, which are more evolutionarily distant from the mammalian channels than NavAb is. Fourth, NavAb shares an overall topology with Cav channels and the sequences are similar. As an ancestor protein to both Nav and Cav channels, NavAb provides a unique opportunity to structurally model mammalian channels with a crystallization method that is already known. Chapter II discusses how we used NavAb to create the calcium selective CavAb, which is used throughout this thesis.

### 1.11 Questions Addressed

This dissertation will explore three different ways that NavAb can act as a reasonable structural model for mammalian calcium channels. First, I will discuss creating CavAb from NavAb, and how we used structural biology to study the basic biophysics and biochemistry of calcium conduction through a calcium channel. Second, I will discuss drug binding to CavAb, describing how common cardiac medications such as verapamil and amlodipine bind to their calcium channels. Third, I will show how CavAb can be used to model Timothy Syndrome, a disease caused by a point mutation in the activation gate of the human Cav1.2 channel.

All functional work associated with the structural studies in this thesis were done using NavAb-N49K and performed by Catterall lab member, Tamer Gamal El-Din, PhD.

## 1.12 Figures

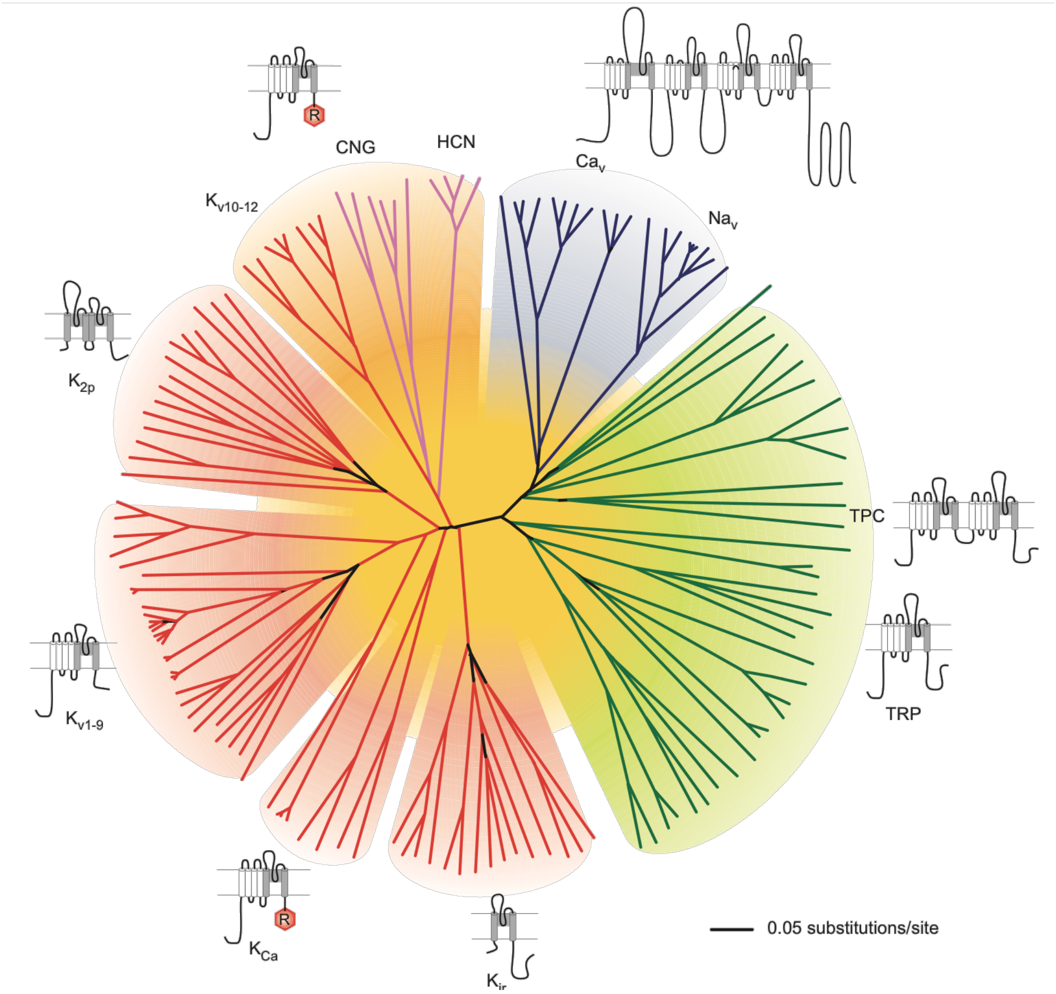

**Figure 1.1: Ancestry of voltage gated ion channels**. Figure from Yu and Catterall, 200422. Dendrogram showing amino acid relationships of voltage-gated ion channels. Sodium and calcium channels are related evolutionarily, shown in the blue wedge.

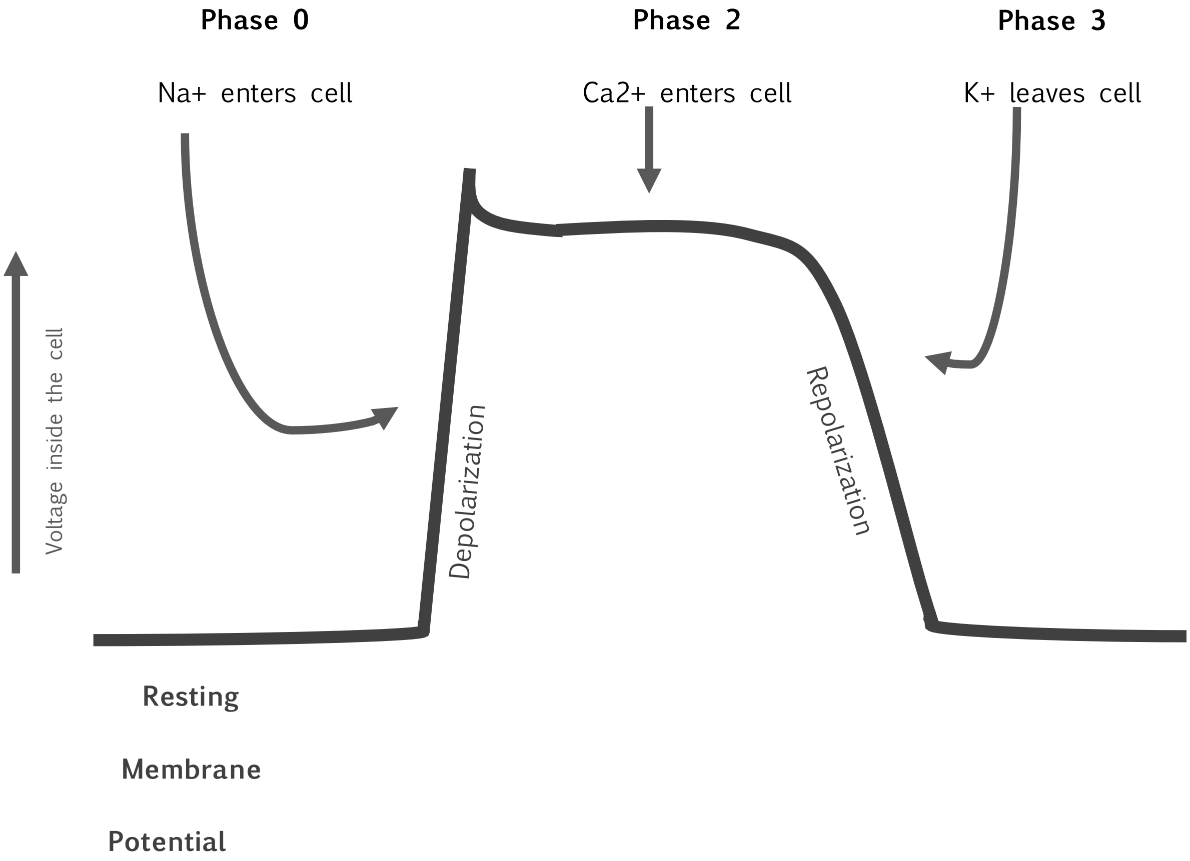

**Figure 1.2: Cardiac action potential.** Cardiac myocytes are depolarized by the quick opening of Nav channels, followed by a plateau of elevated membrane potential due to Cav and Kv channel openings. Repolarization of the membrane potential is due to the inactivation of Cav channels and K+ leaving the cell through Kv channels.

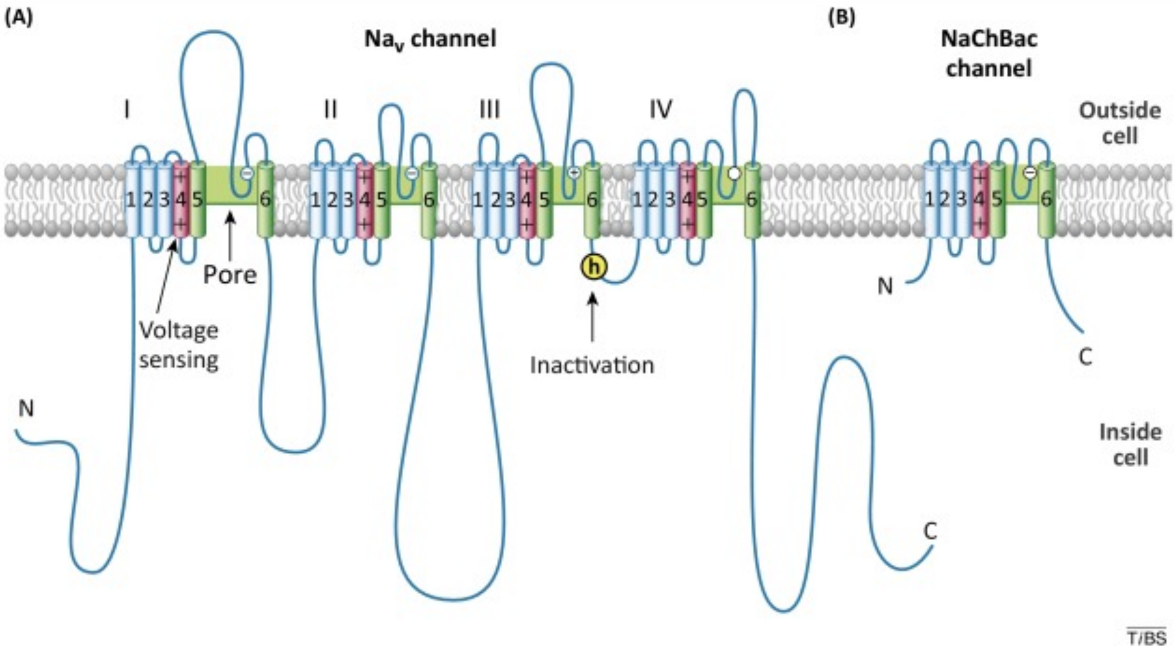

**Figure 1.3: Overall architecture of sodium channel $\alpha_1$ subunit.** Figure and legend adapted from Catterall & Zheng, 2015. (A) Mammalian Nav (and Cav) channels contain four homologous domains, each with six transmembrane segments. Segments S1-S4 make up the voltage sensing domain, with S4 containing the positive charges that respond to membrane potential. S5, S6 and the intervening P-loop make up the pore domain and line the ion conductance pathway through the channel. Loops and termini contain protein-protein interaction domains as well as sites of post-translational modifications. (B) Prokaryotic sodium channels are homotetramers with four identical repeating domains that come together to mimic the $\alpha_1$ subunit of mammalian channels.

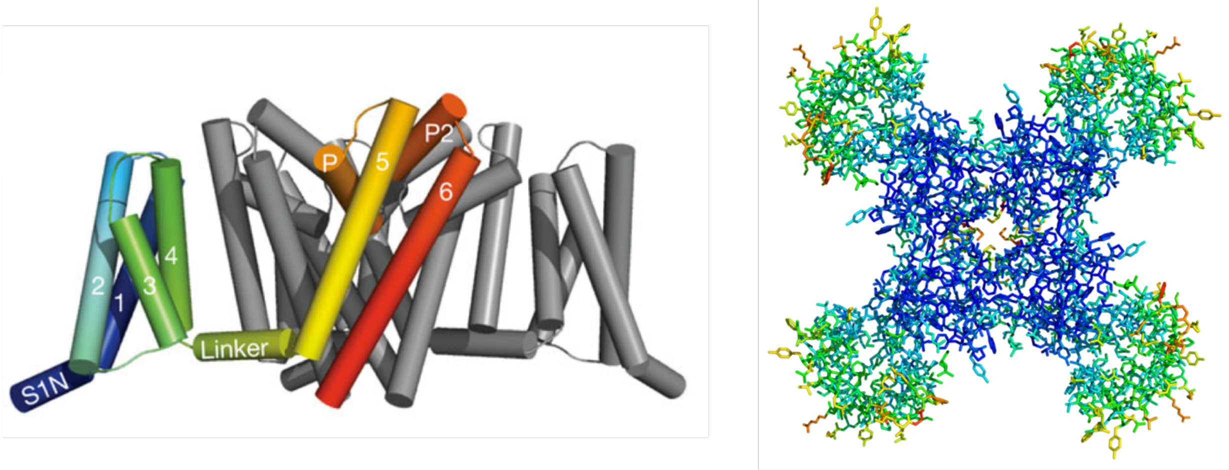

View from membrane

Extracellular View

**Figure 1.4: NavAb crystallization reveals four-fold symmetrical structure.** Figure and legend adapted from Payandeh *et al.,* 2011. Four identical subunits fold together to form the NavAb channel. Left: View from the membrane. One subunit is colored for visualization, S1-S4 in blue, organized around the pore domain, in yellow and red. Right: View of NavAb from the extracellular space, voltage-sensing domain shown in green and pore domain shown in blue. Ion conduction pathway can be seen down the center of the pore domain.

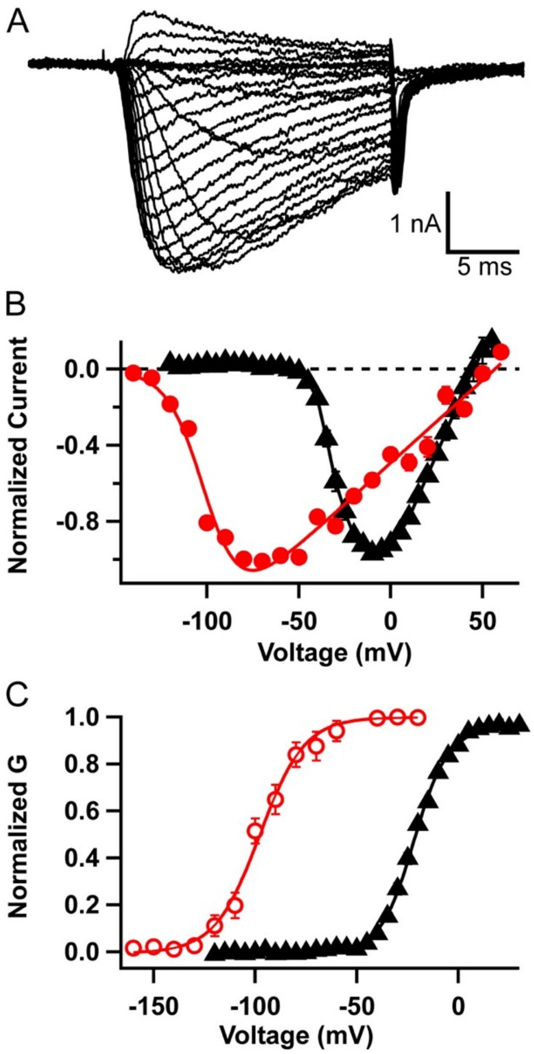

**Figure 1.5: Electrophysiology of NavAb WT and NavAb N49K.** Figure and legend adapted from Gamal El-Din *et al.*, 2013. (A). NavAb N49K sodium currents. (B) NavAb N49K (black triangles) shows a positively shifted peak current-voltage relationship compared to NavAb WT (red circles). (C) NavAb N49K (black triangles) shows approximately a +75 mV shift in voltage-dependence of inactivation compared to NavAb WT (red circles).

# 2 CALCIUM SELECTIVITY

## 2.1 Introduction

Ion channel specificity is found within the pore of the channel where the P-loops between helices S5 and S6 come together (Catterall, 2011; Hille, 1992). All four P-loops contain a subset of about seven amino acids that come together to create multiple ion binding sites near the top of the pore. This small region of an ion channel dictates much of its defining properties and after decades of research (Catterall, 2011; Hille, 1992), and still inspires continuing electrical and biophysical questions.

### *2.1.1 Kv Channel Selectivity*

Previous Kv channel crystal structures have shown that $K^+$ is selected for based on its ionic radius and arrangement of the first hydration shell around $K^+$ (Zhou & MacKinnon, 2003). $K^+$ ions travel through the pore in a dehydrated manner; their waters of hydration are replaced by the backbone carbonyl oxygens of the amino acids lining the selectivity filter (Figure 2.1).

There are four sites of $K^+$ coordination in the Kv selectivity filter, which are proposed to be alternately occupied to accommodate electrostatic repulsion between successive $K^+$ ions traveling through the channel. As new ions enter the selectivity filter and become dehydrated, previously bound $K^+$ ions are electrostatically knocked into the next position in the filter, and ultimately into the channel cavity. The ions are promptly rehydrated, and exit into the cell through the activation gate. $Na^+$ and $Ca^{2+}$ ions are thought to be excluded from Kv channel selectivity filters due to their larger ionic radii than $K^+$ and inability to be dehydrated and subsequently "rehydrated" by the lining carbonyl oxygens.

### *2.1.2 Selectivity Filter Structure*

Nav and Cav selectivity filters differ in architecture from Kv channels significantly (Hille, 1992; Payandeh, Scheuer, Zheng, & Catterall, 2011a; Yu & Catterall, 2004). The size of the pore is significantly larger for Nav and Cav channels than Kv channels, which is a first indication that these ions permeate in a different manner than $K^+$ (Payandeh, Scheuer, Zheng, & Catterall, 2011a; Zhou & MacKinnon, 2003). Secondly, the selectivity filters are not lined with carbonyl oxygens as the Kv filter is. Instead, Nav and Cav channels are lined by the side chains of amino acids, in addition to backbone carbonyls, to create the ion binding sites in the conductance pathway (Payandeh, Scheuer, Zheng, & Catterall, 2011a).

All Nav and Cav channels share a strictly conserved tryptophan (W), which I'll refer to as position 0 of the selectivity filter (Payandeh, Scheuer, Zheng, & Catterall, 2011a). Cav channels are most easily recognized by their strictly conserved glutamate (E) residue at the -2 position in the selectivity filter of all four Cav domains (Catterall, 2011). The EEEE motif is the position that seems to dictate calcium over sodium in eukaryotic channels. This EEEE motif provides a strong negative charge to attract $Ca^{2+}$ ions into the selectivity filter, and it's thought that $Ca^{2+}$ binds symmetrically within this selectivity filter.

At the equivalent position in eukaryotic Nav channels is a DEKA motif (Catterall, 2005), which presents an environment that is only slightly negative with two negative residues, a positive residue and a neutral residue. Several studies have mutated the DEKA motif to a EEEE motif, showing that the overall architecture of Nav channels can support $Ca^{2+}$ conductance. This also demonstrates the importance of this position in ion selectivity.

### *2.1.3 Calcium Selectivity Model*

In mammals, the extracellular $Na^{+}$ concentration is approximately 70-fold higher than $Ca^{2+}$ concentration (Catterall, 2011; Sather & McCleskey, 2003). Cav channels have evolved to maintain a $Ca^{2+}$ selectivity greater than 500-fold over $Na^{+}$, despite selecting for an ion which is not the most prevalent (Catterall, 2011; Sather & McCleskey, 2003). When relative concentrations are coupled with the fact that $Na^{+}$ and $Ca^{2+}$ have similar ionic radii at 1.16 Å and 1.14 Å, respectively, the unique challenge of $Ca^{2+}$ selectivity can be appreciated. Although models exist to explain this extraordinary selectivity, the precise biophysical mechanisms remain unknown.

A paired-sites model of conductance suggests that for the permeant ion, two adjacent binding sites must be present in the selectivity filter (B. Y. W. Almers & Mccleskey, 1984; W. Almers, Mccleskey, & Palade, 1984; Hess & Tsien, 1984; Hockerman, Peterson, Johnson, & Catterall, 1997b; Mccleskey & Almers, 1985) (Figure 2.2). The first site has high affinity for the permeant ion which occupies it at low ion concentrations. Occupancy of a second, lower affinity site would cause electrostatic repulsion and a decrease in affinity of the first site, causing the ion to be released into the channel pore and diffuse through the activation gate and into the cytosol.

According to this model, the divalent blocking cations such as $Cd^{2+}$, $Co^{2+}$ or $Mn^{2+}$ (Lansman, Hess, & Tsien, 1986; Tsien, Hess, & Mccleskey, 1987) would occupy only one high affinity site within the selectivity filter, lacking the second site to create the "knock-off" effect. This model suggests two different interactions of ions in the selectivity filter; a two-site permeation interaction, and a single-site blocking interaction. These mechanisms in Cav channels can be tested through crystallization of CavAb with $Ca^{2+}$ and pore-blocking cations.

### *2.1.4 Anomalous Mole Fraction Effect*

While Cav channels are selective for $Ca^{2+}$, they will also permeate $Na^{+}$ if no divalent cations are present. The anomalous mole fraction effect is when the conductance through a channel is lower in the presence of a mixture of permeant ions then when only $Ca^{2+}$ at the same concentration. It's thought this effect is due to both types of ions being able to move through the pore and differing selectivities for the ions. The anomalous mole fraction effect is characteristic of Cav channels and a strong indicator of $Ca^{2+}$ selectivity.

### *2.1.5 NaChBac Mutagenesis*

The first prokaryotic sodium channels studied was NaChBac, discovered by Clapham and colleagues in 2001 (Navarro et al., 2001). As previously mentioned, the overall architecture of BacNavs is similar to mammalian Nav and Cav channels. NaChBac contains a similar selectivity filter sequence to mammalian Cav channels (Yue et al., 2002), sharing a few conserved residues including a glutamate (E) at position -2 that is crucial for calcium selectivity (Figure 2.3). There is also a conserved threonine at position -4 which is present in both mCavs and NaChBac. Despite these similarities, NaChBac is more $Na^{+}$ selective than $Ca^{2+}$ selective.

Clapham and colleagues found they could switch NaChBac selectivity to $Ca^{2+}$ selective with successive point mutations in the selectivity filter (Yue et al., 2002). They in turn mutated positions -2, -1 and $^{+}2$ to change the wildtype $Na^{+}$ selective TLESWAS to TLDDWAD, a fully $Ca^{2+}$ selective filter. Relative permeability calculations showed that TLDDWAD was 133 times more $Ca^{2+}$ than $Na^{+}$ selective. Intermediate mutations showed a gradual switch from $Na^{+}$ to $Ca^{2+}$ selectivity. TLDDWAD also shows an anomalous mole fraction effect, which shows that TLDDWAD replicates more nuanced characteristics of $Ca^{2+}$ permeation.

### *2.1.6 NavAb Selectivity Filter*

NavAb has a similar selectivity filter sequence to NaChBac, 175-TLESWSM-181, which shares positions 0, -2 and -4 with Cav channels, as well as position -3 with NaChBac (Figure 2.3) (Navarro et al., 2001; Payandeh, Scheuer, Zheng, & Catterall, 2011a). As with NaChBac, NavAb is also $Na^{+}$ selective, despite the EEEE motif at the -2 position, which is residue E177 (Payandeh, Scheuer, Zheng, & Catterall, 2011a). Three ion binding sites were identified in the NavAb structure, the high-field-strength sites, $Site_{HFS}$ at E177, $Site_{CEN}$ at the carbonyl of L176 and $Site_{IN}$ at the carbonyl of T175 (Payandeh, Scheuer, Zheng, & Catterall, 2011a).

The NavAb structure contains an extracellular funnel just outside of the selectivity filter that spans the entire top of the pore domain (Payandeh, El-Din, Scheuer, Zheng, & Catterall, 2012b; Payandeh, Scheuer, Zheng, & Catterall, 2011a). The P-loops that come together to create the selectivity filter create this dip in the protein structure as they reach from the corners of the pore to the center. There is an overall negative charge on the NavAb extracellular funnel, which may help attract positively charged ion to the selectivity filter.

## 2.2 Research Strategy

The structure of NavAb, a NaChBac homolog, had been solved to 2.7 Å (Payandeh, Scheuer, Zheng, & Catterall, 2011a). Preliminary functional studies from Tamer Gamal El-Din had shown that when introduced to NavAb, the equivalent point mutations mentioned made in NaChBac also create a $Ca^{2+}$ selective NavAb channel, which is referred to as CavAb.

To test the paired-sites model of conductance, high-resolution crystal structures of NavAb-I217C, CavAb-I217C and intermediate mutant channels in the presence of a range of $Ca^{2+}$ concentrations were collected. Observation of the ion occupancy of sites within the CavAb selectivity filter could validate the "knock-off" mechanism.

To further test the paired-sites model of block, high-resolution crystal structures of CavAb in the presence of blocking divalent cations were collected. High-resolution data of CavAb bound to these blockers was expected to reveal a single binding site as the reason for cation block of calcium channels. Questions to be answered included whether all cation blockers bind to a single site, if the blocking site was the same for each blocker, and whether these sites are similar to either potential $Ca^{2+}$ binding site.

## 2.3 Results

Expanded results and discussion from this chapter have been published in: Tang L, Gamal El-Din TM, Payandeh J, Martinez GQ, **Heard TM**, Scheuer T, Zheng N, Catterall

WA. Structural basis for $Ca^{2+}$ selectivity of a voltage-gated calcium channel. Nature 505; 56-61 (2014). The project was completed as a collaboration among Tang, Gamal El-Din, Martinez and Swanson (previously Heard). All data published were from Tang (structural) and Gamal El-Din (functional) but Swanson and Martinez made all constructs and collected preliminary crystallographic data on them except TLDDWSN. Data statistics can be found in Table 2.1 and Table 2.2.

### *2.3.1 Constructs Studied*

NavAb-I217C was mutated at the equivalent positions to NaChBac, which are residues E177, S178 and M181. All channels discussed in this chapter contain the I217C mutation. Each of these positions was changed to an aspartate (D) in turn. This mutation makes the side chain length one carbon shorter at the 177 position, while introducing negative charge at the 178 and 181 positions. The channel with the filter sequence of TLDDWSD was coined CavAb, and was the most $Ca^{2+}$ selective channel studied. For all channels studied, the backbone of the protein was identical to NavAb-I217C, and so any changes that are seen in the electrophysiological properties of the channel are simply due to the changes in the positions of amino acid side chains at the sites mutated. This level of detail allowed us to provide structure-function relationships within the selectivity filter that had never been visualized before.

### *2.3.2 CavAb*

All constructs crystallized had a resolution of about 3.2 Å to 3.3 Å. The construct containing the selectivity filter TLDDWSD, CavAb, was the most $Ca^{2+}$ selective channel studied (Figure 2.4). For CavAb, $Ca^{2+}$ is 382-fold more permeant than $Na^{+}$. This is remarkable, given that calcium channels conduct monovalent ions such as $Na^+$ in the absence of Ca. This current is blocked by micromolar concentrations of Ca, and $Ca^{2+}$ conductance is observed at millimolar concentrations of extracellular Ca. This is a demonstration of the anomalous mole fraction effect that is characteristic for Cav channels.

The introduction of three negative charges per subunit to the selectivity filter drastically changes the electrostatics of the outer funnel of the pore. CavAb is significantly more negatively charged around the selectivity filter, potentially leading to greater attraction of divalent cations than NavAb (Figure 2.5).

### *2.3.3 Calcium Binding Sites*

A view of the TLDDWSN mutant in 10 mM $Ca^{2+}$ showed the best $Ca^{2+}$ anomalous densities within the selectivity filter, showing three sites along the axis of the pore (Figure 2.6). These three ion binding sites match well with the observed sites in NavAb, and here are named sites 1, 2 and 3. Site 1 is the most extracellular site located at the carbonyl and carboxylate oxygens of D178. Site 2 is the strongest density and is located near the carbonyl and carboxylate oxygens of D177, about 4 Å below site 1. Site 3 is located near the carbonyl oxygens of T175, which contains the weakest density and is right above the central cavity.

Distances between pore ions and coordinating oxygens are generally between 4.0 Å and 5.0 Å, distances that are too long to be direct coordination of Ca. However, these distances would be appropriate for a hydrated $Ca^{2+}$ ion, with water molecules acting as a bridge between $Ca^{2+}$ and oxygen atoms of the protein. Larger electron densities at the binding sites suggest waters are present around the ions, but at 3.2A resolution, they are not distinct.

$Ca^{2+}$ concentration was titrated in the TLDDWSN construct to investigate relative affinities of the observed $Ca^{2+}$ binding sites. Sites 1 and 2 were occupied at the lower concentrations, while site 3 was not occupied until higher concentrations were added. Occupancy of site 2 was greater at higher concentrations as well. These patterns indicate that sites 1 and 2 have higher affinities for $Ca^{2+}$ than site 3. Differences in affinities are likely due to the differences in coordination of the hydrated Ca; site 2 is the only site where eight coordinating oxygens were observed. The pattern of a high affinity site flanked by lower affinity sites correlates with predictions made for $Ca^{2+}$ permeation in the stepwise model.

### *2.3.4 Intermediate Mutations*

Aspartate mutations were made in the selectivity filter not only one at a time, but also in combination to give rise to a collection of channels with increasing $Ca^{2+}$ selectivity over $Na^+$. The intermediate channels studied were TLDSWSM, TLEDWSM, TLDDWSM, TLEDWSD, and TLDDWSN (Figure 2.4).

Interestingly, one channel that was made, TLDSWSM, was more $Na^+$ selective than Ca. While the structure of this mutant was not published, based on our findings I would hypothesize that this structure does not create a high affinity $Ca^{2+}$ binding site because the S178 does not coordinate the $Ca^{2+}$ properly.

Constructs TLEDWSM, TLEDWSD and TLDDWSN all had intermediate $Ca^{2+}$ selectivity between NavAb and CavAb. Each showed slightly different $Ca^{2+}$ binding characteristics and potential coordination of hydrated ions. Presumably, the difference in binding affinities for $Ca^{2+}$ because of the coordination leads to the differences in $Ca^{2+}$ selectivity.

The first intermediate to be crystalized was TLDDWSM, which I reported to the Department of Pharmacology in my rotation talks. To our surprise, this selectivity filter did not conduct $Ca^{2+}$ or Ba, but had working voltage-sensing domains. When EGTA was added to both intra- and extracellular solutions, $Na^{+}$ current could be seen through the channel. The structure of this mutant revealed that D178 was dunked into the center of the pore, tightly coordinating an ion, which was potentially dehydrated (Figure 2.7). We hypothesized that the affinity for cations at this site is too high to allow for proper conductance and therefore the $Ca^{2+}$ and Ba ions become blockers.

### *2.3.5 Functional Roles of Residues*

A comparison of relative $Ca^{2+}$ selectivity of intermediate mutants can shed light on the roles of individual residues within the selectivity filter. A single mutation of S178D is sufficient to make the switch from $Na^{+}$ to $Ca^{2+}$ selective because it opens up Site 1 for low affinity hydrated $Ca^{2+}$ coordination, as seen in the TLEDWSM mutant. The M181D mutation expands upon this selectivity by pulling E177 carboxylates away from the pore, allowing $Ca^{2+}$ to be hydrated at site 2. D181 also contributes to holding D178 in an orientation that allows for $Ca^{2+}$ coordination at site 1 without too high of an affinity for permeation (see TLDDWSM). The final addition of E177D allows for full hydrated $Ca^{2+}$ coordination by 8 carboxylates, introducing a high affinity site at site 2 and increasing $Ca^{2+}$ selectivity significantly.

### *2.3.6 Ion Permeation Mechanism*

The three sites within the selectivity filter cannot be occupied by $Ca^{2+}$ simultaneously due to electrostatic repulsion between the ions. We therefore concluded that the visibility of all three ion-binding sites in one structure was due to two states of occupancy within a single crystal and that only one of these states can be occupied at a time within a single molecule. State 1 would consist of sites 1 and 3 being occupied, while state 2 would only have site 2 occupied by a $Ca^{2+}$ ion (Figure 2.8).

$Ca^{2+}$ permeation would be initiated by $Ca^{2+}$ being recruited to low affinity site 1 by the negatively charged extracellular funnel, followed by successive ions knocking the occupying ion into the high affinity site 2 by electrostatic repulsion. Another $Ca^{2+}$ ion would be recruited to site 1, causing the ion at site 2 to be knocked to the low affinity site 3 so that sites 1 and 3 were occupied. This would continue to knock ions into the cavity of the channel through electrostatic repulsion of the ions entering the selectivity filter from the extracellular side.

### *2.3.7 Block by Divalent Cations*

$Ca^{2+}$ currents through Cav channels can be blocked by divalent cations such as $Cd^{2+}$, $Co^{2+}$ and $Mn^{2+}$. This block by divalent ions was mimicked in CavAb, with IC50s of 1.78 uM for $Cd^{2+2+}$, 526 uM for $Mn^{2+2+}$. CavAb crystals were soaked in 100 mM ions and data were collected at a wavelength of 1.75 Å for anomalous signal detection. The anomalous signals for both ions showed a strong density at site 2, coordinated by D177 side chains and L176 carbonyls (Figure 2.9). This high affinity for ions at this site would lead to block of the channel, rather than conductance, due to the inability to knock ions into the next binding site as new ions enter the selectivity filter. The hydration of $Cd^{2+}$ and $Mn^{2+}$ also takes on different geometry than Ca, as they maintain only six waters of hydration in their first shell.

## 2.4 Conclusions

Crystallization of CavAb has shed light on a few interesting biophysical properties of $Ca^{2+}$ selectivity and permeation. First, CavAb suggests that $Ca^{2+}$ ions are hydrated when in a Cav selectivity filter, which is in direct contrast to previous Kv channel studies. Second, it confirms that multiple binding sites are needed for $Ca^{2+}$ permeation. And third, CavAb provides a mechanism for divalent cation blockers of Cav channels. Overall, the CavAb structures support the paired sites and knock off mechanisms of ion permeation by demonstrating that there are multiple $Ca^{2+}$ binding sites of differing affinities.

While NavAb is obviously a valuable tool for studying Nav channels and their properties, the creation of CavAb provided a unique opportunity for our lab to structurally study a Cav channel at the atomic level. With CavAb's replication of several Cav channel properties, both structural and functional, we can confidently use CavAb to model other mechanisms of Cav channels in a system that is easily crystallizable, providing a resolution to Cav channel research that hasn't been achieved before.

## 2.5 Figures

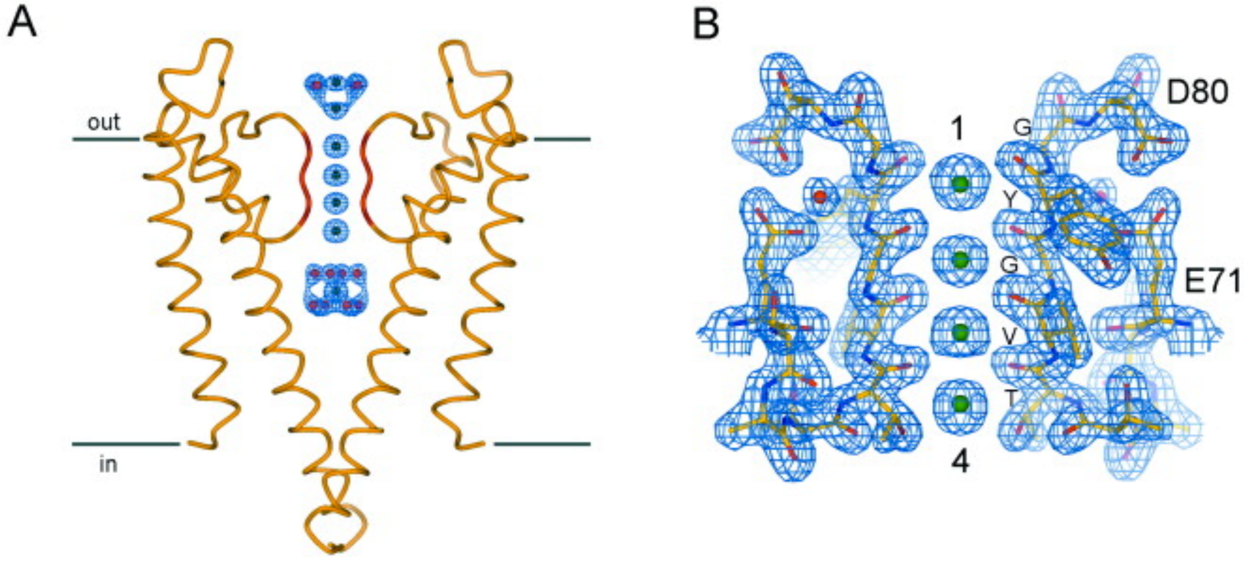

**Figure 2.1:** $K^+$ ions in the selectivity filter of bacterial Kv channel, KcsA. Figure adapted from Zhou and MacKinnon. A. KcsA in ribbon, two subunits removed for clarity. B. Selectivity filter of A, Fo-Fc mesh at 3σ in blue mesh.

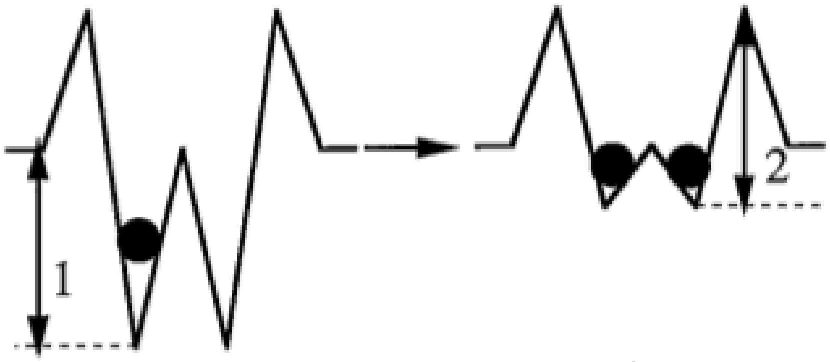

**Figure 2.2: Multiple $Ca^{2+}$ ions in the selectivity filter cause decrease in $Ca^{2+}$ affinity to allow permeation.** With two binding sites in the selectivity filter, occupancy of the second site decreases the affinity of both. This allows the ions to be knocked out of their sites easier, leading to conductance. Figure adapted from Dang & McClesky 1998.

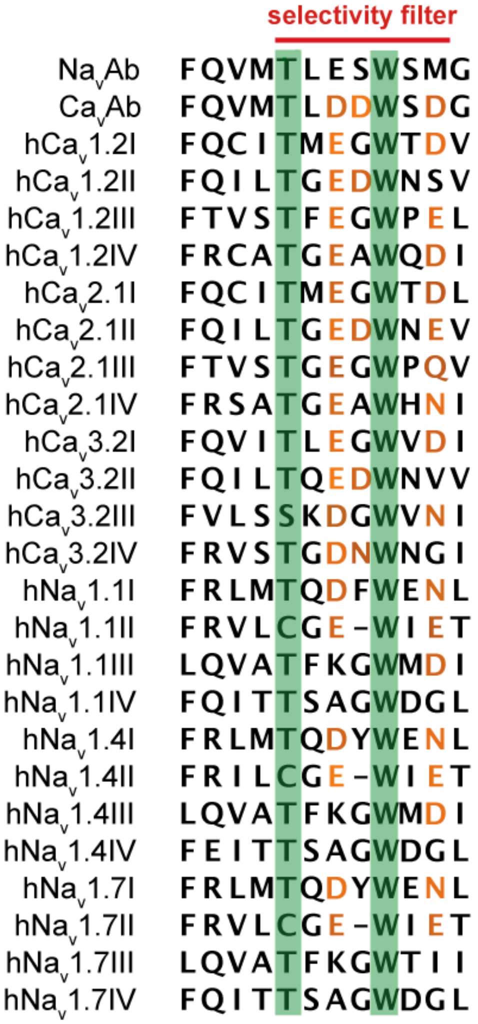

**Figure 2.3: Sequence alignment of NavAb, CavAb and Cav1.2 domains I-IV.** Alignment of the selectivity filter sequence of NavAb, CavAb, and the four domains from three human Nav and three human Cav channels. Two highly conserved residues that maintain the structural configuration of the filter are highlighted in green. Negatively charged and polar residues at positions corresponding to E177, S178, and M181 in NavAb are colored in yellow.

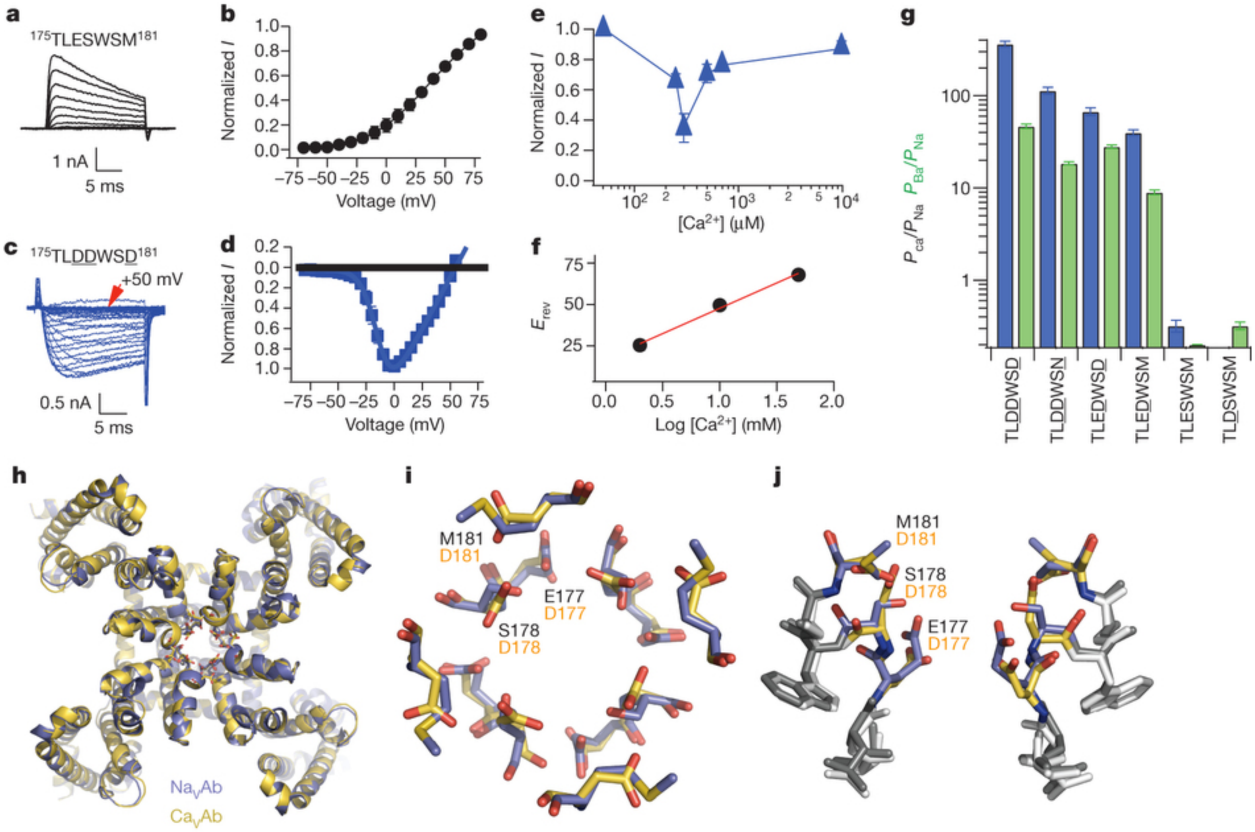

**Figure 2.4: CavAb biophysical properties and structures.** Figure and legend from Tang and Gamal El-Din, *et al.* Nature, 2014. a, b, Outward Na$^+$ current conducted by NavAb with 10 mM extracellular Ca$^{2+}$ and 140 mM intracellular Na$^+$. Holding potential, −100 mV; 20-ms, 10-mV step depolarizations. c, d, Voltage-dependent conductance of inward Ca$^{2+}$ current by CavAb under the same conditions. 20-ms, 5-mV step depolarizations. e, Biphasic anomalous mole fraction effect of increasing Ca$^{2+}$ as indicated, with Ba$^{2+}$ as the balancing divalent cation: 10 mM Ba$^{2+}$ with 0 to 0.5 mM Ca$^{2+}$, 9.3 mM Ba$^{2+}$ with 0.7 mM Ca$^{2+}$, and 0 mM Ba$^{2+}$ with 10 mM Ca$^{2+}$ ($n$ = 4–10). f, Reversal potential ($E_{rev}$) versus Ca$^{2+}$ concentration. g, Relative permeability of CavAb and its derivatives as measured from bi-ionic reversal potentials. $P_{Ca}/P_{Na}$, blue; $P_{Ba}/P_{Na}$, green ($n$ = 5–22). h, Cartoon representation of the overall structure of CavAb (yellow) superimposed with NavAb (slate). i, j, Top (i) and side (j) views of the superimposed selectivity filters of CavAb (yellow) and NavAb (slate) in stick representation. The three original NavAb residues (black) and substituted CavAb residues (orange) are indicated. Errors bars in b andd–g are ± s.e.m.

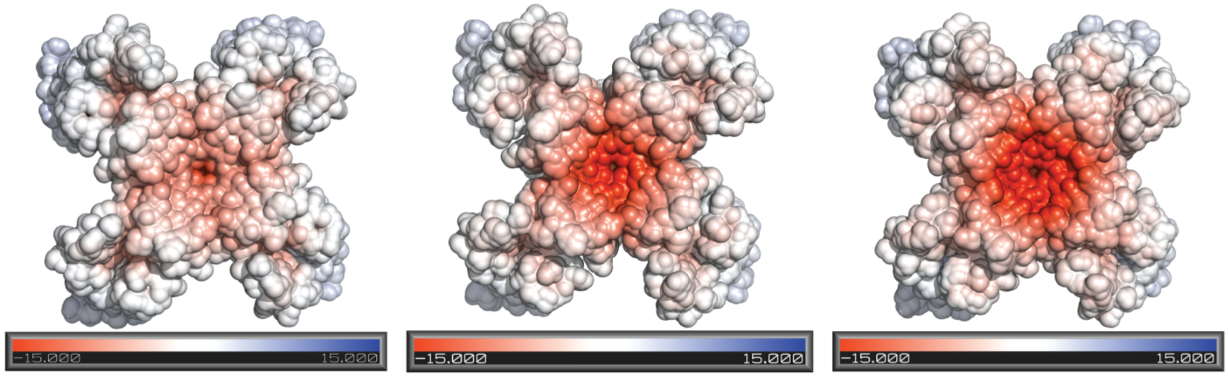

NavAb $^{175}$TL$\underline{\text{DD}}$WS$\underline{\text{N}}^{181}$ CavAb

**Figure 2.5: Protein surface electrostatic potential of NavAb and CavAb.** Figure and legend from Tang and Gamal El-Din, *et al.* Nature, 2014. The electrostatic potential on the surface of NavAb ($^{175}$TLESWSM$^{181}$), $^{175}$TL$\underline{\text{DD}}$WS$\underline{\text{N}}^{181}$, and Ca$_V$Ab ($^{175}$TL$\underline{\text{DD}}$WS$\underline{\text{D}}^{181}$) viewed from the extracellular side. Electronegative and electropositive charges are colored in red and blue, respectively.

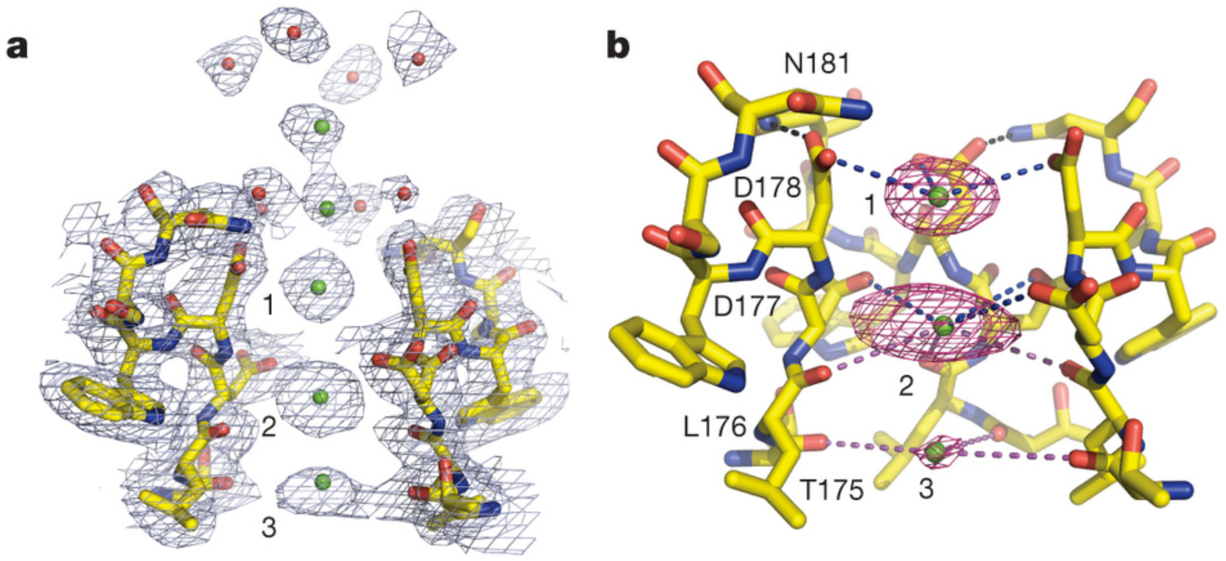

**Figure 2.6: CavAb TLDDWSN shows three Ca$^{2+}$ binding sites in the selectivity filter.** Figure and legend from Tang and Gamal El-Din, *et al.* Nature, 2014. a, Electron density at the selectivity filter of $^{175}$TL$\underline{\text{DD}}$WS$\underline{\text{N}}$$^{181}$. The $2F_o - F_c$ electron density map (contoured at $2\sigma$) of select residues in the selectivity filter with two diagonally opposed subunits shown in sticks, the Ca$^{2+}$ ions along the ion pathway in green spheres and water molecules in red spheres. b, Densities at Ca$^{2+}$ binding sites 1 and 2 from the anomalous difference Fourier map ($3\sigma$) calculated from the diffraction data of a$^{175}$TL$\underline{\text{DD}}$WS$\underline{\text{N}}$$^{181}$ mutant crystal soaked in the presence of 5 mM Ca$^{2+}$ and collected at 1.75 Å wavelength. The distances between Ca$^{2+}$ and oxygen atoms (dashed lines) are about 4.0 Å at Site 1 (blue lines), 4.4 Å at Site 2 (blue and magenta lines) and 5.0 Å (magenta line) at Site 3. For clarity, the subunit closest to the viewer is not shown.

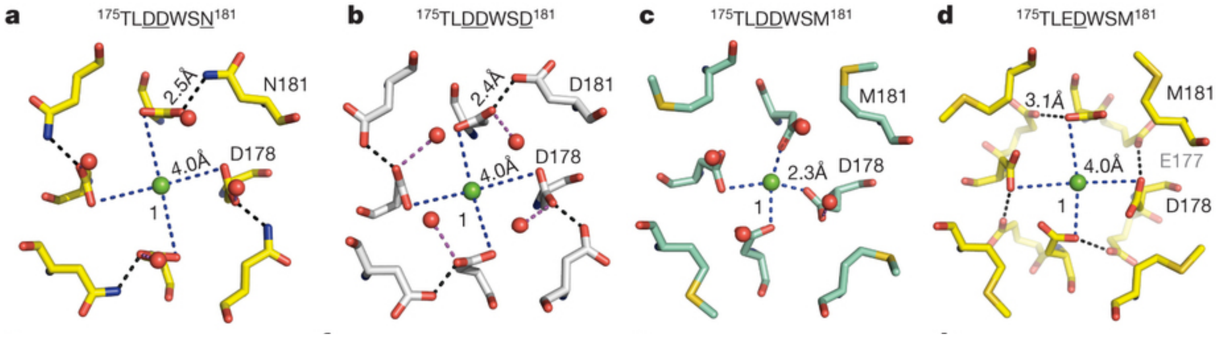

**Figure 2.7: Position of residue 178 in different constructs.** Figure and legend from Tang and Gamal El-Din, *et al.* Nature, 2014. **a**, **b**, Top view of Site 1 with a hydrated $Ca^{2+}$ ion coordinated by D178 with the help of N181 and D181 in $^{175}\text{TL}\underline{\text{DD}}\text{WS}\underline{\text{N}}^{181}$ and $^{175}\text{TL}\underline{\text{DD}}\text{WS}\underline{\text{D}}^{181}$ (CavAb), respectively. **c**, Binding of a dehydrated $Ca^{2+}$ ion at Site 1 in the nonconductive $^{175}\text{TL}\underline{\text{DD}}\text{WSM}^{181}$ mutant. **d**, Coordination of a hydrated $Ca^{2+}$ ion at Site 1 of the $^{175}\text{TLE}\underline{\text{D}}\text{WSM}^{181}$ mutant. Despite the absence of a polar residue at amino acid 181, E177 in $^{175}\text{TLE}\underline{\text{D}}\text{WSM}^{181}$ can hold D178 in place to allow the binding of a hydrated $Ca^{2+}$ ion.

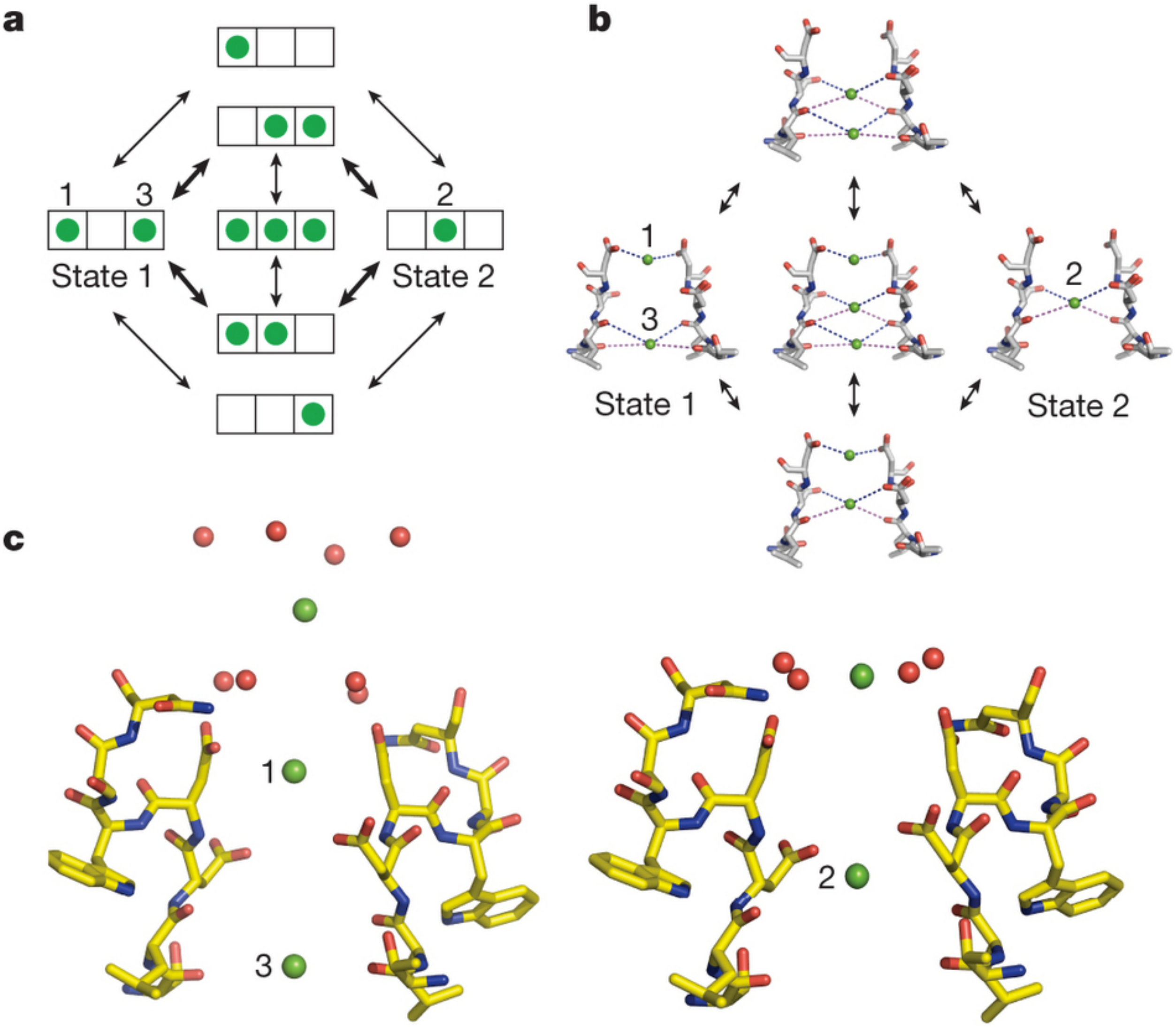

**Figure 2.8: Ion permeation mechanism.** Figure and legend from Tang and Gamal El-Din, *et al.* Nature, 2014. a, An ionic occupancy state diagram of CavAb showing two proposed low energy states and the potential transitions that connect them. Each state of the selectivity filter is represented by a three-box rectangle with Sites 1–3 going from left to right. Green circles represent $Ca^{2+}$ ions. Note that transitions in the inner circle potentially lead to ion repulsion, which might facilitate conduction. These transitions in the inner circle are more probable than those in the outer circle, as denoted by the bold arrows. b, The structural basis of the ionic occupancy states depicted in the inner circle of the state diagram shown on the left. The clockwise cycle represents a path for inward flux of $Ca^{2+}$ ions through the selectivity filter. c, Coupling of extracellular Ca-binding sites and the three sites within the selectivity filter in the two proposed ionic occupancy states. When two $Ca^{2+}$ ions bind to position 1 and 3 in the filter, the entryway $Ca^{2+}$ ion is placed furthest from the pore (left). When one $Ca^{2+}$ ion binds to position 2 within the filter, the ion outside the filter is pulled closer to the pore (right).

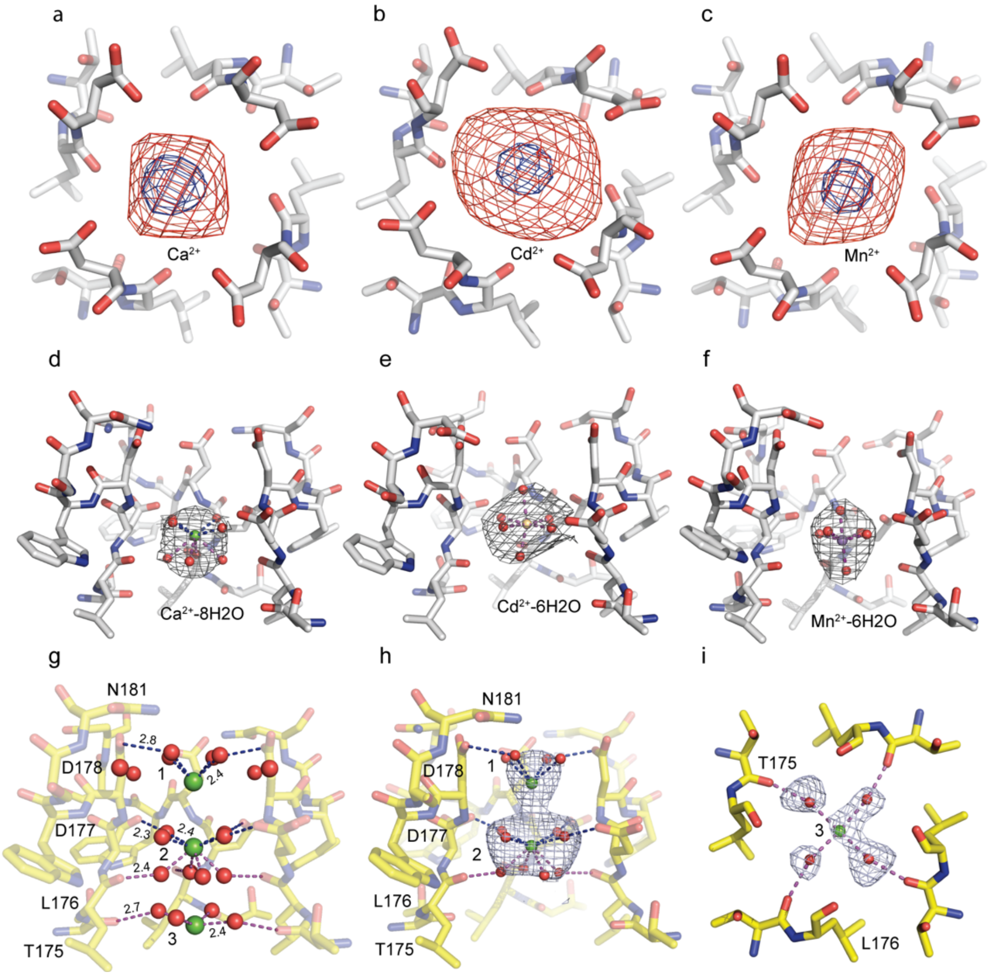

**Figure 2.9: Divalent cation blockers show one binding site in the selectivity filter.** Figure and legend from Tang and Gamal El-Din, *et al.* Nature, 2014. The distances between the coordinating residue and $Ca^{2+}$, $Cd^{2+}$, $Mn^{2+}$ are in a similar range of 4-5 Å. The anomalous difference Fourier maps (blue mesh) are contoured at 8σ, 34σ and 11σ for $Ca^{2+}$ (a), $Cd^{2+}$ (b) and $Mn^{2+}$ (c) at site 2, in sizes reflecting the real atom ionic radius. The |Fo-Fc| omit maps (red mesh) are calculated without ion and water included in the model and contoured at 3σ (red mesh) for $Ca^{2+}$ (a), $Cd^{2+}$ (b) and $Mn^{2+}$ (c) at site 2, indicating the likely hydration shell of $Ca^{2+}$, $Cd^{2+}$ and $Mn^{2+}$. d, e, f, 2|Fo-Fc| maps (grey mesh), contoured at 1.3σ, 2σ and 2σ, were calculated after potential hydrated ions ($Ca^{2+}$-$8H_2O$, $Cd^{2+}$-$6H_2O$ and $Mn^{2+}$-$6H_2O$) were included in the model and refined. All three datasets are collected at 1.75 Å wavelength, with crystals $^{175}$TLDDWSN$^{181}$ soaked with10 mM $Ca^{2+}$ (a and d), $^{175}$TLDDWSD$^{181}$ soaked with 100 mM $Cd^{2+}$ (b and e), and $^{175}$TLDDWSD$^{181}$ soaked with 100 mM $Mn^{2+}$ (c and f). To better define the position of $H_2O$ in the selectivity filter, one 2.75 Å dataset was collected with the $^{175}$TLDDWSN$^{181}$ crystals soaked with cryo-protectant solutions containing 15 mM $Ca^{2+}$. g, Coordination of the $Ca^{2+}$-nH2O complex at the three binding sites. The distance between oxygen atoms or oxygen atom and $Ca^{2+}$ is shown in Å. h, An |Fo-Fc| simulated annealing omit map contoured at 2.5σ for site 1 and 2 was calculated from the model in which the $Ca^{2+}$-$nH_2O$ complex was omitted. i, An |Fo-Fc| simulated annealing omit map contoured at 2.5σ for calcium binding Site 3 (Top view).

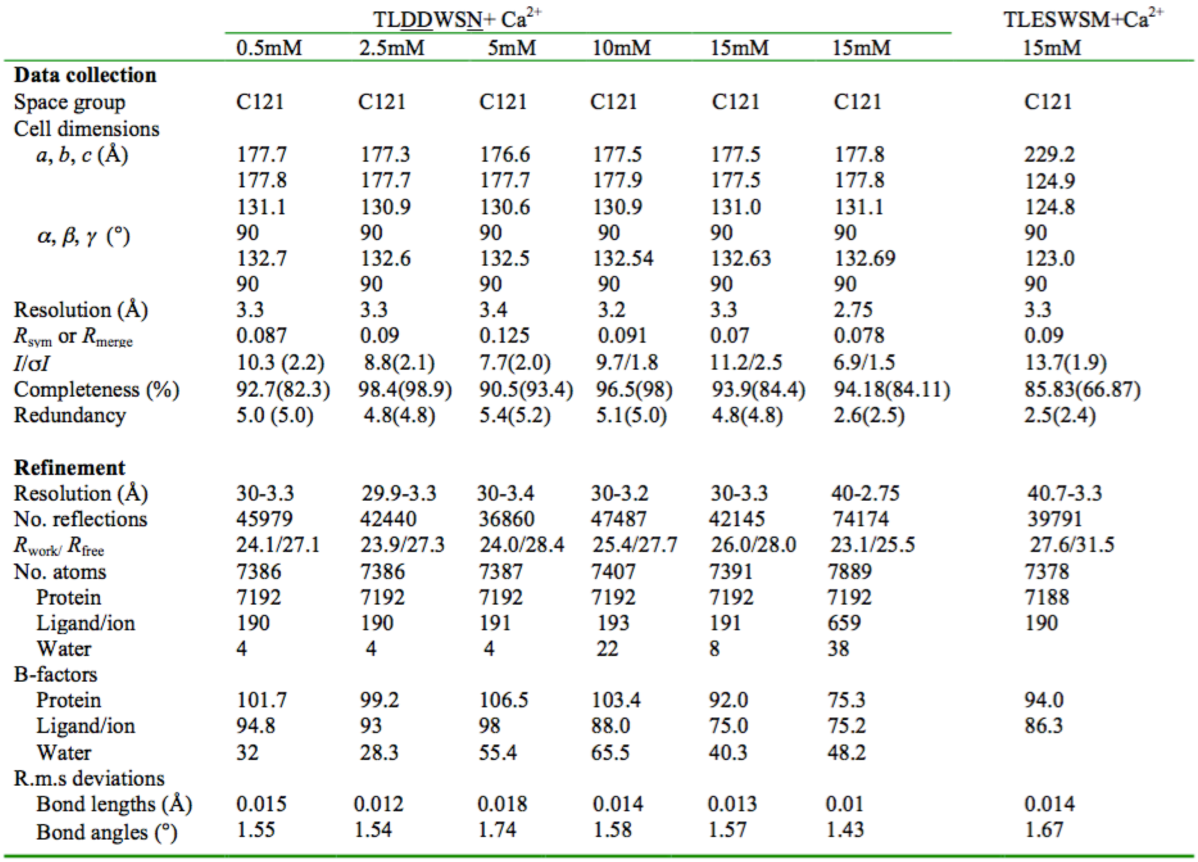

| | TL<u>DD</u>WS<u>N</u>+ $Ca^{2+}$ | | | | | | TLESWSM+$Ca^{2+}$ |
|---|---|---|---|---|---|---|---|
| | 0.5mM | 2.5mM | 5mM | 10mM | 15mM | 15mM | 15mM |
| **Data collection** | | | | | | | |
| Space group | C121 | C121 | C121 | C121 | C121 | C121 | C121 |
| Cell dimensions | | | | | | | |
| *a*, *b*, *c* (Å) | 177.7<br>177.8<br>131.1 | 177.3<br>177.7<br>130.9 | 176.6<br>177.7<br>130.6 | 177.5<br>177.9<br>130.9 | 177.5<br>177.5<br>131.0 | 177.8<br>177.8<br>131.1 | 229.2<br>124.9<br>124.8 |
| $\alpha, \beta, \gamma$ (°) | 90<br>132.7<br>90 | 90<br>132.6<br>90 | 90<br>132.5<br>90 | 90<br>132.54<br>90 | 90<br>132.63<br>90 | 90<br>132.69<br>90 | 90<br>123.0<br>90 |
| Resolution (Å) | 3.3 | 3.3 | 3.4 | 3.2 | 3.3 | 2.75 | 3.3 |
| $R_{\mathrm{sym}}$ or $R_{\mathrm{merge}}$ | 0.087 | 0.09 | 0.125 | 0.091 | 0.07 | 0.078 | 0.09 |
| $I/\sigma I$ | 10.3 (2.2) | 8.8(2.1) | 7.7(2.0) | 9.7/1.8 | 11.2/2.5 | 6.9/1.5 | 13.7(1.9) |
| Completeness (%) | 92.7(82.3) | 98.4(98.9) | 90.5(93.4) | 96.5(98) | 93.9(84.4) | 94.18(84.11) | 85.83(66.87) |
| Redundancy | 5.0 (5.0) | 4.8(4.8) | 5.4(5.2) | 5.1(5.0) | 4.8(4.8) | 2.6(2.5) | 2.5(2.4) |
| **Refinement** | | | | | | | |
| Resolution (Å) | 30-3.3 | 29.9-3.3 | 30-3.4 | 30-3.2 | 30-3.3 | 40-2.75 | 40.7-3.3 |
| No. reflections | 45979 | 42440 | 36860 | 47487 | 42145 | 74174 | 39791 |
| $R_{\mathrm{work}}/R_{\mathrm{free}}$ | 24.1/27.1 | 23.9/27.3 | 24.0/28.4 | 25.4/27.7 | 26.0/28.0 | 23.1/25.5 | 27.6/31.5 |
| No. atoms | 7386 | 7386 | 7387 | 7407 | 7391 | 7889 | 7378 |
| Protein | 7192 | 7192 | 7192 | 7192 | 7192 | 7192 | 7188 |
| Ligand/ion | 190 | 190 | 191 | 193 | 191 | 659 | 190 |
| Water | 4 | 4 | 4 | 22 | 8 | 38 | |
| B-factors | | | | | | | |
| Protein | 101.7 | 99.2 | 106.5 | 103.4 | 92.0 | 75.3 | 94.0 |
| Ligand/ion | 94.8 | 93 | 98 | 88.0 | 75.0 | 75.2 | 86.3 |
| Water | 32 | 28.3 | 55.4 | 65.5 | 40.3 | 48.2 | |
| R.m.s deviations | | | | | | | |
| Bond lengths (Å) | 0.015 | 0.012 | 0.018 | 0.014 | 0.013 | 0.01 | 0.014 |
| Bond angles (°) | 1.55 | 1.54 | 1.74 | 1.58 | 1.57 | 1.43 | 1.67 |

**Table 2.1: Published Data.** Datasets from this table were collected and processed by L. Tang, and reported in Tang L, Gamal El-Din TM, Payandeh J, Martinez GQ, Heard TM, Scheuer T, Zheng N, Catterall WA. Structural basis for Ca2+ selectivity of a voltage-gated calcium channel. Nature 505; 56-61 (2014).

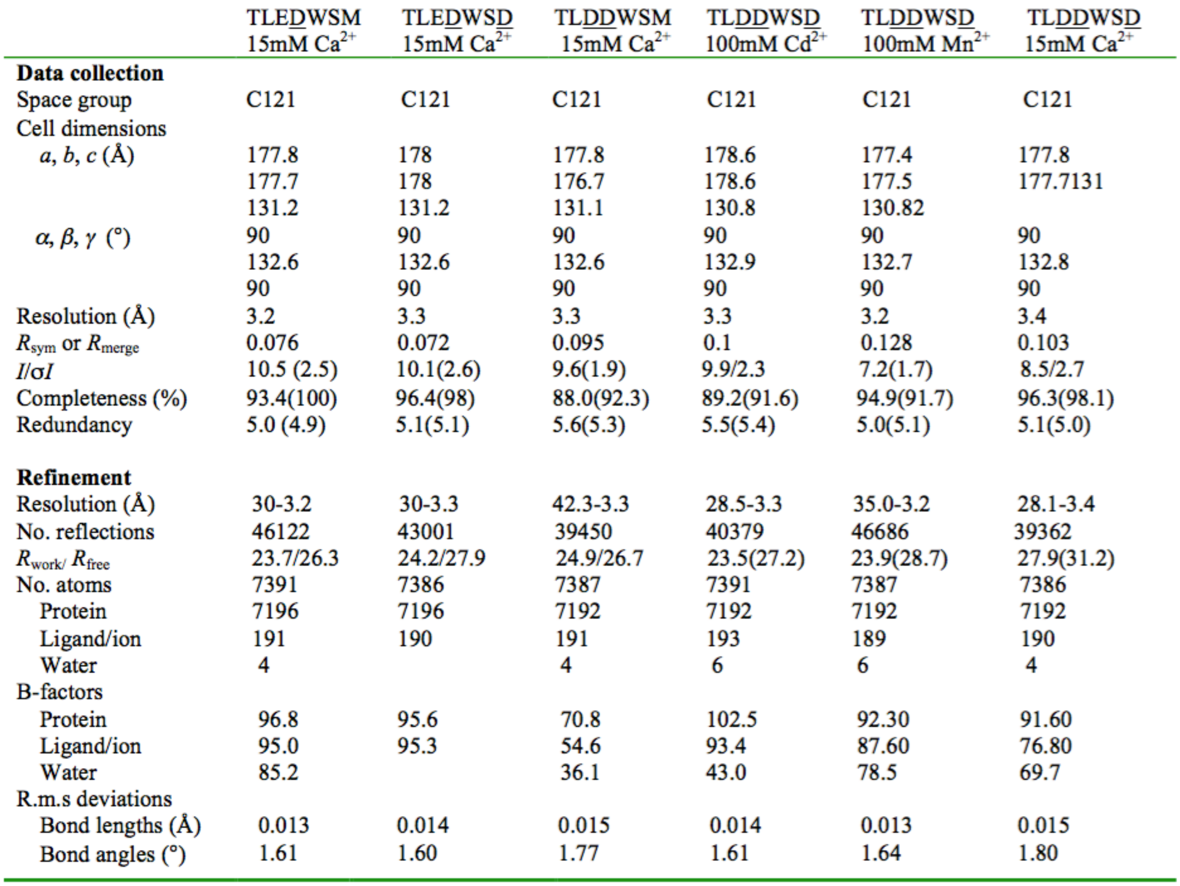

| | TLEDWSM 15mM $Ca^{2+}$ | TLEDWSD 15mM $Ca^{2+}$ | TLDDWSM 15mM $Ca^{2+}$ | TLDDWSD 100mM $Cd^{2+}$ | TLDDWSD 100mM $Mn^{2+}$ | TLDDWSD 15mM $Ca^{2+}$ |
|---|---|---|---|---|---|---|
| **Data collection** | | | | | | |
| Space group | C121 | C121 | C121 | C121 | C121 | C121 |
| Cell dimensions | | | | | | |
| *a*, *b*, *c* (Å) | 177.8<br>177.7<br>131.2 | 178<br>178<br>131.2 | 177.8<br>176.7<br>131.1 | 178.6<br>178.6<br>130.8 | 177.4<br>177.5<br>130.82 | 177.8<br>177.7131 |
| $\alpha, \beta, \gamma$ (°) | 90<br>132.6<br>90 | 90<br>132.6<br>90 | 90<br>132.6<br>90 | 90<br>132.9<br>90 | 90<br>132.7<br>90 | 90<br>132.8<br>90 |
| Resolution (Å) | 3.2 | 3.3 | 3.3 | 3.3 | 3.2 | 3.4 |
| $R_{sym}$ or $R_{merge}$ | 0.076 | 0.072 | 0.095 | 0.1 | 0.128 | 0.103 |
| $I/\sigma I$ | 10.5 (2.5) | 10.1(2.6) | 9.6(1.9) | 9.9/2.3 | 7.2(1.7) | 8.5/2.7 |
| Completeness (%) | 93.4(100) | 96.4(98) | 88.0(92.3) | 89.2(91.6) | 94.9(91.7) | 96.3(98.1) |
| Redundancy | 5.0 (4.9) | 5.1(5.1) | 5.6(5.3) | 5.5(5.4) | 5.0(5.1) | 5.1(5.0) |
| | | | | | | |
| **Refinement** | | | | | | |
| Resolution (Å) | 30-3.2 | 30-3.3 | 42.3-3.3 | 28.5-3.3 | 35.0-3.2 | 28.1-3.4 |
| No. reflections | 46122 | 43001 | 39450 | 40379 | 46686 | 39362 |
| $R_{work/}$ $R_{free}$ | 23.7/26.3 | 24.2/27.9 | 24.9/26.7 | 23.5(27.2) | 23.9(28.7) | 27.9(31.2) |
| No. atoms | 7391 | 7386 | 7387 | 7391 | 7387 | 7386 |
| Protein | 7196 | 7196 | 7192 | 7192 | 7192 | 7192 |
| Ligand/ion | 191 | 190 | 191 | 193 | 189 | 190 |
| Water | 4 | | 4 | 6 | 6 | 4 |
| B-factors | | | | | | |
| Protein | 96.8 | 95.6 | 70.8 | 102.5 | 92.30 | 91.60 |
| Ligand/ion | 95.0 | 95.3 | 54.6 | 93.4 | 87.60 | 76.80 |
| Water | 85.2 | | 36.1 | 43.0 | 78.5 | 69.7 |
| R.m.s deviations | | | | | | |
| Bond lengths (Å) | 0.013 | 0.014 | 0.015 | 0.014 | 0.013 | 0.015 |
| Bond angles (°) | 1.61 | 1.60 | 1.77 | 1.61 | 1.64 | 1.80 |

**Table 2.2: Published Data.** Datasets from this table were collected and processed by L. Tang, and reported in Tang L, Gamal El-Din TM, Payandeh J, Martinez GQ, Heard TM, Scheuer T, Zheng N, Catterall WA. Structural basis for Ca2+ selectivity of a voltage-gated calcium channel. Nature 505; 56-61 (2014).

# 3 HIGH RESOLUTION OF CALCIUM SELECTIVITY

## 3.1 Introduction

The CavAb studies discussed in Chapter 2 revealed important biophysical mechanisms of $Ca^{2+}$ selectivity in Cav channels. However, at 3.2 Å (Tang et al., 2014), the CavAb-I217C structures were unable to provide sufficient resolution for water molecules bound within the selectivity filter. We hypothesized that $Ca^{2+}$ is hydrated within the selectivity filter, but could not visualize these coordinating water molecules. While geometries of the hydration shell can be estimated with the placement of coordinating carbonyl or carboxylate oxygens in relation to the bound $Ca^{2+}$ ions, they could not specifically be observed. Also, we could not ask if these waters are always present in the channel or if they're simply brought along with a $Ca^{2+}$ ion when it enters the filter.

### *3.1.1 CavAb Truncation Construct*

Two colleagues in the lab, Dr. Michael Lenaeus and visiting scientist Karthik Ramanadane, created a NavAb construct for their projects in which the final 27 residues of the C-terminal tail were deleted. This construct does not seem to have the twinning issues that NavAb-WT crystals produce (see Chapter 4.3.4 for discussion on twinning).

Removal of the final 27 residues of CavAb did not seem to change the transmembrane portion of CavAb structure significantly; however, changes were seen in the four-helix bundle. The entire S6 still continues as a helix through the end of the peptide chain. Without the full extension of the tail, the four-helix bundle extends straight into the intracellular space from the transmembrane area. The curvature of the tail observed in full length CavAb (see Chapter 4.4.1.1) is eliminated in the d27 construct. The tail is truncated before the point where opposing molecules in the crystal lattice need to overlap. Without the overlapping tail ends, the d27 tails can be straight.

I started using CavAb-d27 for a project investigating Timothy Syndrome mutations in the activation gate to avoid crystal twinning (see Chapter 5.3). The CavAb-d27 construct does not have the I217C mutation present in the constructs from Chapter 2 and uses the TLDDWSD selectivity filter sequence. The Timothy Syndrome mutation used in this chapter is D219G. For a full discussion on how this mutant affects the C-terminal tail, see Chapter 5.

### *3.1.2 Preliminary Data*

Upon crystallization of a CavAb-d27 construct, it was very clear that the average resolution of the crystals was at least 0.5 Å higher than CavAb-WT or even CavAb-I217C. At this point, I revisited the selectivity filter to see if waters were visible in the pore. Crystallography can generally interpret densities as water molecules around 2.5 Å, and the average crystal resolution I was seeing was around 2.6 Å.

The Timothy Syndrome mutant D219G does not affect the selectivity filter structure of CavAb (Figure 3.1). Because the backbones of the proteins overlay, we can make a direct comparison between the CavAb-d27-D219G mutant used in this chapter, and the CavAb-I217C mutant used in Chapter 2.

## 3.2 Research Strategy

I used the CavAb-d27-D219G construct at high resolution to further investigate waters within the selectivity filter and how they contribute to $Ca^{2+}$ permeation through a Cav channel. Crystallization was carried out as previously published, and ions were soaked into preformed crystals in the same way used in Tang, *et al*. Different concentrations of $Ca^{2+}$ were used to visualize hydrated $Ca^{2+}$ in the pore. EGTA and BAPTA, two calcium chelators, were co-crystallized with CavAb-d27-D219G to produce crystals free of $Ca^{2+}$. Cav channel blockers were also re-investigated at high resolution in order to confirm their hydration states within a Cav channel pore.

## 3.3 Results

The work presented here has yet to be published. It is the sole work of myself, Teresa Swanson, under the guidance of Ning Zheng and Bill Catterall.

### *3.3.1 Crystallization Symmetry*

All CavAb-d27 constructs crystallized in the I422 space group, and did not present any signs of crystal twinning. The I422 space group produces a crystal structure in which there is only a single CavAb subunit within the asymmetrical unit. This makes the overall structure of the protein four-fold symmetrical around the central axis, which runs down the center of the pore. This is different from NavAb-I217C and CavAb-I217C, as they both crystallize in the I222 space group, which gives the channels two-fold symmetry.

Since the symmetry axis is along the center of the pore, and therefore down the center of the ion binding sites, careful interpretation of the ion binding sites was necessary.

Water peaks will not be as strong as ion peaks, and could easily be amplified by symmetry when in fact, they are not symmetrical within the pore.

For this reason, all structures in this chapter were solved in both the I422 space group as well as the C2 space group, a lower space group in which all four subunits are in a single asymmetric unit. Solving the structures in C2 allows for a view at the pore without symmetry being forced on the model. However, solving the structural models in the C2 space group causes the data to be less redundant and often less complete, leading to weaker densities that are more difficult to interpret.

For all cases presented in this chapter, there was no strong evidence that the symmetry induced by the I422 space group changed the interpretation of the models when compared to the same dataset solved in the C2 space group. Therefore, all results discussed in this chapter are from I422 models, unless otherwise specified.

### *3.3.2 Calcium Binding*

Crystals of CavAb-d27-D219G were soaked in different concentrations of $Ca^{2+}$ ions during cryoprotection. Three datasets were collected for 1.5 mM $Ca^{2+}$, five for 5 mM $Ca^{2+}$ and three for 15 mM $Ca^{2+}$ concentrations. Five “apo” datasets, without the addition of $Ca^{2+}$ but without the chelation of it either, were also collected.

In this construct, only one high affinity calcium binding site was observed, site 2 as previously discussed. Calcium coordination at site 2 showed eight distinct water molecules surrounding a $Ca^{2+}$ ion in a reasonable geometry (Figure 3.2). There are two rings of waters, one above and one below the $Ca^{2+}$. Waters on the top coordinate $Ca^{2+}$ with the carboxylate oxygen of D177, while the waters on the bottom coordinate with the backbone carbonyl of T175. Both the water-ion and water-protein distances were around 2.8 Å, easily within hydrogen bonding distance.

Interestingly, $Ca^{2+}$ occupies site 2 at any concentration of calcium collected, even when not specifically added (Figure 3.3). This suggests that the affinity for $Ca^{2+}$ at site 2 in this construct is very high, sequestering even the residual calcium present in the crystallization solutions. Waters are coordinated by the $Ca^{2+}$ ion as well as either a D177 carboxylate oxygen or a T175 carbonyl oxygen. All coordination distances are within reason for hydrogen bonds between 2.8 Å and 3.0 Å.

There was a reproducible density at site 1 (not shown), however lack of anomalous $Ca^{2+}$ signal here, as well as lack of response to EGTA and BAPTA addition suggests this density is not due to a divalent cation.

### *3.3.3 Absence of Calcium*

Two different approaches were used for eliminating $Ca^{2+}$ from the crystals. First, 10mM EGTA was added both for co-crystallization as well as in cryo-protection. EGTA is a common $Ca^{2+}$ chelator. However, CavAb crystallization is done at lower pH levels, around pH 5.0, which can interfere with $Ca^{2+}$ chelation. Three crystals with EGTA were collected. In these crystals, $Ca^{2+}$ was still seen at site 2, suggesting incomplete chelation and a higher $Ca^{2+}$ affinity at site 2 than when bound to EGTA.

Instead, 1 mM BAPTA was used because BAPTA's $Ca^{2+}$ chelating properties are more robust at lower pH levels. Two datasets were collected with BAPTA present. A distinguishable calcium ion is not seen at site 2 in these structures. Surprisingly, when BAPTA chelates $Ca^{2+}$ in the crystals, the structure reveals waters of hydration still similarly coordinated in the selectivity filter as if an ion where there (Figure 3.4). This suggests that even without calcium, the position of these eight waters are stable enough to exist in the selectivity filter.

### *3.3.4 Divalent Blockers*

Cadmium and Manganese block at high resolution were investigated as well, with 100 mM of either ion being added to the crystals during cryo-protection. Four datasets of $Cd^{2+}$ were collected, as well as four $Mn^{2+}$ datasets. Cadmium and manganese have smaller ionic radii than calcium, at 1.09 Å and .97 Å, respectively. The first hydration shells of these blocking ions contain six water molecules, as opposed to eight in calcium's first hydration shell. This has been hypothesized to cause block over permeation for divalent blockers.

Both $Cd^{2+}$ and $Mn^{2+}$ show only a single binding site within the selectivity filter, in the same place as previously determined (Figure 3.5). Neither ion displays distinct waters of hydration, although there are hints of them in the $Cd^{2+}$ structure. The $Cd^{2+}$ soaked structure shows a large Fo-Fc density around the ion, but does not show distinct water molecules. Two potential waters can be seen below the $Cd^{2+}$ ion, around the level of the lower ring of waters in the $Ca^{2+}$-bound selectivity filter. The $Mn^{2+}$ soaked structure clearly shows a single $Mn^{2+}$ ion within the selectivity filter, situated at the level of D177. The observed F0-Fc density is round with no clear indication of coordinating water molecules surrounding the ion or near the amino acids.

The lack of water observed in these structures is most likely due to the lack of ordered positioning of the six waters of hydration by the protein surrounding the ion. This confirms the idea that the six waters are not ideally positioned within the four-fold symmetrical selectivity filter to provide optimal coordination for permeation.

## 3.4 Conclusions

These studies are the first time waters of hydration have been directly observed within a Cav channel selectivity filter. My high resolution studies confirm our ion hydration model presented in Tang *et al*, 2014, verifying that $Ca^{2+}$ ions bound at site 2 are coordinated to the protein though eight waters in a hydration shell.

Surprisingly, the waters of hydration observed at site 2 are still found within the pore of the channel when $Ca^{2+}$ has been chelated by BAPTA. This shows that a $Ca^{2+}$ ion is not necessary for waters to be ordered within the selectivity filter, and that these waters are a standing part of a Cav channel. This is an unexpected and observation, and leads to more questions about the nature of the coordinating waters. The presence of waters in the pore in the BAPTA structures begs the question—are the waters observed in the pore the same ones that hydrate the $Ca^{2+}$ ion before entering the selectivity filter? Or are they rather the waters that are present in the pore before the ion enters, and strip the $Ca^{2+}$ ion of its hydration shell in order to replace it?

In this thought experiment, it is important to consider the potential exchange rates of the two water populations, as well as that the ionic blockers displace these eight pore water molecules, as they are not seen in the $Mn^{2+}$ or $Cd^{2+}$ structures. Importantly, no waters of hydration for ionic blockers $Mn^{2+}$ and $Cd^{2+}$ could not be specifically observed. This indicates ionic blockers (and their hydration shells) have high enough affinities to displace the waters observed in the BAPTA structures, but x-ray crystallography cannot answer the question of which water molecules are shed during $Ca^{2+}$ permeation.

Combined, these results provide convincing evidence that the waters of hydration around an ion are crucial in determining its permeability characteristics within a calcium channel selectivity filter. I showed that eight waters of hydration are necessary for permeation of cations, and that these waters are present whether ion is present or not. If waters of hydration reside permanently in the selectivity filter, they should be considered catalytic water molecules, in that they remain fixed and unchanged as they reduce the free energy for $Ca^{2+}$ conductance through the pore.

## 3.5 Figures

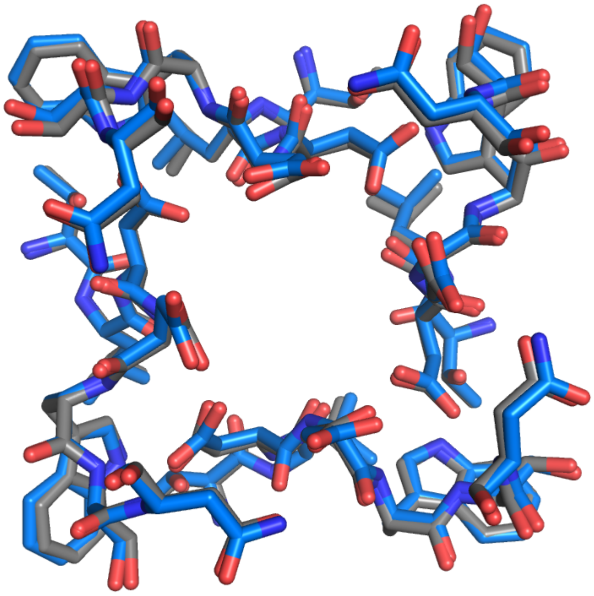

**Figure 3.1: Structural alignment of CavAb-I217C and CavAb-d27-D219G selectivity filter.** Backbones and side chains of CavAb-I217C in blue and CavAb-d27-D219G in grey align nearly perfectly, allowing for direct comparison between the two different constructs.

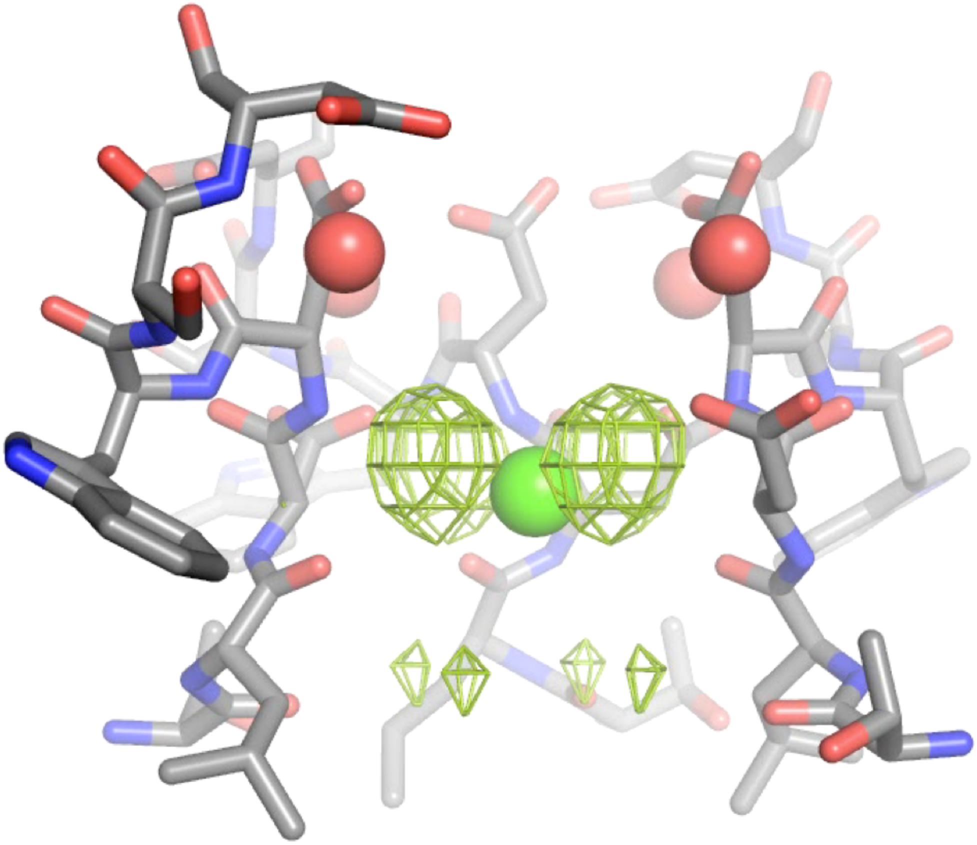

**Figure 3.2: CavAb shows eight water densities coordinating Ca2+ at site 2.** CavAb-d27 with 15mM Ca2+ shows eight distinct water densities surrounding a Ca2+ ion at site 2. Waters not included here for easier visualization of differences signal strength between upper and lower rings of waters. Fo-Fc electron density at 3σ shown in green mesh, Ca2+ ion shown as green sphere, and previously published water molecules shown as red spheres.

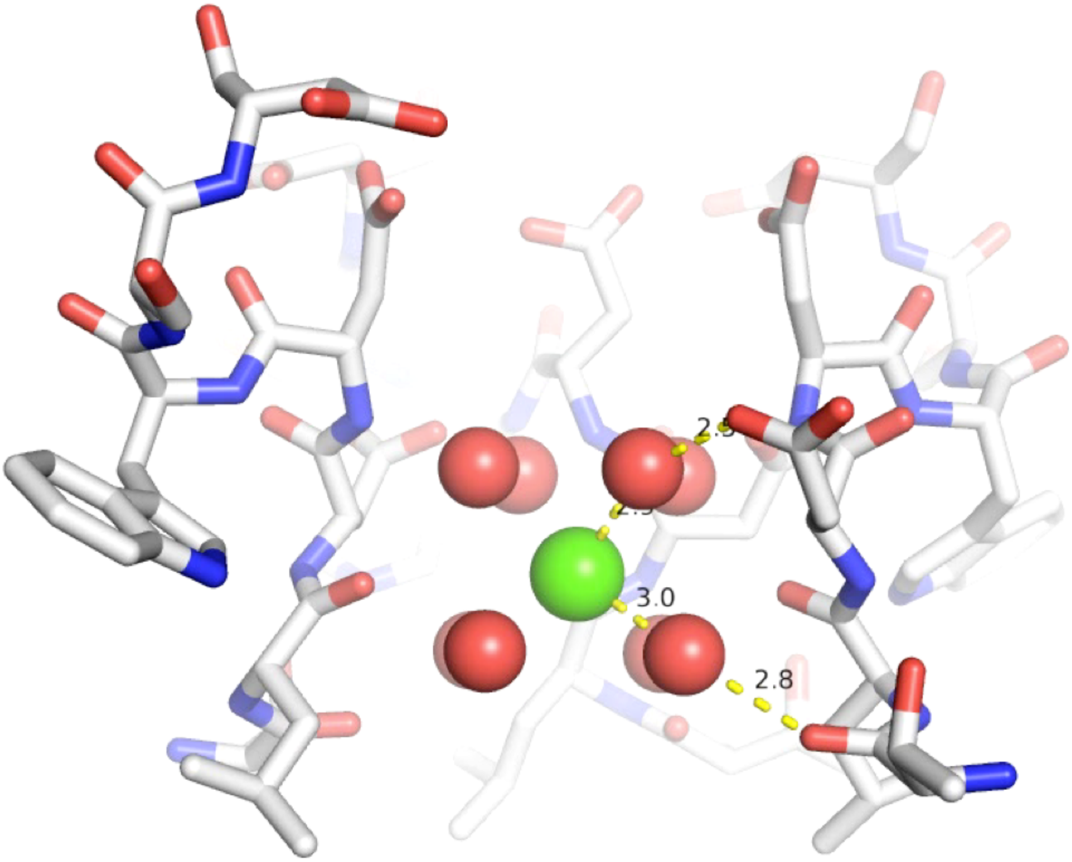

**Figure 3.3: Residual calcium is chelated by either waters at site 2.** Even without the addition of Ca2+, residual calcium from crystallization solution contamination is chelated at site 2. The top ring of waters is coordinated by the Ca2+ ion as well as a carboxylate water of D177. The bottom ring waters are coordinated by the Ca2+ ion as well as the carbonyl oxygen of a T175 residue. These eight waters maintain reasonable hydrogen bonding distances for the Ca2+-H2O distances as well as the H2O-Oxygen distances. Ca2+ ion shown as green sphere, and water molecules shown as red spheres.

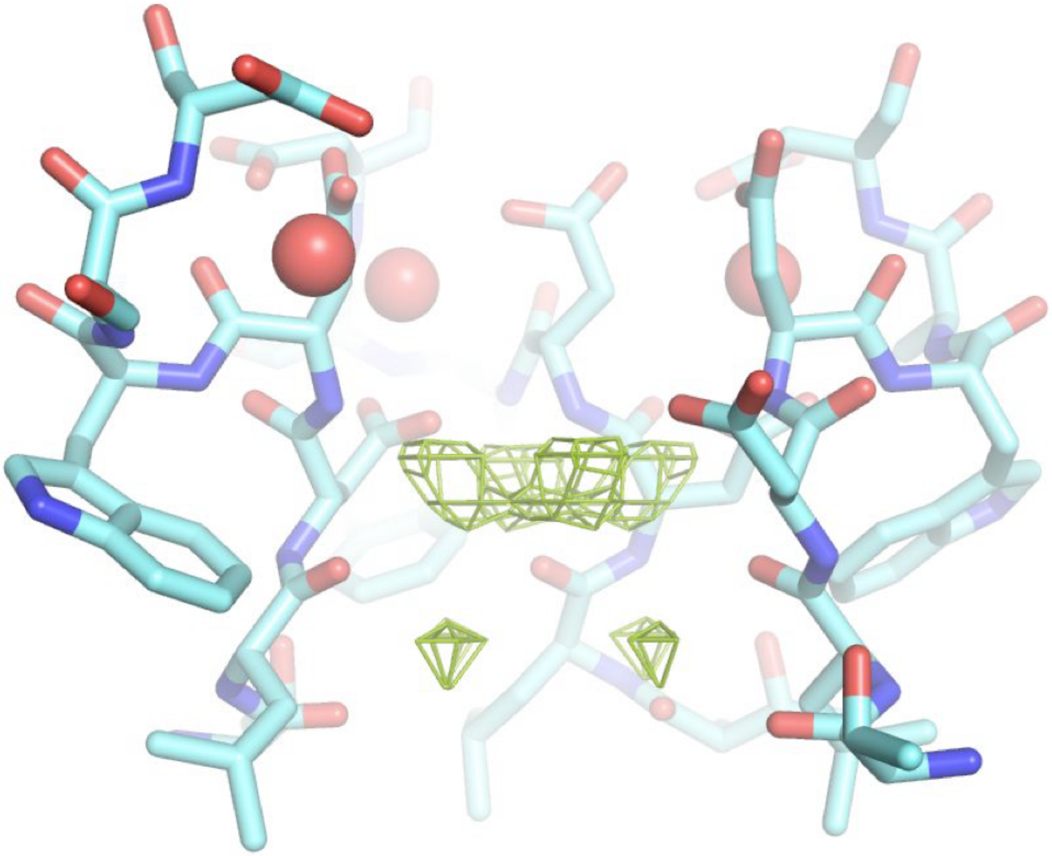

**Figure 3.4: Addition of BAPTA reveals waters of hydration are a stable part of the selectivity filter in the absence of calcium.** Fo-Fc electron density at 3σ shown in green mesh, and water molecules shown as red spheres. Eight water molecule densities are seen surrounding site 2, in similar locations to structures with $Ca^{2+}$ present in selectivity filter.

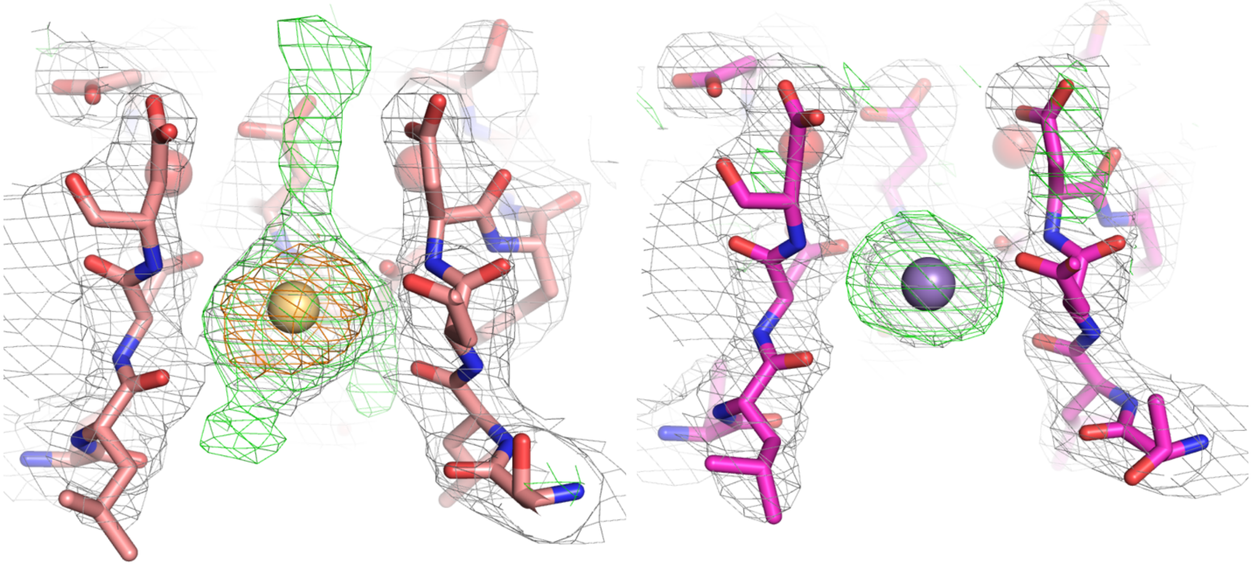

**Figure 3.5: Block by divalent cations at high resolution.** 2Fo-Fc densities shown in grey mesh and 2σ, Fo-Fc densities shown in green mesh at 3σ, and anomalous signal shown in orange densities, at 2σ. Red spheres are water molecules. *Left:* Cd2+ is seen in site 2 of the selectivity filter, shown as a yellow sphere. *Right:* Mn2+ is seen in site 2, shown as a purple sphere.

# 4 STRUCTURAL MECHANISMS OF ANTAGONIST BINDING

## 4.1 Introduction

A review of this information is published in: Catterall, W.A. and Swanson, T.M., Structural basis for pharmacology of voltage-gated sodium and calcium channels. Molecular Pharmacology 88 (1): 141-150. 2015.

When stimulated by an action potential, the voltage-gated calcium channel Cav1.2 allows calcium to enter cardiac and vascular smooth muscle cells to trigger contraction of the tissue (Moosmang, Lenhardt, Haider, Hofmann, & Wegener, 2005). Precise control of Cav1.2 is necessary for the regulation of heart rate, force of contraction, and blood pressure (Bers, 2002). Accordingly, drugs targeting Cav1.2 are used to treat a variety of cardiovascular diseases including hypertension, arrhythmias and angina. These drugs include phenylalkylamines, benzothiazepines and dihydropyridines (Hockerman, Peterson, Johnson, & Catterall, 1997b). The drug binding sites on Cav1.2 have been extensively mapped by site-directed mutagenesis (Hockerman & Johnson, 1997; Hockerman, Dilmac, Scheuer, & Catterall, 2000; Hockerman, Johnson, Abbott, Scheuer, & Catterall, 1997a; Hockerman, Peterson, Johnson, & Catterall, 1997b; Hockerman, Peterson, Sharp, Tanada, Scheuer, & Catterall, 1997c), but the structural basis for drug block is unknown.

Phenylalkylamines, benzothiazepines and dihydropyridines each have different physiological effects. Interestingly, their receptor sites are overlapping yet distinct, and involve neighboring amino acid residues in the pore domain of the α1 subunit of Cav channels (Hockerman, Peterson, Sharp, Tanada, Scheuer, & Catterall, 1997c). Both biophysical studies and site-directed mutagenesis studies suggest that the phenylalkylamines (PAA) and benzothiazepines bind within the channel pore, while the dihydropyridines (DHP) seem to bind on the lipid-facing backside of the pore-forming helices (Brauns et al., 2002; Hockerman et al., 2000; Hockerman & Johnson, 1997; Hockerman, Peterson, Johnson, & Catterall, 1997b; Hockerman, Peterson, Sharp, Tanada, Scheuer, & Catterall, 1997c; Kraus et al., 1996; Thomas Brauns et al., 1997).

### *4.1.1 Phenylalkylamines*

Verapamil is a characteristic PAA commonly used in the treatment of arrhythmias, hypertension, and cluster headaches. Despite verapamil's nanomolar affinity for the Cav1.2 channel (J.-P. Galizzi, Fosset, & Lazdunski, 1985; Johnson, Hockerman, Scheuer, & Catterall, 1996), side effects are common and a patient's risk of edema, stroke, and myocardial infarction increase during verapamil treatment (Opie, 2001; 1997). The design of new PAAs, including verapamil derivatives, could lead to increased therapeutic benefit with decreased side effects.

Phenylalkylamine drugs consist of two aromatic rings joined by a tertiary-amine containing linker (DRUG STRUCTURES). The tertiary amine is thought to be protonated when acting on Cav1.2, whereas the uncharged for allows the helps the small molecules pass through the membrane and bind to the channel from the intracellular side of the membrane.

### *4.1.2 Phenylalkylamine Binding Site*

Photoaffinity labeling of Cav1.2 in the late 1980's suggested that PAAs bind to the S6 transmembrane segments of domain III (DIIIS6) and domain IV (DIVS6). This would place the drug binding site within the pore cavity of the channel, although not directly in the center, as the S6 segments of DI and DII were not implicated. This led to the idea that PAAs act as physical blockers of the pore and plug of the conduction pathway of calcium ions through Cav1.2.

Further alanine scanning and mutational studies showed four main residues on the pore-facing side of the DIIIS6 helix, and three residues on the DIVS6 helix. Three-dimensional computer models of Cav1.2 based on potassium channel structures (Cheng, Tikhonov, & Zhorov, 2009; Hockerman, Johnson, Abbott, Scheuer, & Catterall, 1997a) suggest these amino acids do indeed face the center of the pore, rather than away from it, confirming the idea that the PAAs block the conduction pathway of calcium ions (Figure 4.1).

### *4.1.3 Phenylalkylamine Function*

Functionally, many PAAs including verapamil, exhibit a frequency-dependent block (Johnson et al., 1996) of Cav1.2, a characteristic that makes verapamil useful for treatment of arrhythmias. One can imagine that frequent opening of the channel increases inhibition of conductance due to increased access to its binding site inside the pore. This leads to an increased fraction of channels blocked with more channel openings.

In Cav1.2, the efficacy of block by verapamil varies for different conformational states of the channel in not only a frequency-dependent but also a state-dependent manner.

PAAs have a higher affinity for the inactivated state of the channel (Johnson et al., 1996). This is presumably because the channel needs to open in order for access to the pore, which eliminates the ability to access the closed state easily, but also an open pore maintains a faster off rate, leading to lower drug affinity. If Cav1.2 enters the inactivated state while the drug is trapped in the pore, the drug will maintain a slower off rate and therefore higher affinity for the channel. Common $IC_{50}$s for PAA drugs are in the high nanomolar to low micromolar range for state-dependent binding.

### *4.1.4 Phenylalkylamine Preliminary Data*

Preliminary electrophysiological data showed that verapamil has an affinity for CavAb-N49K comparable to mammalian Cav1.2 channels in the range of 250 nM. The specific residues reported to be involved in drug binding in Cav1.2 are not conserved in CavAb, but the overall fold and hydrophobicity of the proposed binding site is conserved, which seems to be sufficient to confer high-affinity binding.

The difference in $IC_{50}$ for block of CavAb-N49K in an open/inactivated conformation vs. a resting conformation is approximately 15-fold. Preliminary studies showed that the electrophysiological properties of verapamil binding to CavAb-N49K mirror the use-dependent and inactivated-state block seen in mammalian Cav1.2 channels.

### *4.1.5 Dihydropyridines*

Dihydropyridine drugs are mainly used for control of hypertension and coronary artery disease, as their effects on the vasculature are stronger than their cardiac effects. More DHPs are in clinical use than PAAs, with the most prescribed one being amlodipine.

Mild side effects of amlodipine include nausea and fatigue, while more serious side effects include severe low blood pressure or heart attacks.

Dihydropyridines contain two semi-saturated ring moieties, but their linker is a single bond long and does not maintain the flexibility of the PAA linker. The DHP ring is reduced across one double bond, in comparison to the aromatic rings of the PAA drugs that are fully oxidized. The DHP ring defines binding affinity, while the substitutions on the rings are modulators of affinity, with a wide variety of functional groups found on each ring.

### *4.1.6 Dihydropyridine Binding Site*

Similar to PAAs, DHPs were found to bind to DIIIS6 and DIVS6 by photoaffinity labeling (Striessnig, Knaus, & Glossmann, 1988). Follow-up alanine scanning mutagenesis confirmed that the binding sites were only overlapping, but not identical (Hockerman, Peterson, Johnson, & Catterall, 1997b; Hockerman, Peterson, Sharp, Tanada, Scheuer, & Catterall, 1997c; Peterson & Catterall, 2006; Peterson et al., 1997). Mutagenesis studies suggested four residues on DIIIS6 and four on DIVS6, only a few of which overlap with PAAs (Figure 4.1). One residue on DIIIS5 was also found to be important for binding. Both residues that are specific to Cav1.2 and residues that are conserved among Cav1 channels were among the positions identified.

Instead of sitting in the pore, the DHP binding site is nestled between the DIIIS6 and DIVS6 and the intervening DIIIS5 on the opposite helical face as the PAA site. This means that the DHP drugs bind to the channel in-between the subunits, on the outside of the pore. With the lack of structural insight into Cav channels, the precise mechanism of how this binding site controls calcium conductance was largely unknown.

### *4.1.7 Dihydropyridine Function*

Dihydropyridine drugs act on and bind to Cav1.2 in a very different manner than phenylalkylamines. Functionally, dihydropyridines bind to Cav1.2 with state-dependence; the drugs bind best when Cav1.2 is in the inactivated state, rather than the open or closed states (Hockerman, Peterson, Johnson, & Catterall, 1997b). Depending on the drug or even the enantiomers, DHPs can either be agonists or antagonists of the channel which suggests that they cannot block calcium conductance like the PAAs (Hering, Hughes, & Timin, 1993). Instead, the DHPs must be allosteric activators or inactivators of the channel, which bind to a site outside of the pore yet cause a physical change that stops calcium conductance. Common $IC_{50}$s for DHP drugs range from .3 nM to 1 μM for state-dependent binding.

### *4.1.8 Benzothiazepines*

Diltiazem is a canonical benzothiazepine drug used to treat high blood pressure, angina, and sometimes migraines (D. P. Galizzi & Borsotto, n.d.). The chemical structure contains a thiazepine ring, which is quite different from what is seen in the DHP and PAA drugs. It is thought to be a pore blocker similar to PAAs, and shares much of the same molecular determinants. Like PAAs, diltiazem block is frequency and voltage dependent (Hockerman et al., 2000). Surprisingly, block by BTP and PAA drugs seems to be noncompetitive (Kraus et al., 1996; Striessnig et al., 1998).

## 4.2 Research Strategy

Because of CavAb's similarity with Cav1.2 both structurally and functionally, it was hypothesized that the PAA verapamil and the DHP amlodipine would bind to and act on Cavab in a similar fashion to Cav1.2. Verapamil should bind within the channel cavity, physically blocking the conductance pore. Amlodipine should bind to the outside of the pore between subunits, causing some physical change that prevents calcium from passing through the channel.

This hypothesis was tested by co-crystallization of the CavAb-drug complexes. Placement of the drugs was confirmed by used of anomalous diffraction patterns from brominated drug derivatives. Following observation of binding sites, mutations were made based on the position of drugs in order to confirm their binding sites by disruption of the interaction. Residue positions that were shared between the prokaryotic and mammalian binding sites were of particular interest.

CavAb crystallizes in an either pre-open or inactivated state, and we know that PAA and DHP binding depends upon the conformation of the protein. Because of this, drugs were added to the protein at different points during crystallization in order to optimize binding conditions and drug visibility in the structural models.

## 4.3 Crystallographic Considerations

There were several considerations in the crystallization of CavAb-drug complexes that needed to be accounted for. The combination of these issues created a unique challenge to overcome for successful crystallization.

### *4.3.1 Binding Site Access*

The binding of PAA inside the cavity of the pore presented a unique challenge for the crystallographic determination of the drug-binding mode. PAAs are use-dependent drugs; increased time in the open conformation causes an increase in drug block (Johnson et al., 1996). This is presumably due to increased access to the binding site in the open conformation; the closed conformation slows the drug diffusion to its site of block. Crystallization places the protein in a single conformation, restricting the structural flexibility of CavAb. Also, it has been hypothesized that PAAs enter their binding site through the activation gate as it opens, which does not happen in a crystal structure. Examination of all published bacterial sodium channel structures reveals that fenestrations in the sides of the pore leading to the membrane are large enough in the various conformational states to allow drugs in and out of their binding sites (Payandeh, Scheuer, Zheng, & Catterall, 2011a), which might be a normal drug access pathway, or a substitute for the open activation gate in our case. Also, in NavAb and CavAb structures that do not have drug present, the cavity is filled with electron density thought to belong to lipids entering the pore through the fenestration. It is possible that PAAs are unable to displace the lipids and thus be prevented from binding.

While the DHP binding site is on the outside of the protein and more accessible, it is in the middle of the bicelle layer. This in itself should not affect drugs from accessing the site, as it’s a comparable environment to a cell membrane, however previous crystal structures have shown that a DMPC molecule- the lipid used in bicelle formation- sits in the proposed binding site and could potentially compete for the site.

### *4.3.2 Conformation Dependent Binding*

Since both PAA and DHP drugs bind to calcium channels in a conformation dependent manner, the addition of drug to CavAb must be done at a point in the protocol where the protein is flexible enough to accommodate drug. There are several points in the protein purification protocol where drugs could be mixed with protein; in cell culture, during lysis, with purified protein, after bicelle addition, in the crystallization well buffer, or in the crystal cryo-protectant as was done with the ions in the selectivity filter studies. The easiest option would be to add drug to CavAb after crystallization, where the unbound protein crystals could be soaked in a cryo-protectant solution that contains appropriate concentrations of drug. Protein molecules in crystals do not have structural flexibility however, and are unlikely to bind drug efficiently. This option was solely used in combination with earlier introduction of drug to CavAb, in order to maintain a constant drug concentration until protein crystals were frozen.

For the most protein flexibility and ideal binding site access, drug would be mixed in with cell culture media, allowing it to be present for the entirety of CavAb's lifespan. Addition of drug to the cell culture is feasible, but requires too much drug to be cost effective due to the large number of cells necessary for protein production and volumes during purification. While this may be possible with some compounds, it was out of the question for the brominated derivatives, which are significantly more expensive. Similarly, addition of drug during cell lysis results in wasted use of drug when CavAb is FLAG-purified.

The options we were left with were to add drug to purified CavAb protein, or after bicelle addition. The easiest option would be to add drug to CavAb after reconstitution in bicelles yet before crystallization due to concentrations necessary. When this was attempted however, some compounds did not dissolve properly. This is presumably due to lipophilicity allowing the drug to solely distribute into the bicelle phase. In the end, drug was added to purified protein before the addition of bicelles at appropriate concentrations for dilution. Purified CavAb is presumably flexible enough in solution to accommodate verapamil into its pore binding site, and does not have the lipid bicelle phase present yet to sequester drug away from the protein.

### *4.3.3 Symmetry*

The Cav1.2 channel is created from four homologous domains, linked together in the same peptide chain, that fold together to create the overall architecture of the $\alpha_1$ subunit. This means that the amino acid sequence of Cav1.2 is different in all four domains, creating an asymmetric channel, and particularly an asymmetric pore domain. This leads the PAA binding site in Cav1.2 to be asymmetric, and we can see that the mutational studies have shown that the molecular determinants of PAA binding are reserved to DIIIS6 and DIVS6, but not DI and DII.

In contrast, CavAb is created by the assembly of four identical subunits, creating a pore that is lined by the same amino acids in each of the helices. Preliminary functional studies show that PAAs have almost as high affinity for CavAb-N49K as they do for Cav1.2, and so this sequence symmetry does not substantially disrupt drug function.

However, the symmetry of CavAb could potentially be an issue for crystallography. X-ray crystallography relies on all molecules in the crystal lattice being oriented the same in order to produce high quality data. In previous projects with NavAb and CavAb, the observed symmetry was to our benefit, allowing for increased redundancy of data and solutions in higher symmetry space groups. The selectivity filter studies were not disrupted by this symmetry because the ions were located on the axis of symmetry, and themselves are symmetrical.

Verapamil and other PAA drugs are not symmetrical, yet we were trying to visualize them within a symmetrical system. At worst, the PAA wouldn't induce a conformational change and the protein-drug complexes could be oriented in any direction, causing a washing out of the drug density in the pore cavity. This would lead to complicated density that may be unresolvable, or would look similar to the density already seen in NavAb/CavAb without drugs present. Ideally, this asymmetry of the PAA would induce a protein conformational change when bound that would be large enough to orient all molecules in the crystal lattice in the same direction, leaving a defined drug density in the center of the cavity that drug can be modeled in to.

### *4.3.4 Crystal Twinning*

NavAb and CavAb crystal structures tend to be twinned, which is a data quality issue that arises from incorrectly ordered crystals. Twinning occurs when there are multiple crystal domains found within a single crystal that are oriented to each other in a definitive way such as a mirror or a rotation. This orientation to each other can be described with a “twin law”, which indicates how to rotate one domain in relation to the other in order to place both domains in the unit cell same orientation.

The type of twinning specifically found in CavAb crystals is called pseudo-merohedral twinning. This happens when the application of the twin law results in the crystal lattices of each domain overlapping each other and results in a higher perceived symmetry, or space group, in the crystal than is actually present because of the near perfect overlap of x-ray reflections from both domains.

Even though the diffraction data collected will be a combination of reflections from both crystal domains, it is still possible to solve and refine the crystal structure properly as long as the twin law is known. Without the twin law, an analysis of twinned data is based on reflections from two entirely differently oriented crystal domains, which can lead to distortion of the electron densities and incorrect interpretation. An application of the twin law throughout refinement allows for consideration of both crystal domains, and therefore correct electron densities for interpretation.

In order to use the twin law to re-orient the crystal domains, the fraction of the overall crystal that each domain occupies must be also be known. A crystal without twinning would have a twin fraction of 0, while a perfectly twinned crystal has a twin fraction of .5. Perfectly twinned crystals cannot be resolved using the twin law because of the inability to separate the diffraction patterns of the individual lattices and de-twin them accordingly. The closer the twin fraction is to .5, the more difficult it is to separate the reflection contributions of each lattice from each other, which results in distorted densities similar to trying to refine the data without accounting for twinning. However, mildly twinned crystals are able to be refined using a twin law, because the contributions from each lattice are easily separated.

While using the twin law allows twinned data to be used and refined, this solution does not come without consequences. Twinned data is sensitive to the selection of input models during refinement, and can easily become model bias, making the electron density maps deceiving. Care must be taken when manipulating models and omit maps must be referred to often in areas of high interest or uncertainty for validation.

## 4.4 Phenylalkylamine Results

Results discussed in this section are from experiments I designed, datasets I collected and analysis I performed under the guidance of Bill Catterall and Ning Zheng.

### *4.4.1 Verapamil*

CavAb-verapamil complexes were crystallized in the same conditions as previously published, with a final target concentration of 150 mM verapamil. This was the concentration after addition of the well buffer, and was maintained in cryo-protectant soaks for freezing. A high concentration of verapamil, well above the $IC_{50}$, was desired, to saturate every possible protein molecule in the crystals. Higher concentrations were attempted, but crystal formation was disrupted above 200 mM verapamil and crystals would not form at concentrations near 500 mM.

A total of 21 CavAb-verapamil datasets were collected with a range of 2.6 Å to 3.9 Å resolution, seven of which were twinned. For the majority of the datasets, the racemic mixture of verapamil was used, however one dataset that was not twinned was CavAb-(+)-verapamil, with a resolution of 3.2 Å. These crystals, as with CavAb-WT crystals without drug bound, were processed in the P222 space group, which is a change from the CavAb-I217C structures collected in the selectivity filter studies.

The P222 space group breaks down the symmetry seen in the NavAb/I217C structures, and contains all four subunits in the asymmetric unit (Figure 4.2). Because the binding site potentially interacts with all four S6 helices differently, non-crystallographic symmetry restraints were not used in the refinement of these structures.

#### *4.4.1.1 C-terminal tail*

Immediately, it was apparent that CavAb-verapamil induced a stabilization of the C-terminal domain, as it was visible for the first time in my first verapamil structures (Figure 4.2). The CavAb tail showed hints of electron density for all four helices, but only two were confident enough to build close to the end of the amino acid sequence. These structures revealed a long helix that extends from the top of the S6 helix, through the activation gate and all the way down to the end of the sequence. This helix spans nearly 60 Å through the membrane and into what would be the intracellular space. All four subunits come together to create a tight four-helix bundle for the intracellular domain of CavAb. This helical bundle is curved and the helices also curl around each other as in a coiled-coil, causing a nearly 90° rotation in the helix from the activation gate to the end of the tail.

Neither of the NavAb structures published nor any of the CavAb-I217C structures showed strong evidence of this tail. At the time of data collection, there was only a single paper out describing a prokaryotic channel C-terminal domain (Bagnéris et al., 2013). This structure from the Wallace lab showed a flexible neck region below the activation gate, before the four helix bundle formed further down in the sequence. Their studies did not suggest that the neck region could be entirely helical as I saw with CavAb.

#### *4.4.1.2 Crystal Packing*

Due to the surprisingly long and ordered C-terminal tail present, the crystal packing of the CavAb-verapamil structures was slightly different than observed in previous structures (Figure 4.3). The general packing scheme is the same; an S0 helix still interacts with a neighboring S0 helix, and the top of the pore domain still pack head to head with another pore domain. This leaves a large aqueous space between two intracellular faces.

The intracellular portion of the tail is actually longer than the transmembrane portion, which creates a conflict in the large aqueous space between CavAb molecules. The bottoms of two tails end up attempting to occupy the same space in the crystal, and instead end up packing next to each other. This causes a curvature in the helical bundle that can be followed all the way up to the membrane (Figure 4.3).

#### *4.4.1.3 Lipids and Detergent Molecules*

In previous structures, DMPC lipids from the bicelle phase can be visualized between subunits in the pore domain. These lipids are regularly associated with the channel, and the verapamil complex is no different. The DMPC molecules are securely wedged at the subunit interface (Figure 4.4).

The CavAb-verapamil complex reveals detergent molecules that pack around the C-terminal tail that had not been seen before. Several CHAPSO molecules associate with the channel just below the activation gate, in the crevice formed between the helical bundle and the S4-S5 linker. Either the stabilization of the extended S6 helix allows these molecules to bind there, or they help stabilize the helical bundle by packing snugly between the tail and the linker.

#### *4.4.1.4 Verapamil Electron Density*

The electron densities visualized in the 21 different datasets varied a bit, but consistent trends were found. All datasets showed a disruption of the known lipid density seen in the cavity in the absence of drug. Sometimes this density was simply the fenestration densities being disconnected but still fairly symmetrical, while other times the fenestration densities would disappear from one or two fenestrations, but remain in the others. This led to an asymmetrical density visualized. This density is potentially in a position to interact with residues T206 and M209, which are positions important for PAA binding in Cav1.2. Some datasets showed a small density lower in the cavity, although I was never able to identify it (Figure 4.4).

The disrupted density, coupled with the other observations discussed, point to verapamil accessing the pore but maybe not being able to orient the molecules in the crystal in the same direction, causing a washed out density. Without other indications that the drug is present, such as an anomalous diffraction signal, the cavity density is ambiguous and unable to be fit to drug.

#### *4.4.1.5 Verapamil Docking Experiments*

Since crystallography of the verapamil complex was ambiguous, I attempted to quickly model verapamil binding in the pore with a computational model. DockThor (Almeida, 2011; de Magalhães, Almeida, Barbosa, & Dardenne, 2014; de Magalhães, S Barbosa, Almeida, & Dardenne, 2012) is an online receptor-ligand docking server that enables flexible ligand docking to known protein structures, a difficult task for most ligand docking programs. Using the MMFF94S molecular force field and high degrees of customization, DockThor is specifically designed to handle flexible ligands.

Trial experiments were run with a known protein-ligand complex solved to 1.94 Å, the mCry$^{2+}$KL001 complex published by Shannon Nangle from Ning Zheng's lab (Nangle, Xing, & Zheng, 2013). DockThor correctly placed the large carbazole ring in the binding pocket, however it switches the placement of the methanosulfanomide group with the furan ring (Figure 4.5, top) from what was observed in the crystal. These results suggest that DockThor is reliable for general placement of flexible ligands and will be most accurate by the most significant moiety present in a small molecule.

CavAb docking experiments were carried out using the CavAb-verapamil pdb file (sans ligand) and a drug MOL2 file. The search area was defined as a large box around the central cavity, with a total of 30 runs. All other parameters were set to defaults.

Simulations of drug binding suggest that verapamil should bind near the top of the pore cavity, with the positively charged amino group folded significantly up into the negatively charged selectivity filter (Figure 4.5, bottom). The substituted rings rest underneath the P-loops, with their methoxy groups dangling into the cavity. Multiple trajectories show the rings in two main orientations respective of the amine, suggesting this charge interaction dictates the majority of the drug binding behavior in these simulations. Also, with only two relative orientations of the drug, not four as would be expected with a purely symmetrical channel, the docking shows that the CavAb structure has indeed lost symmetry in crystallization with verapamil.

The positions of substituted rings in the simulations align well with observed electron densities and the lack of consistency of which ring is oriented where could explain the ambiguity seen in the crystal structures. However, there is no drug density in the selectivity filter to explain the folded drug seen in these simulations.

Other docking experiments were done with CavAb + bromoverapamil (Bromoverapamil), CavAb-I217C-$Ca^{2+}$-BV, and CavAb-ranolazine (DRUG STRUCTURES). The bromoverapamil simulations are similar to verapamil and dictated mainly by the charge interactions, while the ranolazine simulations show a greater variety of drug positions, likely due to the increased size and flexibility of ranolazine as compared to verapamil. Ranolazine is a large anti-agina medication that is mainly a sodium channel inhibitor. I attempted to crystallize NavAb with ranolazine without any notable success.

#### *4.4.1.6 Other Verapamil Derivatives*

Due to the limited success of the CavAb-verapamil complex, other verapamil derivatives were sought out that would have potentially higher affinity for CavAb then verapamil. One compound in particular, D888, had been shown in Cav1.2 studies (Hockerman, Johnson, Abbott, Scheuer, & Catterall, 1997a; Johnson et al., 1996) to have a higher affinity than verapamil. It is important to note that most of the PAA binding studies done in Cav1.2 were done using D888. The residues determined to be important in drug binding caused disrupted D888 binding when mutated, but not significant disruption of verapamil.

However, production of this research compound was mostly discontinued due to lack of interest. After some investigation, small amounts of D888 and 11 other verapamil derivatives were acquired from Michael Kort at Abbvie, Inc. A couple of these derivatives were chosen for crystallization trials based on their chemical structures and co-crystallized with CavAb in the same way verapamil and bromoverapamil were. In the limited trials of these compounds, none lead to any crystal formation.

Another interesting verapamil derivative is D890 (DRUG STRUCTURES). This compound was used in studies focused on determining the access route of PAAs to their binding site (Berjukov et al., 1996; Berjukov, Kimball, Striessnig, & Hering, 1994; Leblanc & Hume, 1989). Even though it is overall lipophilic like any PAA, it does not cross the membrane due to the quaternary amine. Experiments showed that D890 could only access its binding side from the intracellular side of the membrane, leading to the hypothesis that PAAs access the pore through the activation gate when it opens. Since it is thought that PAAs are positively charged as they enter the channel, we hypothesized that CavAb crystallization with D890 might produce more clear results than verapamil due to its positive charge. A total of six datasets were collected for the CavAb-I217C-D890 complex, ranging from 3.1 Å to 3.7 Å, all of which were twinned datasets. Unfortunately, I ran into the same issues with symmetry and lack of confidence in drug presence and D890 could not be resolved in the pore.

### *4.4.2 Bromoverapamil*

In order to make an unambiguous assignment of the drug density, a brominated derivative of verapamil was used to provide the location within the pore through anomalous x-ray scattering data collection (DRUG STRUCTURES). This allows for the specific identification of an intense density observed from the anomalous scatterer, bromine, (collected at a wavelength of .92 Å) among the total electron density of the dataset and therefore more accurate information on how to fit the drug correctly into the binding site.

Importantly, our previous studies of binding of $Ca^{2+}$ to CavAb have shown that high-resolution images of ligand binding in the pore can be achieved, even with a relatively low affinity ligand like $Ca^{2+}$, and further that the location of ligands with anomalous scattering can be defined with accuracy.

#### *4.4.2.1 Bromoverapamil Data Collection*

The concentrations of racemic bromoverapamil were kept the same as verapamil, at 150 μM. Overall, I collected 29 CavAb-bromoverapamil datasets, ranging from 2.6 Å to 4.2 Å resolution, 20 of which were twinned. The twinned structures at first appeared to be in the P4 space group, but were determined to instead belong in the P222 space group, which is consistent with the verapamil results, as well as the datasets that were not found to be twinned.

#### *4.4.2.2 CavAb-Bromoverapamil Conformational Changes*

Crystal packing of the CavAb-bromoverapamil complex did not significantly change from drug-free structures. There were three major differences from the verapamil complexes that I observed in my data, including changes to the C-terminal tail and the bound DMPC molecules. First, the C-terminal tail was no longer visible, in contrast to the verapamil complexes. The reliable electron density ends just after the activation gate, in the same place as with CavAb-I217C. The rest of the sequence is too flexible to be seen. Second, the lack of ordered C-terminal tail means that any detergent molecules that were seen in the verapamil structures are not seen with bromoverapamil. Third, the DMPC molecules normally wedged between pore subunits are disrupted in the bromoverapamil complexes, with very weak density in those binding pockets, if it's there at all. Also of note is that all four fenestrations in the side of the channels were different sizes and shapes in the presence of bromoverapamil (Figure 4.6).

#### *4.4.2.3 Bromoverapamil Electron Density*

My structures of CavAb with the brominated verapamil derivative were very encouraging, and the images suggested that only a single molecule binds within the CavAb pore and induces a conformational change in the protein. This protein conformation changes the crystal packing, potentially rearranging the channel, and seems to place the drug in one orientation in the crystal lattice.

In these data sets, the anomalous scattering signal was not strong enough to be above noise, but the electron density was suggestive of a single drug molecule bound within the channel pore (Figure 4.7). The density is more vertical than seen with the verapamil complexes, and shows the drug bent into a "C" shape. The size of the electron density nearly perfectly accommodates a bromoverapamil molecule.

#### *4.4.2.4 CavAb-Bromoverapamil-Ca$^{2+}$ Complex*

Bound Ca$^{2+}$ has also been shown to affect verapamil's affinity for its receptor site, either acting as a competitor or enhancer depending on the experimental conditions (Ferry, Goll, Gadow, & Glossmann, 1984; J.-P. Galizzi et al., 1985; Hockerman & Johnson, 1997; Ptasienski, McMahon, & Hosey, 1985). These results point to an interaction of the drug with the selectivity filter where the Ca$^{2+}$ binding sites are located. It is hypothesized that verapamil is functional in its positively charged form, which would provide an obvious point of interaction with the negatively charged Cav1.2 selectivity filter. The local affinity of this charge is probably comparable to the affinity of $Ca^{2+}$ at the selectivity filter, as evidence by the competition of $Ca^{2+}$ and drug binding. One would expect to the see the charged group of verapamil lodged in the cavity, just on the intracellular side of the selectivity filter.

To explore this mechanism of drug-ion interaction, I crystallized CavAb-WT in the presence of bromoverapamil, followed by a crystal soak with 15 mM $Ca^{2+}$. Based on our selectivity studies, calcium should access the selectivity filter with a soak at this concentration and be clearly visible. A total of four datasets were collected for this complex, ranging from 3.1 Å to 3.6 Å. Two of these datasets were twinned, two were not. Before the addition of a known amount of calcium, many bromoverapamil structures seemed to have an ion in the selectivity filter. Not all structures showed this ion, and there was no pattern discernable with which protein preps or crystal trays with ions in the selectivity filter versus no ions. When calcium was added to the complex, crystallization did not reveal any improved or disrupted bromoverapamil density in the presence of calcium.

#### *4.4.2.5 CavAb-Bromoverapamil-$Mg^{2+}$ Complex*

Some experiments have also found $Mg^{2+}$ to be a modulator of verapamil's binding affinity for Cav1.2 (J.-P. Galizzi, Fosset, & Lazdunski, 1984). Based on these studies, magnesium was soaked into CavAb-WT-bromoverapamil crystals in the same way as calcium was in order to visualize any change in the bromoverapamil structure. Two datasets were collected, 3.1 Å and 3.2 Å, both moderately twinned. Both showed $Mg^{2+}$ in the selectivity filter, and a cavity density that was unable to be clearly interpreted, similar to verapamil structures.

#### 4.4.2.6 Other Bromoverapamil Derivatives

Two other derivatives of bromoverapamil were investigated, coined BVa and BVb. The three derivatives differ in the placement of bromine on the aromatic rings, as well as the other functional groups present. BVa and BVb contain bromine on opposite aromatic rings. Crystal structures with anomalous diffraction data would presumably show nearly the same drug bound structure for each of these compounds, with opposing anomalous signal locations in the drug density allowing for definitive evidence as to how the drugs are oriented in the pore. Three datasets of each compound in complex with CavAb-WT were collected at a .92 Å wavelength, ranging from 2.9 Å to 4 Å resolutions, none of which were twinned. Unfortunately, no anomalous signal was resolved, and drug densities were inconsistent and unable to be interpreted.

#### 4.4.2.7 CavAb Mutagenesis

One aim of this project was to investigate the molecular determinants of drug binding in CavAb and crystallize drugs in complex with these CavAb derivatives. Multiple CavAb constructs were investigated in order to investigate different aspects of PAA binding.

Two constructs were directly based on the Cav1.2 residues in domains III and IV, mutating CavAb residues at identical positions to the residues found in Cav1.2. The first construct was CavAb-YIFV, which contained the four mutations found on Cav1.2 DIIIS6 important in PAA binding. The second construct, CavAb-YAI, contained the mutations

I202Y, T206A and M209I which created the YAI motif from Cav1.2 DIVS6 known to improve PAA binding in Cav1.2 (Hockerman, Peterson, Johnson, & Catterall, 1997b). Due to the homotetrameric nature of CavAb, these mutations were present in all four S6 helices, unlike in Cav1.2. CavAb-YIFV was not successfully crystallized. CavAb-YAI was crystallized without drug present and five datasets were collected, ranging from 3.1 Å to 3.8 Å, all of which were significantly twinned. These mutations alone didn't seem to affect the overall structure of CavAb, and due to the four-fold symmetry in the added residues, the crystallization of these constructs was not pursued with drug present.

Two mutations were made to investigate the route of drug access to the binding site; CavAb-F203A and CavAb-F203W. Bromoverapamil undoubtedly accesses the central cavity in purified protein, meaning that an open activation gate is not required for drug access. Residue F203 is located on the S6 helix and sits in the top of the fenestration that connects the pore cavity to the membrane. The hypothesis was that by mutating the phenylalanine to bulky residue, tryptophan, we'd block drug access to the pore, and a mutation to a small residue, alanine, we'd improve access to the pore. CavAb-F203W was not crystallized, but four datasets for CavAb-F203A were collected, ranging from 2.9 Å to 3.5 Å, none of which were twinned. These data showed an increase in fenestration size, but no other changes in the structure.

## 4.5 Published Bromoverapamil Results

Expanded results and discussion from this section are published in: Tang, L., Gamal El-Din, T.M., Swanson, T.M., Pryde, D., Scheuer, T., Zheng, N., Catterall, W.A., Structural basis for inhibition of a voltage-gated $Ca^{2+}$ channel by $Ca^{2+}$ antagonist drugs. Nature 537, 117-121 (01 Sept 2016). Data statistics are found in **Table 4.1**.

A crystal structure collected by L. Tang at 3.3 Å resolution showed a different orientation of bromoverapamil in the pore than I had seen. This structure was from studies of CavAb (DDN) in which an Asn residue is substituted at position 181 rather than an Asp residue as in CavAb (DDD). The complex was crystallized with 100 μM bromoverapamil, and 5 mM calcium was soaked in to the crystals during cryo-protection.

In this structure, bromoverapamil sits right below the selectivity filter in a flat, elongated position (Figure 4.8). The aromatic rings reach towards the fenestrations and are near positions important in Cav1.2 PAA binding. The aromatic ring that contains the methoxy groups is nestled between residues T206 and M209 on one S6 helix, and M174, T175 and L176 at the bottom of the P-loop of a neighboring subunit. The brominated aromatic ring is positioned near the T206 residue on S6 of the subunit opposite of the M174 interactions, meaning the two S6 helices involved in drug interactions are neighboring, similar to Cav1.2 binding. A weak anomalous signal for bromine was found within the drug density, however it is not above anomalous signal noise found throughout the protein.

Crystals of CavAb (DDN) revealed calcium coordination in the selectivity filter at all three sites discussed in the selectivity filter studies (Figure 2.2). The tertiary amine of bromoverapamil is 5 Å directly below the lowest calcium bound in the selectivity filter, physically blocking calcium permeation, in a position predicted from docking studies (Figure 4.5).

The CavAb (DDN)-bromoverapamil structure was significantly twinned and analyzed the data without using the twin law. Surprisingly, repetitive application of multiple refinement procedures allowed refinement to an $R_w/R_f$ of .251/.294.

Gamal El-Din shows that the mutations of T206 discussed above cause a significant change in the $IC_{50}$ of bromoverapamil. A mutation of T206S causes a shift from 810nM to 24 μM for the state-dependent $IC_{50}$. For resting state inhibition, the $IC_{50}$ shifts from 24 μM to 115 μM. This confirms the importance of the T206 residue in PAA binding in CavAb, and supports the structural results. Extended biophysical analysis can be found in L. Tang and T. Gamal El-Din *et al.*, 2016.

### 4.6 Dihydropyridine Results

(-)BayK8644 is a well-known DHP that is a Cav1.2 agonist, increasing the open probability of the channel during stimulation (Striessnig et al., 1998). Interestingly, it's enantiomer, (+)BayK8644, is an antagonist of Cav1.2. A total of five CavAb- (-)BayK8644 complex datasets were collected, with resolutions ranging from 3.5 Å to 3.8 Å, all of which were not twinned. No drug density was seen in the expected DHP binding site, however a large density is seen below the lipid layer in the pore, similar to the location of UK-59811 (discussed below).

### 4.7 Published Dihydropyridine Results

Expanded results and discussion from this section are published in: Tang, L., Gamal El-Din, T.M., Swanson, T.M., Pryde, D., Scheuer, T., Zheng, N., Catterall, W.A., Structural basis for inhibition of a voltage-gated $Ca^{2+}$ channel by $Ca^{2+}$ antagonist drugs. Nature 537, 117-121 (01 Sept 2016). Data statistics are found in **Table 4.1**.

L. Tang solved three crystal structures of CavAb (DDN)-W195Y with DHPs; nimodipine, amlodipine and UK-59811, and one of CavAb (DDN) with UK-59811 (Figure 4.9). These structures had a resolution of 3.2 Å and 3.3 Å and were twinned. The W195Y mutation was made to mimic a Cav1.1 residue at that position.

Despite CavAb being a homotetramer, only one molecule of amlodipine and nimodipine were observed in the crystal structures. Presumably, the binding of one molecule has an allosteric effect on the other potential binding sites, rendering them incapable of binding drug. The binding site was found to be approximately one helical turn higher (towards the extracellular space) than predicted from Cav1.2 mutagenesis studies and displaced DMPC molecules that are normally bound there in the absence of drug.

DHP binding produced an asymmetry in CavAb that extended all the way to the selectivity filter, which is presumably how it induces block of the channel, although the changes are very small. The densities observed in the selectivity filter show that at site 1, the calcium ion is no longer coordinated equally by all subunits, but rather off to one side and potentially partially dehydrated. This is in contrast to the fully hydrated calcium ions seen in previous studies. The asymmetry-induced dehydration of this ion is thought to prevent ion conductance.

UK-59811 binding was slightly different than amlodipine and nimodipine. First, the binding site was slightly lower than the canonical drugs, more closely mimicking the residues from Cav1.2. Anomalous diffraction from the bromine atom in UK-59811 confirmed its position in the complex with CavAb (DDN). Second, a second molecule of UK-59811 was seen in the base of the pore. It seems that UK-59811 has two binding sites in CavAb; in the DHP site and within the base of the pore, lower than where bromoverapamil was observed.

Gamal El-Din investigated the action of these drugs, showing that the $IC_{50}$ for CavAb (DDD) of amlodipine was 10 nM, nimodipine was 100 nM and UK-59811 was 194 nM. The W195Y mutation in the DHP binding site reduced the $IC_{50}$ to 508 nM for nimodipine. A mutation within the DHP binding site I199S showed changes in the $IC_{50}$s to 112 nM for amlodipine and 5.7 μM for nimodipine This position is within the DHP binding site and was mutated to validate the observed drug binding site. The change in $IC_{50}$ supports the structural data. Extended biophysical analysis can be found in L. Tang and T. Gamal El-Din *et al.*, 2016.

## 4.8 Multidrug Complexes

The phenylalkylamine and dihydropyridine drug classes obviously act on calcium channels in different manners, and their binding sites do not overlap each other. Because of this, both DHP and PAAs can be bound to a channel at the same time, and evidence suggests that there is an allosteric interaction between the two.

Due to the uncertainties of verapamil presence in the pore and conflicting results of bromoverapamil, I was curious to see if addition of the (-)BayK8644 agonist and bromoverapamil to CavAb simultaneously would show increased drug access to the pore and a cleaner PAA density. Unfortunately, complexes of (-)BayK8644 and bromoverapamil did not produce crystals of high enough quality for data collection.

Four crystals of CavAb-d40-I217C in complex with amlodipine and bromoverapamil were collected, in order to visualize the interaction of DHP antagonists with a PAA. CavAb-d40-I217C is the CavAb-I217C construct that has the last 40 residues removed, which essentially eliminates the C-terminal tail. This construct was used because of the potential for increased flexibility of the S6 segments without the large, restrictive four-helix bundle present. The datasets ranged from 3.3 Å to 3.8 Å, all of which were not twinned. None of these structures showed either drug present, despite following the same protocols that produced drug structures for publication.

## 4.9 Benzothiazepine Results

Crystallization of CavAb with diltiazem was attempted at multiple concentrations of drug, and with multiple CavAb constructs. A handful of datasets of CavAb-I217C with diltiazem did not produce crystals with a resolution under 4.0 Å, and these data were heavily twinned. The electron densities were unable to be interpreted. The CavAb-d40 construct did not produce diltiazem crystals. I hypothesized that diltiazem is more difficult to crystallize than PAA, despite their similar binding sites, because the larger, more rigid chemical structure of diltiazem has a harder time accessing the pore binding site.

## 4.10 Conclusions

The analysis presented here provides a basis for understanding the structural mechanisms of phenylalkylamine and dihydropyridine block of voltage-gated calcium channels. The binding sites visualized are clearly unique and distinct sites, and confirm previous mutagenesis data in Cav1.2. The binding sites and structural characteristics of drug block support functional data such as state dependence of binding. They also explain why DHPs are only effective when applied extracellularly, while PAAs are effective when applied intracellularly.

The similarities of CavAb and Cav1.2 functional data confirm that CavAb is a viable model for drug binding, and that the structural data presented will closely resemble drug binding in Cav1.2. These structures illustrate the mechanisms of calcium channel pharmacology and provide insight into the therapeutic uses and observations of the PAA and DHP drug classes. These structural models could provide a basis for future design of safer more effective calcium antagonists for clinical use.

## 4.11 Figures

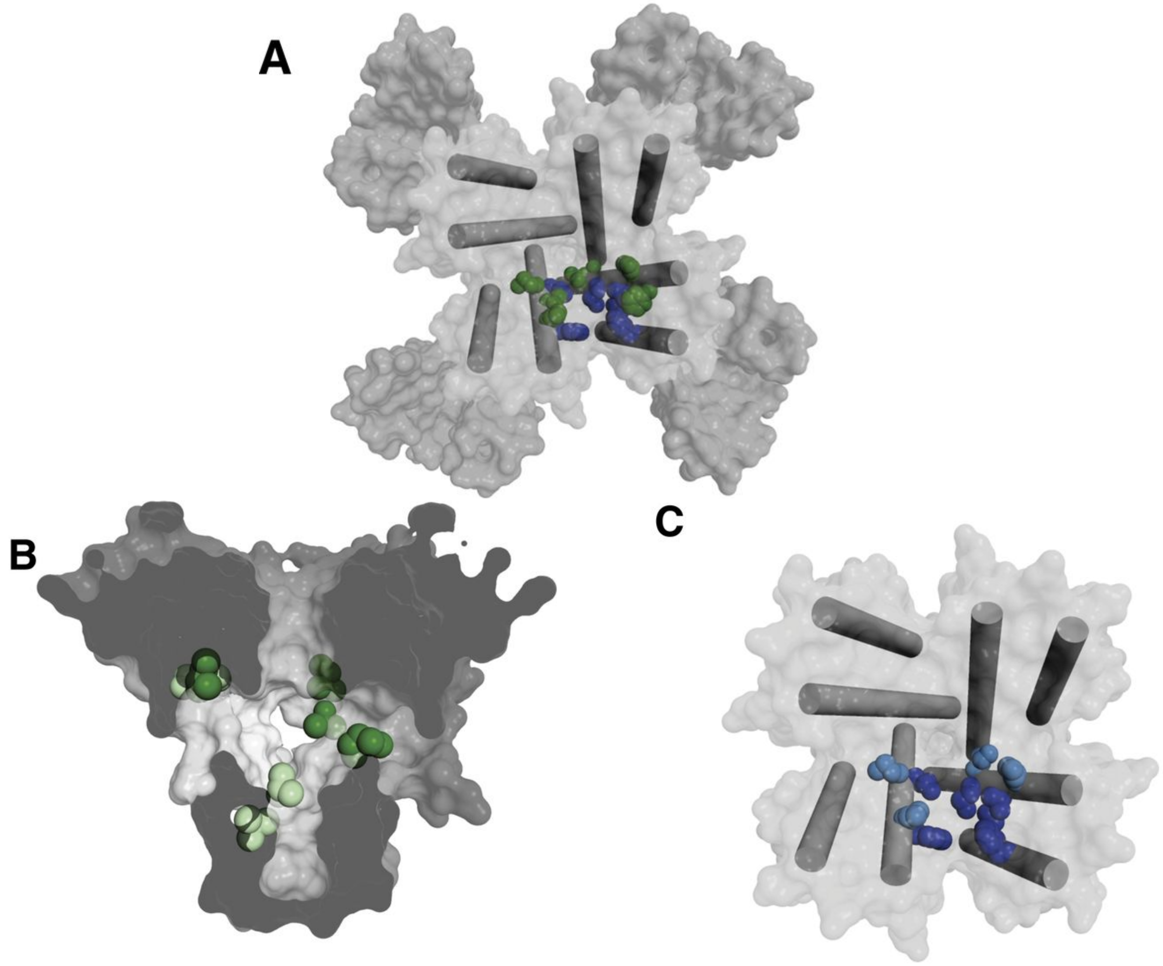

**Figure 4.1: Positions of Cav1.2 PAA and DHP binding sites in the NavAb structures.** Figure and legend adapted from Catterall and Swanson, *Molecular Pharmacology* 2015. Amino acid side chains in the phenylalkylamine-binding site. (A) Top view of the pore module of CavAb in the preopen state, with amino acid side chains analogous to those implicated in phenylalkylamine binding illustrated in green and amino acid side chains specific for dihydropyridine illustrated in blue. (B) Side view of CavAb in the slow-inactivated state, with amino acid side chains analogous to those implicated in phenylalkylamine binding illustrated in green. (C) Top view of the pore domain of CavAb in the preopen state, with amino acid side chains analogous to those implicated in dihydropyridine binding illustrated in blue.

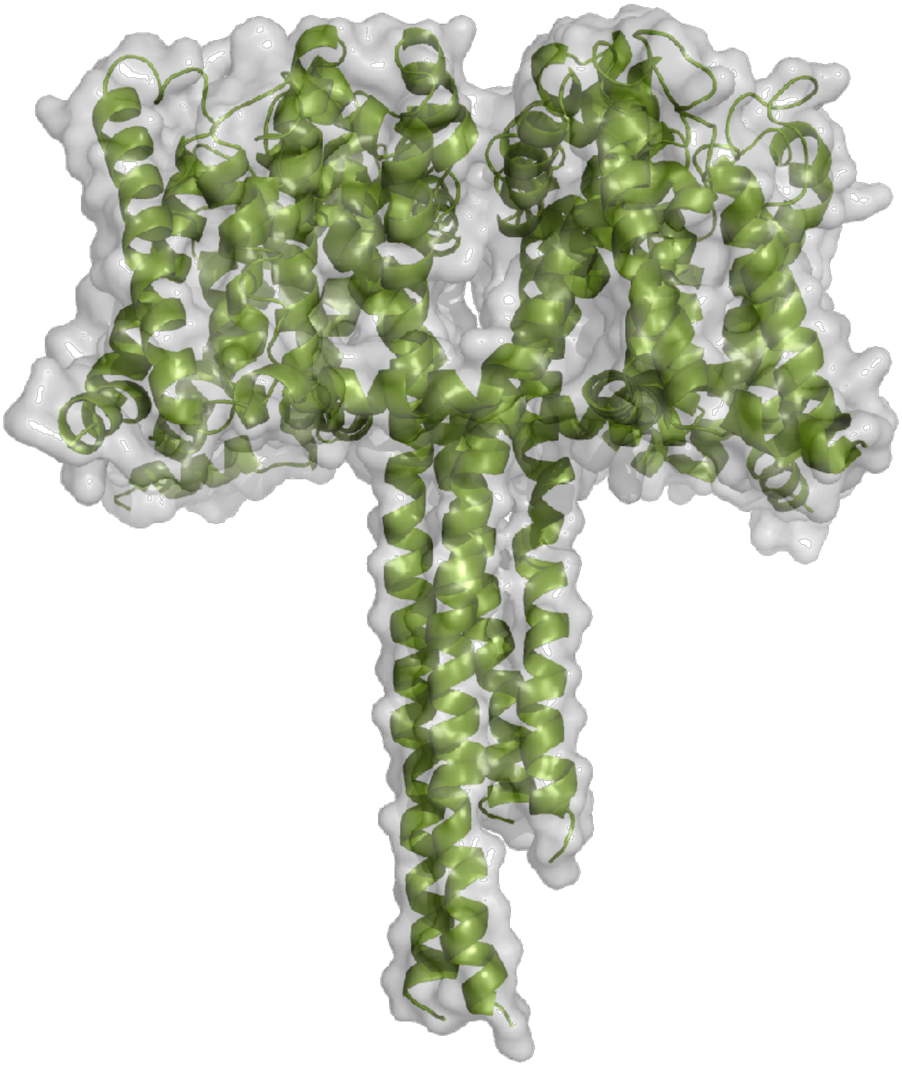

**Figure 4.2: CavAb in the presence of verapamil.** CavAb shows four subunits per asymmetric unit and a large C-terminal tail that extends into the cytoplasmic space.

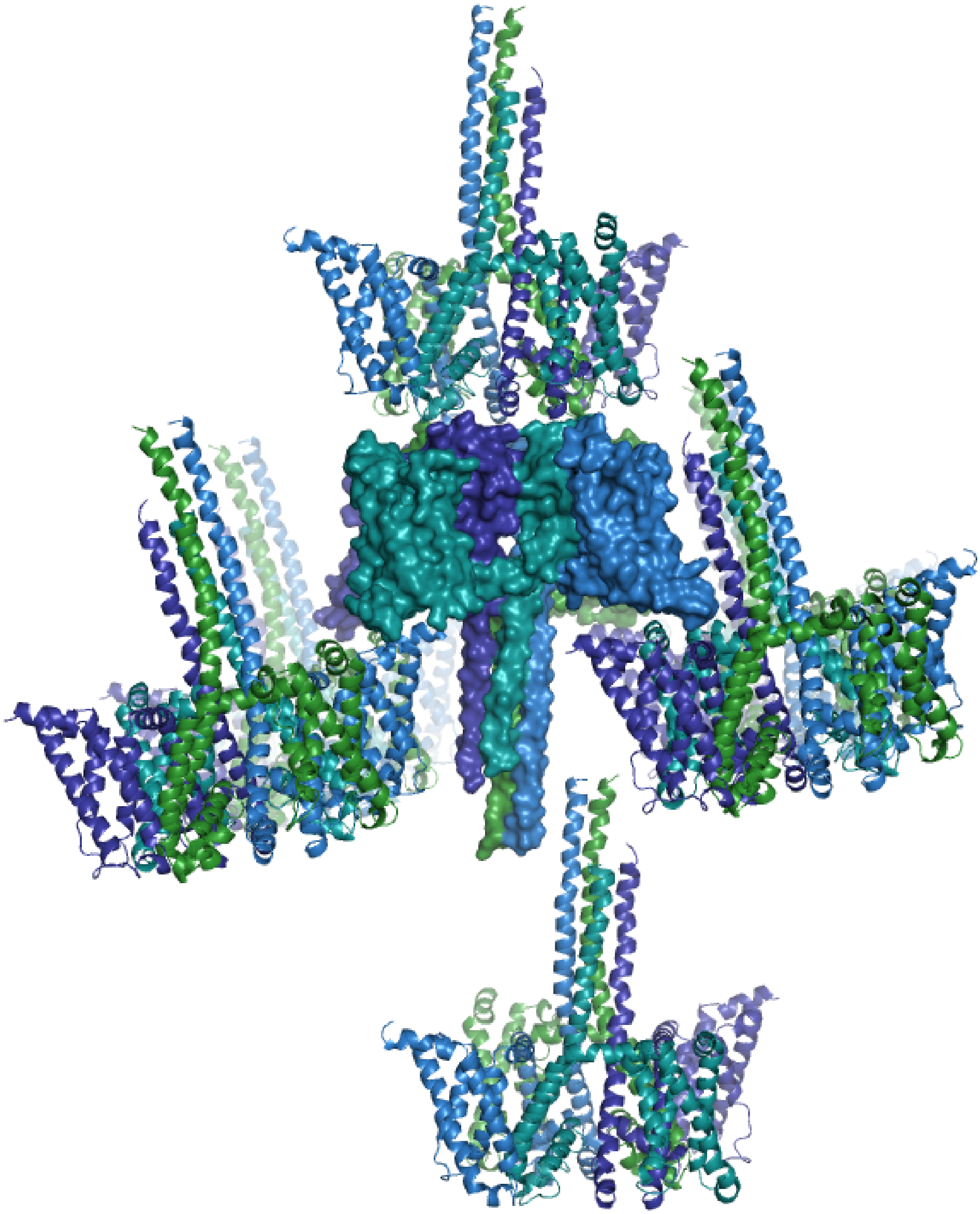

**Figure 4.3: CavAb crystal packing.** The four helix-bundle does not protrude straight into the cytoplasmic space, but rather curves to accommodate crystal packing. The proteins in the crystal lattice is no longer oriented straight together, but rather tilted because of the C-terminal tail.

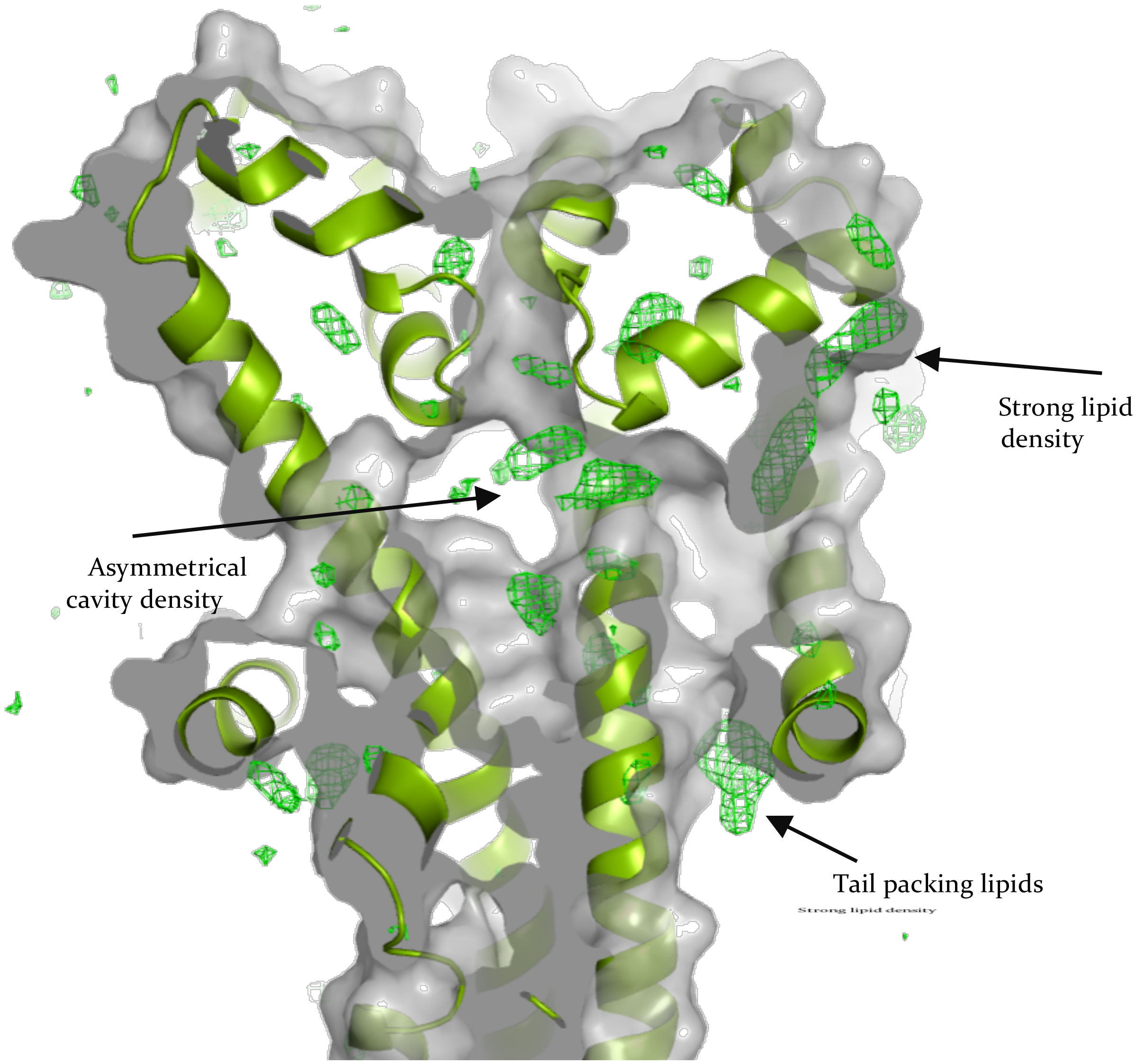

**Figure 4.4: Verapamil bound CavAb has distinct characteristics.** Three regularly observed characteristics of verapamil bound to CavAb are the presence strong lipid densities in the pore cleft, visible tail packing lipids and an asymmetrical cavity density. Green mesh is Fo-Fc map at 2σ.

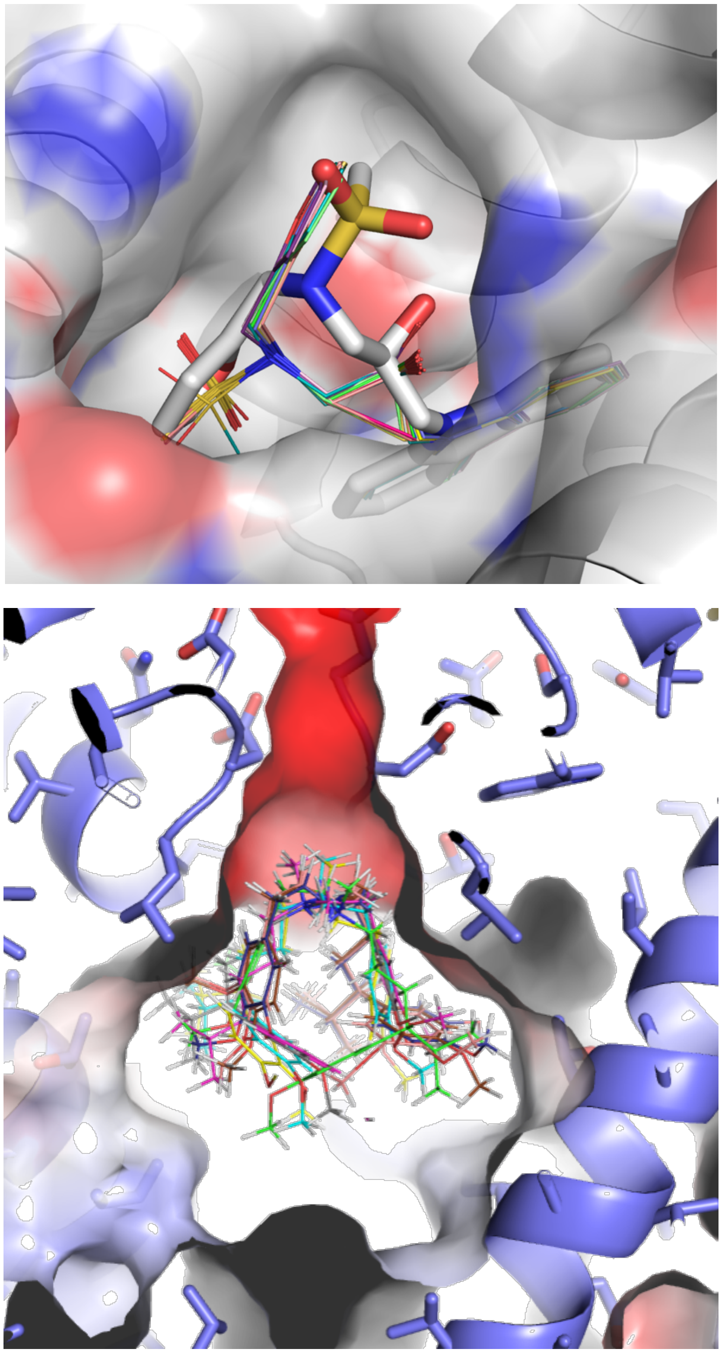

**Figure 4.5: DockThor results of mCry2-KL001 and CavAb-verapamil complexes.** *Top:* mCry2-KL001 complex, colored in grey, overlaid with KL001 placement by DockThor, in various colors and line representation. PDB accession code 4MLP. *Bottom:* DockThor shows verapamil docking to CavAb-verapamil structure in a manner that may explain the ambiguous pore density observed with verapamil binding. Protein is shown in purple cartoon, and surfaces are colored by charge. Five verapamil binding trajectories are shown in colored line representations.

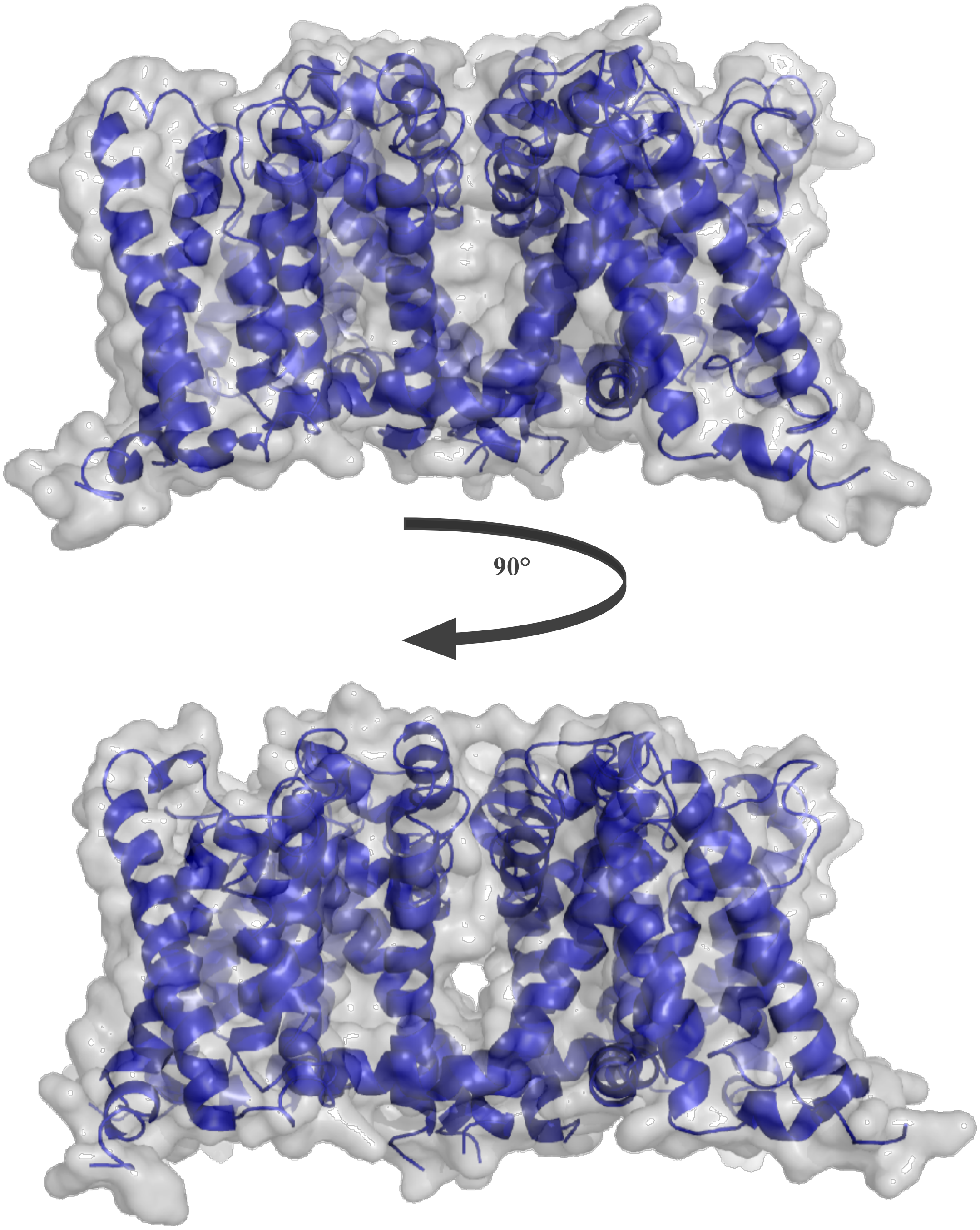

**Figure 4.6: Bromoverapamil causes structural changes in CavAb.** A view of CavAb-BV from the membrane shows a lack of C-terminal tail, as well as differences in fenestration size on different sides of the molecule.

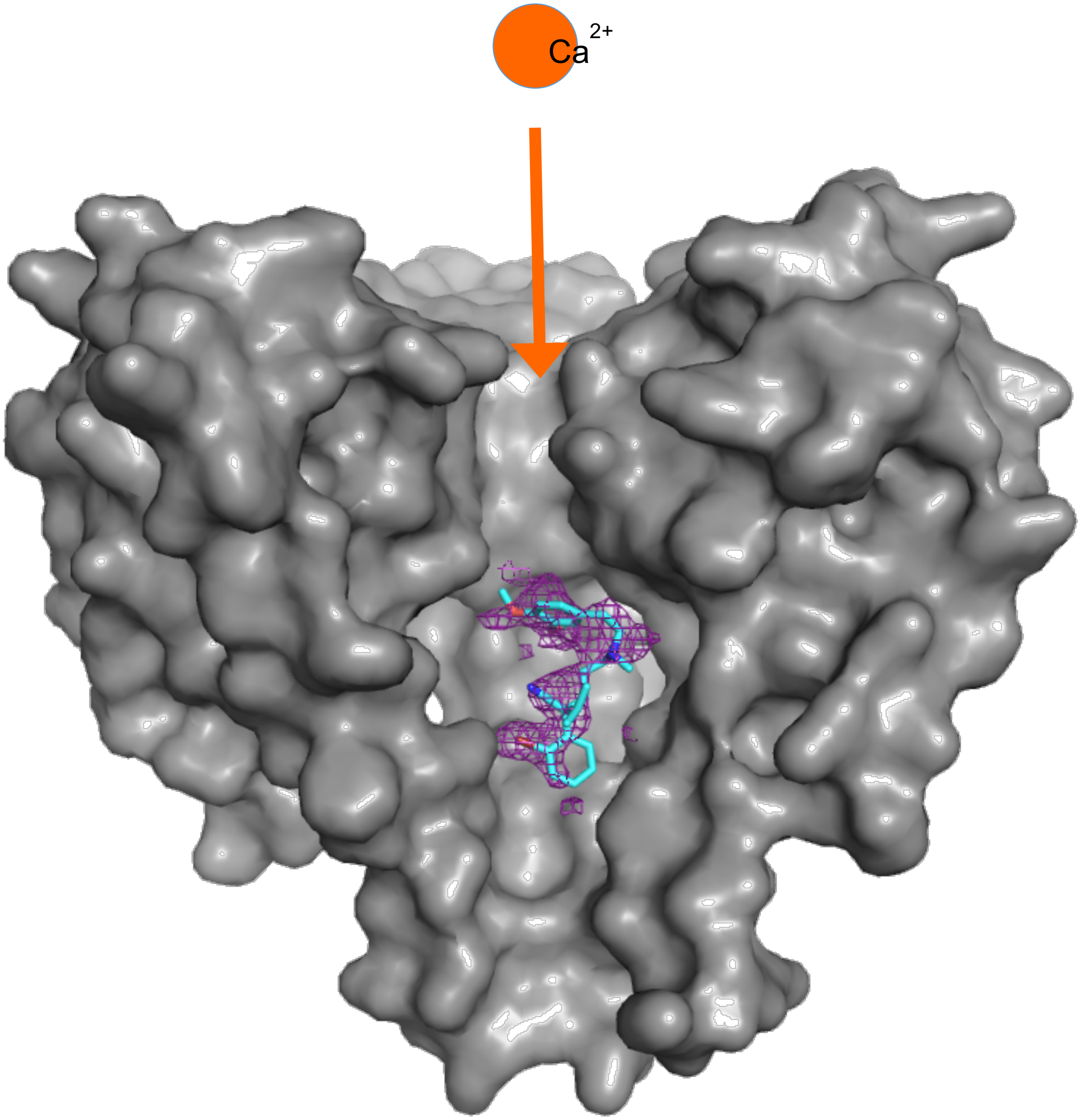

**Figure 4.7: Bromoverapamil shows a strong and identifiable density within the central cavity.** CavAb pore represented in surface rendering, with bromoverapamil in cyan stick. Fo-Fc electron density shown in purple mesh at 3.0σ. Calcium permeation path through the selectivity filter shown in orange.

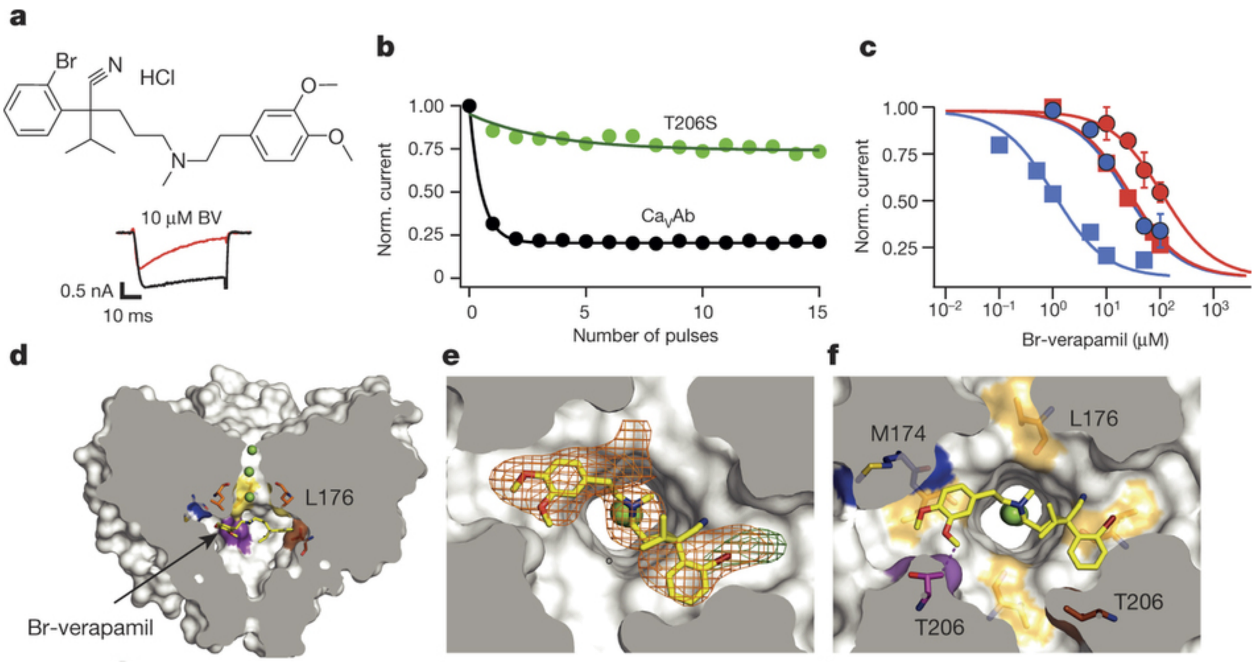

**Figure 4.8: Bromoverapamil bound to CavAb in a second orientation.** Figure and legend adapted from Tang and Gamal El-Din, *Nature*. 2016. **a**, Br-verapamil. Ba2+ current records for CavAb with 0 µM (black) and 10 µM (red) during the depolarizing pulse. **b**, State-dependent block of CavAb (*n* = 7) and CavAb T206S (*n* = 3) at 10 µM during trains of depolarizations at 1 Hz from –120 mV to 0 mV. The error bars for all the data points on this graph are too small to be visible. **c**, Inhibition by Br-verapamil for CavAb and CavAb T206S at *V* = –120 mV and following trains of depolarizations as in **b**. CavAb: resting state block, blue circles, IC50 = 24 ± 1.6 µM; state-dependent block, blue squares, IC50 = 810 ± 80 nM. CavAb T206S: resting state block, red circles, IC50 = 115 ± 3.2 µM; state-dependent block, red squares, IC50 = 24 ± 0.8 µM; *n* = 3–11; mean ± s.e.m. **d**, Side view of the pore module sectioned through the selectivity filter with Br-verapamil bound (yellow sticks). Ca2+, green spheres. **e**, *Fo*–*Fc* electron density (2.5σ, orange mesh) and anomalous scattering density (3σ, green mesh) for Br defines location of Br-verapamil. **f**, The two aromatic rings of verapamil are close to T206 of adjacent subunits.

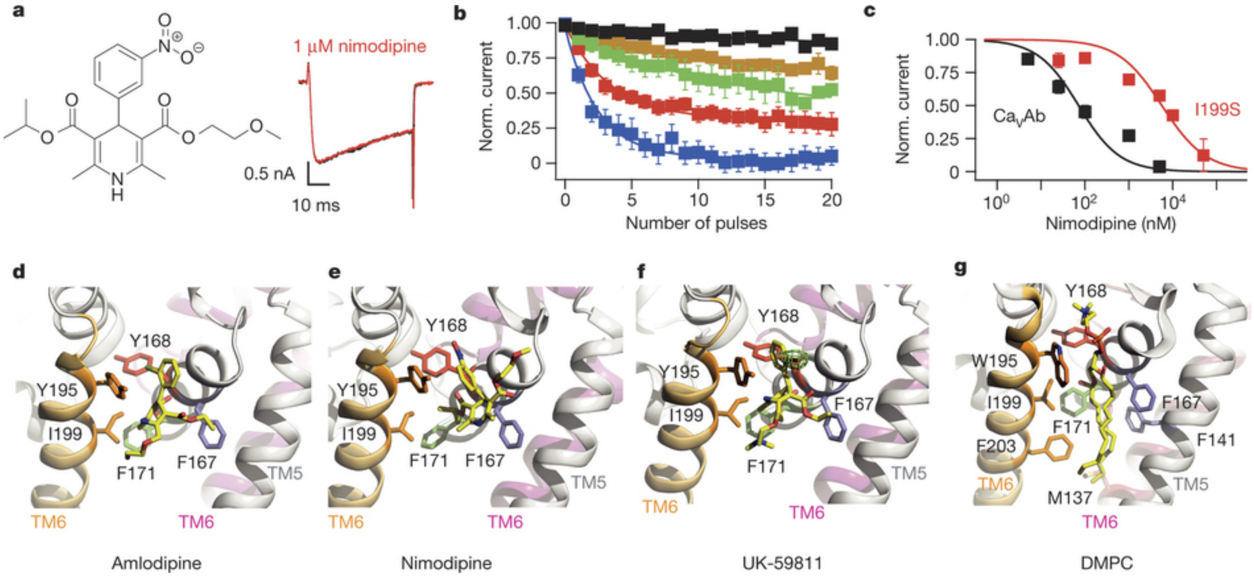

Amlodipine

Nimodipine

UK-59811

DMPC

**Figure 4.9: DHPs displace DMPC lipid at binding site.** Figure and legend adapted from Tang and Gamal El-Din, *Nature*. 2016. a, Nimodipine structure. Current records as in Fig. 1a. b, State-dependent block by nimodipine as in Fig. 1b: 5 nM (black), 25 nM (brown), 100 nM (green), 1 μM (red), and 5 μM (blue); mean ± s.e.m.; *n* = 3–14. c, Inhibition by nimodipine as in Fig. 1c. CavAb: IC50 = 100 ± 9 nM; CaVAb I199S, IC50 = 5.7 ± 0.6 μM; *n* = 3–14; mean ± s.e.m. d, Amlodipine (yellow sticks) bound to CavAb. S5 and S6 helices in ribbons; residues surrounding amlodipine in sticks. e, Nimodipine bound to CavAb. f, UK-59811 bound to CavAb. Anomalous scattering density (3σ, green mesh) for Br in UK-59811. g, DMPC lipid in the drug-free dihydropyridine-binding site in yellow sticks.

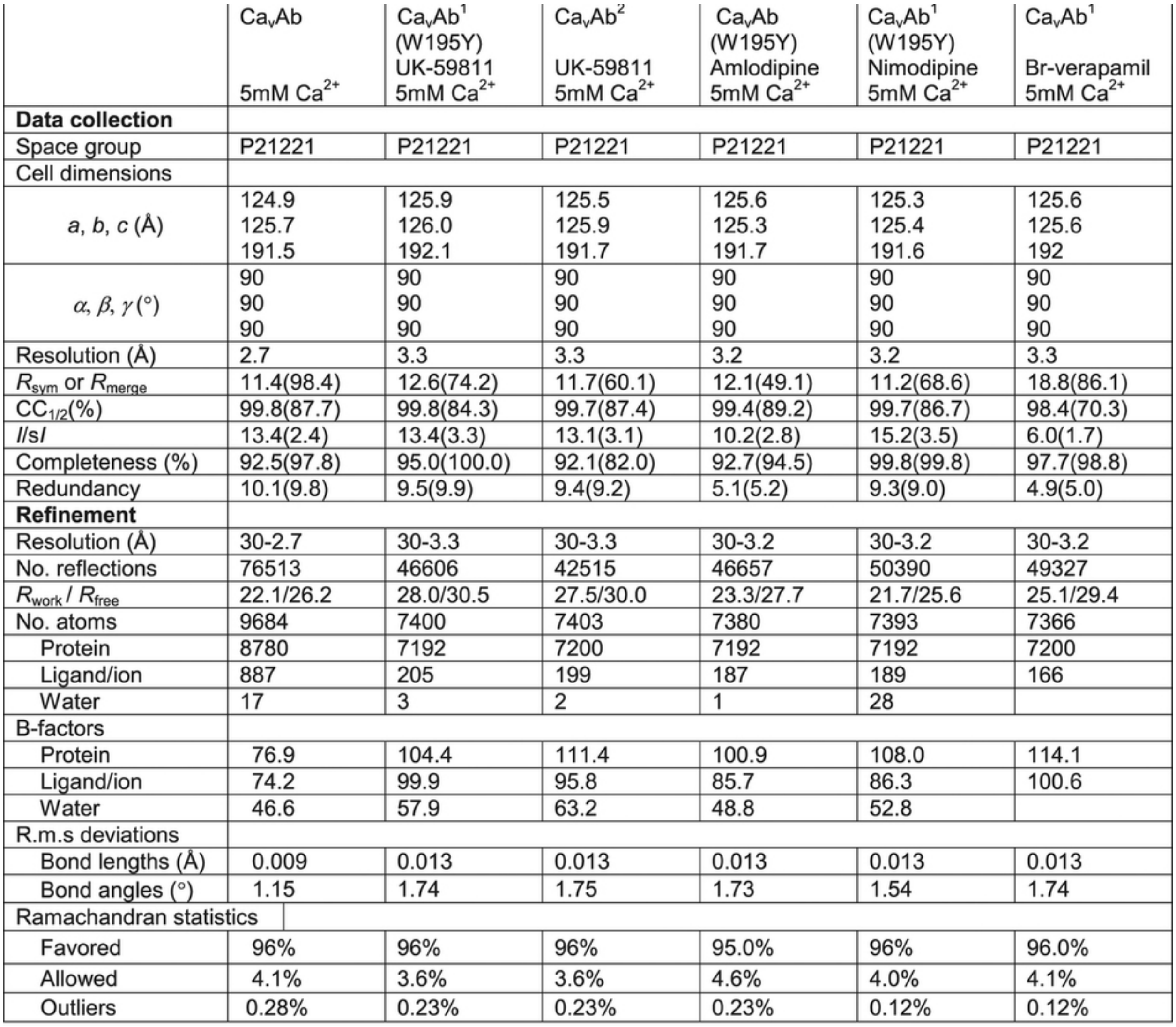

| | Ca$_v$Ab<br>5mM Ca$^{2+}$ | Ca$_v$Ab$^1$<br>(W195Y)<br>UK-59811<br>5mM Ca$^{2+}$ | Ca$_v$Ab$^2$<br>UK-59811<br>5mM Ca$^{2+}$ | Ca$_v$Ab<br>(W195Y)<br>Amlodipine<br>5mM Ca$^{2+}$ | Ca$_v$Ab$^1$<br>(W195Y)<br>Nimodipine<br>5mM Ca$^{2+}$ | Ca$_v$Ab$^1$<br>Br-verapamil<br>5mM Ca$^{2+}$ |
|---|---|---|---|---|---|---|
| **Data collection** | | | | | | |
| Space group | P21221 | P21221 | P21221 | P21221 | P21221 | P21221 |
| Cell dimensions | | | | | | |
| *a*, *b*, *c* (Å) | 124.9<br>125.7<br>191.5 | 125.9<br>126.0<br>192.1 | 125.5<br>125.9<br>191.7 | 125.6<br>125.3<br>191.7 | 125.3<br>125.4<br>191.6 | 125.6<br>125.6<br>192 |
| $\alpha$, $\beta$, $\gamma$ (°) | 90<br>90<br>90 | 90<br>90<br>90 | 90<br>90<br>90 | 90<br>90<br>90 | 90<br>90<br>90 | 90<br>90<br>90 |
| Resolution (Å) | 2.7 | 3.3 | 3.3 | 3.2 | 3.2 | 3.3 |
| $R_{\mathrm{sym}}$ or $R_{\mathrm{merge}}$ | 11.4(98.4) | 12.6(74.2) | 11.7(60.1) | 12.1(49.1) | 11.2(68.6) | 18.8(86.1) |
| CC$_{1/2}$(%) | 99.8(87.7) | 99.8(84.3) | 99.7(87.4) | 99.4(89.2) | 99.7(86.7) | 98.4(70.3) |
| *I*/s*I* | 13.4(2.4) | 13.4(3.3) | 13.1(3.1) | 10.2(2.8) | 15.2(3.5) | 6.0(1.7) |
| Completeness (%) | 92.5(97.8) | 95.0(100.0) | 92.1(82.0) | 92.7(94.5) | 99.8(99.8) | 97.7(98.8) |
| Redundancy | 10.1(9.8) | 9.5(9.9) | 9.4(9.2) | 5.1(5.2) | 9.3(9.0) | 4.9(5.0) |
| **Refinement** | | | | | | |
| Resolution (Å) | 30-2.7 | 30-3.3 | 30-3.3 | 30-3.2 | 30-3.2 | 30-3.2 |
| No. reflections | 76513 | 46606 | 42515 | 46657 | 50390 | 49327 |
| $R_{\mathrm{work}}$ / $R_{\mathrm{free}}$ | 22.1/26.2 | 28.0/30.5 | 27.5/30.0 | 23.3/27.7 | 21.7/25.6 | 25.1/29.4 |
| No. atoms | 9684 | 7400 | 7403 | 7380 | 7393 | 7366 |
| Protein | 8780 | 7192 | 7200 | 7192 | 7192 | 7200 |
| Ligand/ion | 887 | 205 | 199 | 187 | 189 | 166 |
| Water | 17 | 3 | 2 | 1 | 28 | |
| B-factors | | | | | | |
| Protein | 76.9 | 104.4 | 111.4 | 100.9 | 108.0 | 114.1 |
| Ligand/ion | 74.2 | 99.9 | 95.8 | 85.7 | 86.3 | 100.6 |
| Water | 46.6 | 57.9 | 63.2 | 48.8 | 52.8 | |
| R.m.s deviations | | | | | | |
| Bond lengths (Å) | 0.009 | 0.013 | 0.013 | 0.013 | 0.013 | 0.013 |
| Bond angles (°) | 1.15 | 1.74 | 1.75 | 1.73 | 1.54 | 1.74 |
| Ramachandran statistics | | | | | | |
| Favored | 96% | 96% | 96% | 95.0% | 96% | 96.0% |
| Allowed | 4.1% | 3.6% | 3.6% | 4.6% | 4.0% | 4.1% |
| Outliers | 0.28% | 0.23% | 0.23% | 0.23% | 0.12% | 0.12% |

**Table 4.1: Published Data.** Datasets from this table were collected and processed by L. Tang, and reported in Tang, L., Gamal El-Din, T.M., Swanson, T.M., Pryde, D., Scheuer, T., Zheng, N., Catterall, W.A., Structural basis for inhibition of a voltage-gated Ca2+ channel by Ca2+ antagonist drugs. Nature 537, 117-121 (01 Sept 2016).

[1] This data set is collected at 0.9198 Å.

[2] This data set is collected at 1.75 Å.

All other data sets are collected at 1.0 Å.

# 5 TIMOTHY SYNDROME

## 5.1 Introduction

Timothy Syndrome is a rare autosomal dominant genetic disorder caused by a point mutation in the CACNA1C gene, which encodes the Cav1.2 channel . The prevalence of Cav1.2 throughout a variety of tissues leads to both neurological as well as physical and developmental defects. Patients with Timothy Syndrome will display prominent cardiac symptoms that include Long QT syndrome, structural heart defects and arrhythmias. Neurologically, these patients often have autism spectrum disorder (Bader et al., 2011). The most prevalent comorbidity is syndactyly, or finger webbing (Splawski et al., 2004).

### *5.1.1 Prognosis and Treatment*

Timothy Syndrome often results in childhood death, with an average age of death of 2.5 years, but some patients have been known to survive into adulthood . Children usually die from arrhythmias. There are a few cases of genetic mosaicity reported, and the symptoms in these patients are very mild, sometimes non-existent (Splawski et al., 2005).

Treatment of Timothy Syndrome consists mainly of repairing physical defects and addressing the detrimental cardiac issues. Surgery can be an option for removal of finger webbing and reparation of some heart defects. Medications may be used to try to control Long QT syndrome as well as arrhythmias such as beta-blockers or propanalol. Logically, Cav channel blockers may be of use, as faulty calcium currents are implicated in the disease.

### *5.1.2 Cav1.2 Mutations*

Timothy Syndrome is caused by point mutations in the Cav1.2 activation gate (Splawski et al., 2005). Both classical (type-1) and atypical (type-2) mutations are found within the gate region at the bottom of the DI S6 helix that lines the pore. This region is believed to be helical in nature in the wild type protein, which is confirmed by the recent Cav1.1 cryo-electron microscopy structures (Figure 6.1) (Wu et al., 2016; 2015)

Type-1 Timothy Syndrome is caused by a G406R mutation, which introduces a long, positively charged amino acid in place of the flexible glycine (Figure 5.1). This mutation is within exon 8a of CACNA1C, a splice variant that is expressed at low levels.

The atypical form is caused by a mutation on exon 8 of CACNA1C, which is expressed at much higher levels than exon 8a. The same mutation found in Type-1 could occur, G406R, or a mutation in G402S, which adds the serine hydroxyl group and a beta carbon.

### *5.1.3 Physiology*

Timothy Syndrome mutations in Cav1.2 cause a removal of the channels voltage-dependent inactivation (Barrett & Tsien, 2008) (Figure 5.2); Cav1.2 is no longer able to close properly after being opened. Lack of channel inactivation leads to a larger influx of $Ca^{2+}$ ions into the cell. A great calcium current will lead to delayed repolarization of the action potential, which uncouples action potentials in different chambers of the heart, leading to arrhythmias.

### *5.1.4 CavAb as a Model*

A sequence alignment of Cav1.2_DI and CavAb show that the two positions disrupted in Timothy Syndrome, Cav1.2 G402 and G406 are equivalent to CavAb positions A215 and

D219 (Figure 5.3). While CavAb differs a lot from Cav1.2, the helical nature of the activation gate seemed to be conserved between proteins. Secondary structure predications of Cav1.2 showed that the locations of the mutations were still within a helical region of the protein, and this was confirmed recently by the Cav1.1 cryo-electron microscopy structures (Figure 5.4).

We hypothesized that the insertion of Timothy Syndrome mutations into CavAb would reveal a structural mechanism for the loss of voltage-dependent inactivation in Cav1.2. Any structural change due to the mutations should be amplified and easy to detect due to the homotetrameric nature of CavAb. CavAb-d27 and CavAb-d40-I217C had revealed different placements of the S6 helix, which provided two different backgrounds to pursue these mutations on. CavAb-d27 shows a structure very similar to full length CavAb and CavAb-d40-I217C displays a more open activation gate, holding the bottom of the S6 closer to the S4-S5 linker. The CavAb-d40-I217C structure more closely mimics the pore conformation seen in the Cav1.1 structure.

## 5.2 Research Strategy

In order to avoid twinning and potential crystallization artifacts from the full length tail, four Timothy Syndrome mutations were introduced to CavAb-d27. Since neither of these CavAb positions contain the glycine (G) seen in Cav1.2, I first mutated each of these positions to create the CavAb-d27-A215G and CavAb-d27-D219G positions. These will be referred to as the Timothy Syndrome background mutants. The disease mutations in Timothy Syndrome, G402S and G406R, were put in to the CavAb-d27 construct as well to create CavAb-d27-A215S and CavAb-d27-D219R.

A second background construct was used as well, CavAb-d40. CavAb-d40-I217C was briefly used in the drug binding studies (data not shown). Datasets without drug present had also been collected, and examination of these apo structures revealed different spatial relationships between the A215 and D219 sites with the S4-S5 linker than are seen with the CavAb-d27 constructs. The same four mutations were added to CavAb-d40. I hypothesized that the d40 constructs may see a greater change than the d27 constructs between Timothy syndrome background and disease mutations due to the increased flexibility of the final residues as well as their placement close to the linker.

The I217C mutation was not used in these studies, as it is within one helical turn of each of the positions of interest, and well within the region of the protein we would expect structural changes to emerge. It is not a disease relevant mutation, and did not affect crystal formation in the drug binding studies.

## 5.3 Results

The structural work presented here has yet to be published. It is the sole work of myself, Teresa Swanson, under the guidance of Ning Zheng and Bill Catterall. Any electrophysiological data presented is the work of Tamer Gamal El-Din.

While all four mutants were inserted into both CavAb-d27 and CavAb-d40, only the d27 constructs formed crystals readily. CavAb-d40 without the I217C mutation did not produce crystals that would grow large enough for harvesting and data collection. Since I had already decided that I did not want to introduce the I217c mutation into this system to aid in crystallization, only the d27 constructs were pursued.

### *5.3.1 Type-1 and Type-2 D219 Mutations*

Ten datasets of CabvAb-d27-D219G were collected for the Timothy Syndrome investigations (for other structures of this construct in the presence of ions and chelators, see Chapter 3). These datasets had a resolution range of 2.3 Å to 2.85 Å with an average resolution of 2.55 Å. The crystals formed three distinct shapes within the crystallization trays; a rod, a cone and a cube. These crystal shapes could sometimes be found within the same crystal well. The crystal shape did not change the space group observed, resolution did not seem to depend on the shape of the crystal, and the structures between the crystal shapes were the same. There were no indications in data quality as to why the crystals were different shapes, nor did the shape have any effect on the quality. Four datasets of CavAb-d27-D219R were collected with a resolution range of 2.45 Å to 3.05 Å, and an average resolution of 2.78 Å.

### *5.3.2 Activation Gate of D219 Mutations*

One of the major difference between D219G and D219R is seen in the immediate vicinity of the activation gate. In the space between the C-terminal tail and the S4-S5 linker, we see electron densities that have been interpreted as CHAPSO detergent molecule head groups in the D219R mutations, but not the D219G (Figure 5.5, top). CHAPSO is a zwitterionic detergent, with a large ring structure that's been seen in crystal structures previously. Interestingly, eight CHAPSO head groups are seen packed around the tail in constructs that have either a negative aspartate or a positive arginine at position 219, but not in the constructs with a neutral glycine. As a result of no detergent molecules present, the D219G mutation has a slightly bowed four-helical bundle (Figure 5.5, bottom).

### *5.3.3 Type-2 A215 Mutations*

Three datasets of CavAb-d27-A215G and two data sets of CavAb-d27-A215S were collected. The average resolution for A215G was 2.75 Å and was 2.55 Å for A215S. Surprisingly, the structures of these two mutants do not appear to be significantly different from each other (Figure 5.6). The entire transmembrane domain aligns nearly perfectly, and remain unchanged from previous structures. Only small changes are seen in the C-terminal tail. At the position of A215G/S, the S6 helices are aligned well.

For both of these A215 mutations, the detergent molecules that pack around the C-terminal tail were present. A total of eight detergent molecules can be seen packing around the tail, just between the tail and the S4-S5 linker.

### *5.3.4 Lipid Molecules at High Resolution*

The high resolution of these constructs allows for better visualization of DMPC molecules bound to CavAb. There are five DMPC molecules assigned in the highest resolution structure, 20 overall when accounting for symmetry. All lipid molecules can be visualized on the same face of the channel, when viewing from the membrane and looking directly at the fenestration (Figure 5.7).

The first molecule is found in the well-known pocket between the pore domains, where DHPs bind. We'll call these subunits "A" and "B". The other four DMPC molecules are all found at interfaces between the voltage-sensing and pore domains and two are in the extracellular leaflet of the bicelle membrane, while the other two are from the intracellular leaflet.

Two DMPC molecules are wedged between the S3 of the subunit “B” VSD and the S6 of subunit “A” pore domain. The head group lipid on the extracellular side actually packs close to the top of both the S5 and S6 helix of subunit “A”, and the tail is packed close to the loop connecting the top of the S3 and S4 helices on domain “B”. The head group from the intracellular leaflet DMPC is between the bottom of the S3 and the S4-S5 linker of the “B” subunit. One carbon chain tucks into a small crevice in that corner, while the other packs just outside the first carbon chain, mostly closing it off from the rest of the membrane.

The final two DMPC molecules can be found between the S4 of the VSD of subunit “C” and the S5 of the closest pore domain, subunit “B”, one from each leaflet of the bicelle membrane. The head group of the molecule on the extracellular side sits between the top of the S4 and top of the S5 helices that are in close proximity, with the tails packing along the interface. The DMPC molecule on the intracellular leaflet has a head group tucked between two small loops that connect helices. The first is the loop connecting the S4 and the S4-S5 linker. The second loop is on another subunit, the one connecting the S4-S5 linker to the S5 helix. The tails of this DMPC molecule pack along either side of the linker-S5 helix transition point.

### 5.4 Current Functional Progress

Most of the desired electrophysiological data on these Timothy Syndrome mutations has not been investigated or analyzed at this point. The constructs of A215G and A215S did not show calcium currents through the channels, although clear gating current is present. A215G shows Na+ current (data not shown). The D219G construct shows the same V1/2 as CavAb-d27, but roughly equivalent current when opened. The D219R mutation shows no calcium current through the channel, but has clear gating current. Tamer Gamal El-Din preformed all electrophysiology studies.

## 5.5 Conclusions

The numerous visible DMPC and CHAPSO molecules in these structures demonstrate the extent to which membrane composition can regulate and interact with ion channels. DMPC molecules are consistently seen bound to at least four distinct sites on the CavAb channel, one of which has been clearly seen before and three more that are described here. The CHAPSO molecules pack around the four-helical bundle, seemingly to help stabilize the close vicinity of the helices to each other.

The results presented here, while interesting, do not seem to model Timothy Syndrome in mammalian channels. While there are some structural changes between mutants, they are minute and provide no obvious mechanism for the loss of voltage dependent inactivation in mammalian channels. Preliminary functional studies do not show any obvious replication of loss of voltage-dependent inactivation either.

When choosing constructs for these studies, the I217C mutation was purposefully avoided because of its location between A215 and D219 on CavAb. However, the CavAb-d40-I217C construct best models the Cav1.1 DI activation gate and is placed closer to the S4-S5 linker than any other CavAb construct. Since CavAb-d40 did not crystallize well, and CavAb-d27 did not model Timothy Syndrome well, this is the next construct that should be attempted. The activation gate should be more flexible in CavAb-d40-I217C, and would potentially show greater structural changes with the S6 in closer proximity to the S4-S5 linker.

## 5.6 Figures

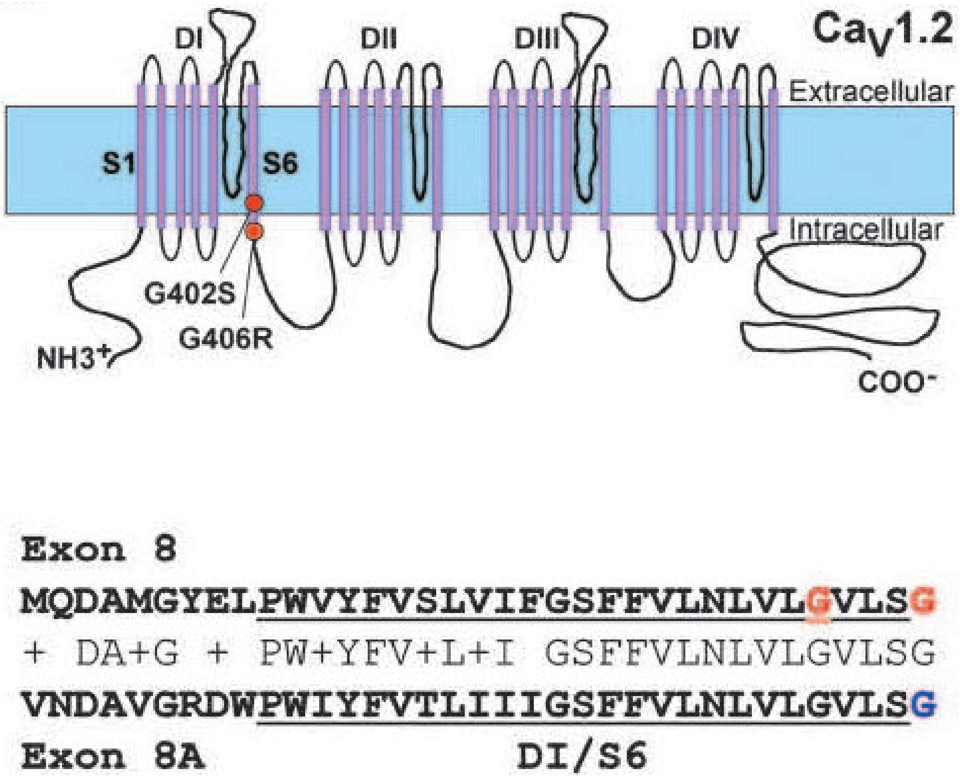

**Figure 5.1:** ***G402S and G406R mutations are found in DI_S6, near the activation gate.*** *Figure adapted from* Splawski, et al. Severe arrhythmia disorder caused by cardiac L-type calcium channels. PNAS 102 (23) 8089-96. June 7, 2005. Top: Location of mutations in the predicted topology of Cav1.2. Bottom: Sequence alignment of S6 helix for Exon 8 and 8a showing location of G402 and G406 (orange) and G406 (purple).

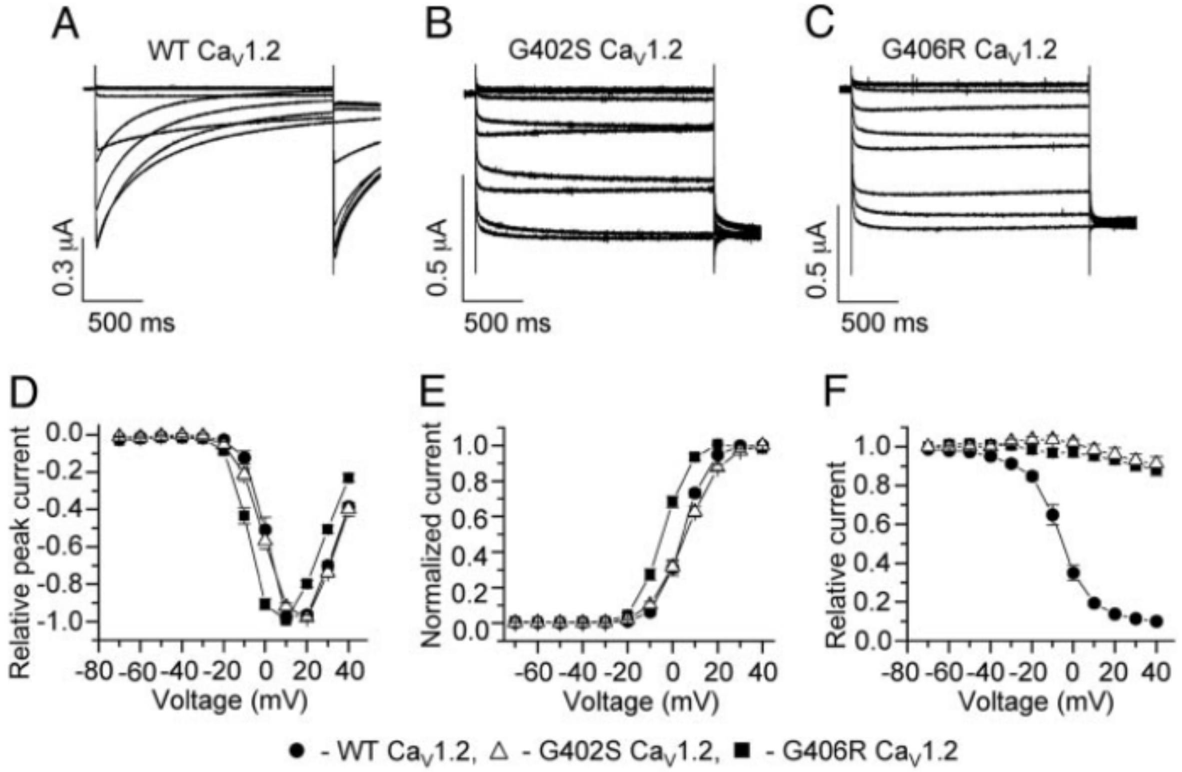

**Figure 5.2: Timothy Syndrome mutations in Cav1.2 remove voltage-dependent inactivation.** Figure from Splawski, *et al.* PNAS 2005. Mutations in exon 8 of Cav1.2, expressed in *Xenopus* oocytes with 40 mM BaCl2 external solution. Calcium currents through channels are shown in (A), (B), and (C). (D) IV curves show similar relationships with WT Cav1.2 (E) Voltage-dependent activation not significantly disrupted with mutations (F) Voltage-dependent inactivation is nearly abolished in mutant channels.

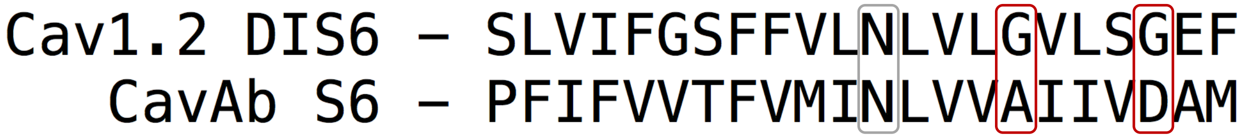

**Figure 5.3: Alignment of CavAb and Cav1.2_DIS6.** Strictly conserved asparagine is outlined in grey, while Cav1.2 positions 402 and 406 are outlined in red.

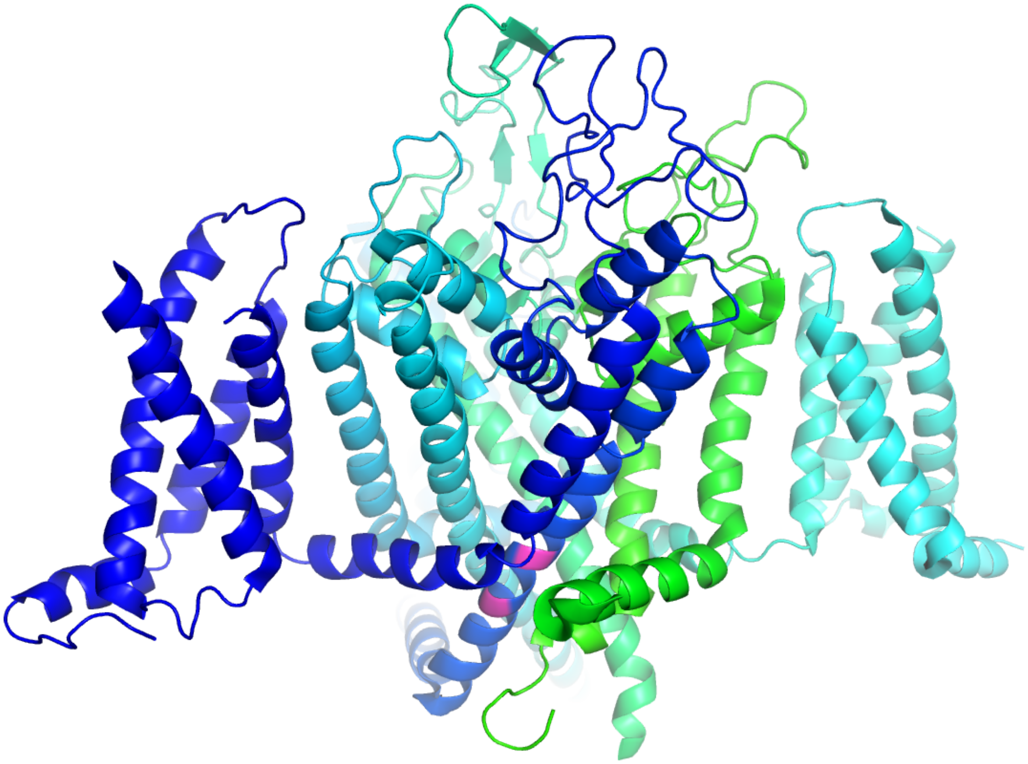

Figure 5.4: **Cav1.1 cryo-EM structure, α1 subunit.** Figure adapted from PDB accession code 5GJW. DI shown in blue, colored by rainbow. DIV shown in green. VSD and intracellular domain of DIV removed for clarity. Magenta residues are Timothy Syndrome mutations G402 and G406.

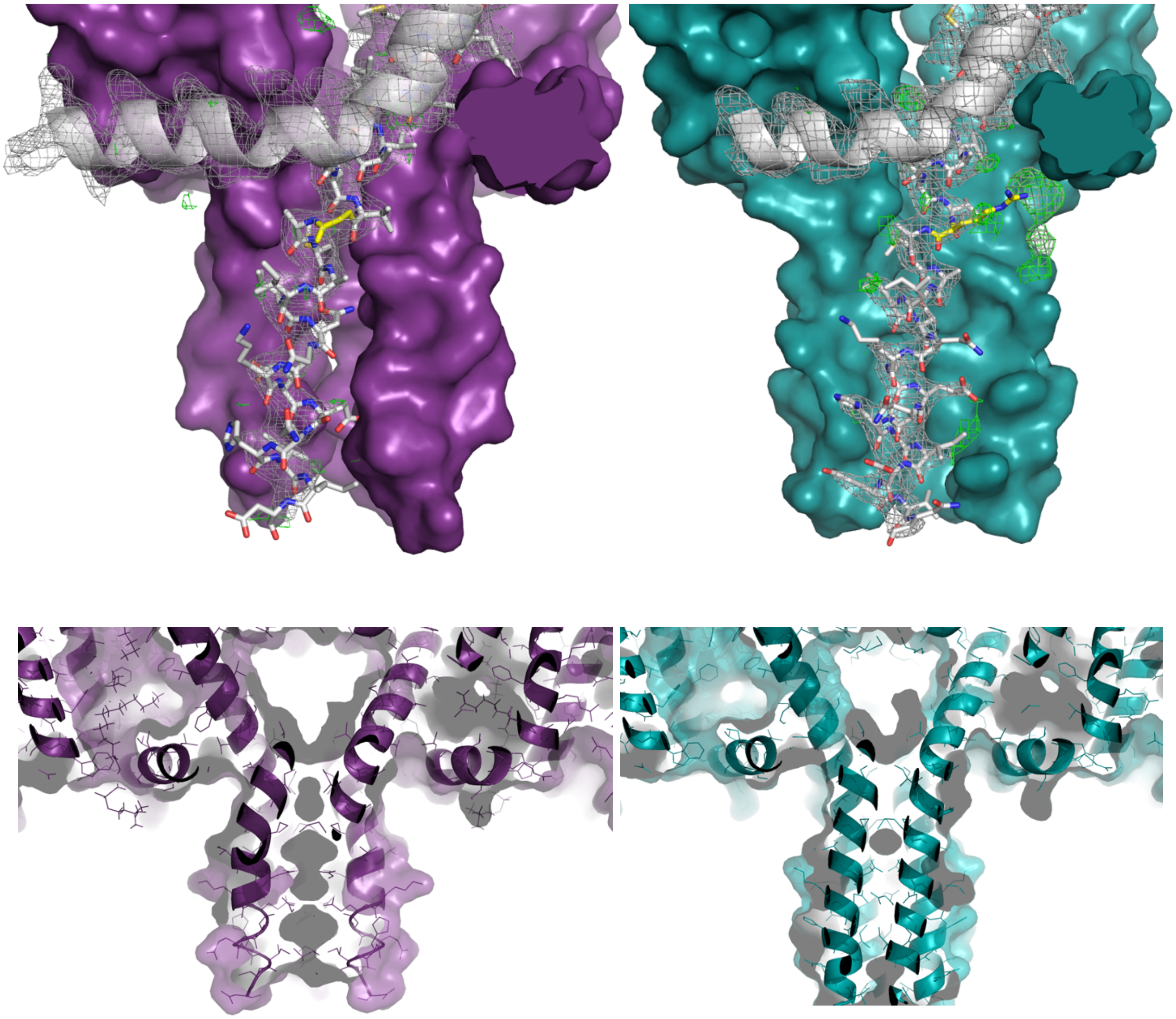

**Figure 5.5: Electron density of CHAPSO detergents is seen in the D219R mutation, but not the D219G.** CavAb-d27-D219G (purple, left) and CavAb-d27-D219R (teal, right). Top: D219G lacks Fo-Fc electron density around the top of the C-terminal tail. D219R shows strong Fo-Fc electron density (green mesh) at 3σ. Proteins are displayed with three subunits in surface representation. Fourth subunit is shown in grey, with the S4-S5 linker to S5 helix in cartoon, and the S6 to C-terminal tail in stick representation. Position 219 is shown in yellow stick. 2Fo-Fc at 2σ shown in grey mesh around one subunit. Bottom: D219G C-terminal tail is bowed compared to D219R, with greater space in the center of the four-helical bundle.

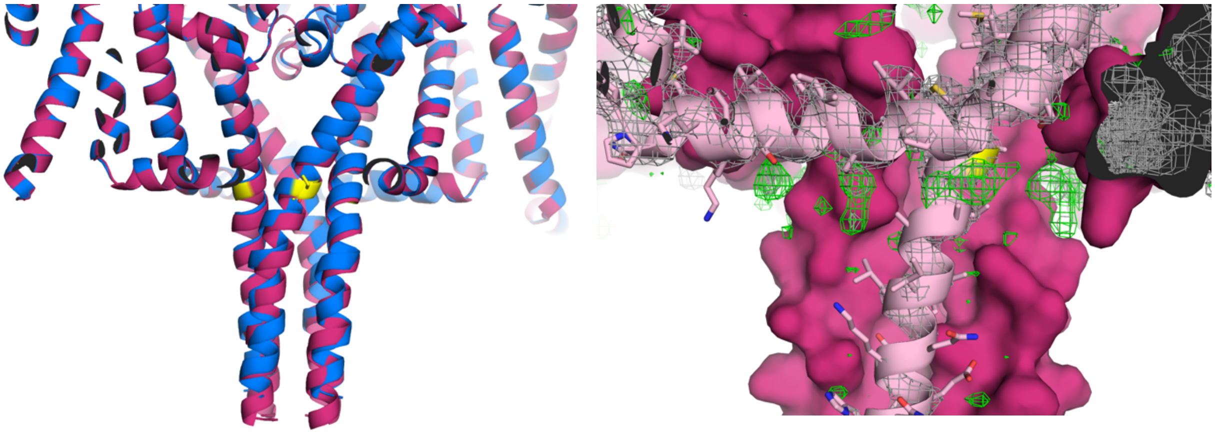

**Figure 5.6: A215 mutations are not significantly different from each other and contain CHAPSO detergent densities.** CavAb-d27-A215G in magenta, CavAb-d27-A215S in blue with position 215 shown in yellow sticks. Left: Protein alignment of A215G and A215S, in cartoon representation. Right: Sample visualization of detergent molecules around the C-terminal tail of A215S. Protein is displayed with three subunits in surface representation. Fourth subunit is shown in light pink, in cartoon and stick representation. Position A215S is shown in yellow stick. 2Fo-Fc at 2σ shown in grey mesh around one subunit and Fo-Fc mesh at 3σ in green mesh.

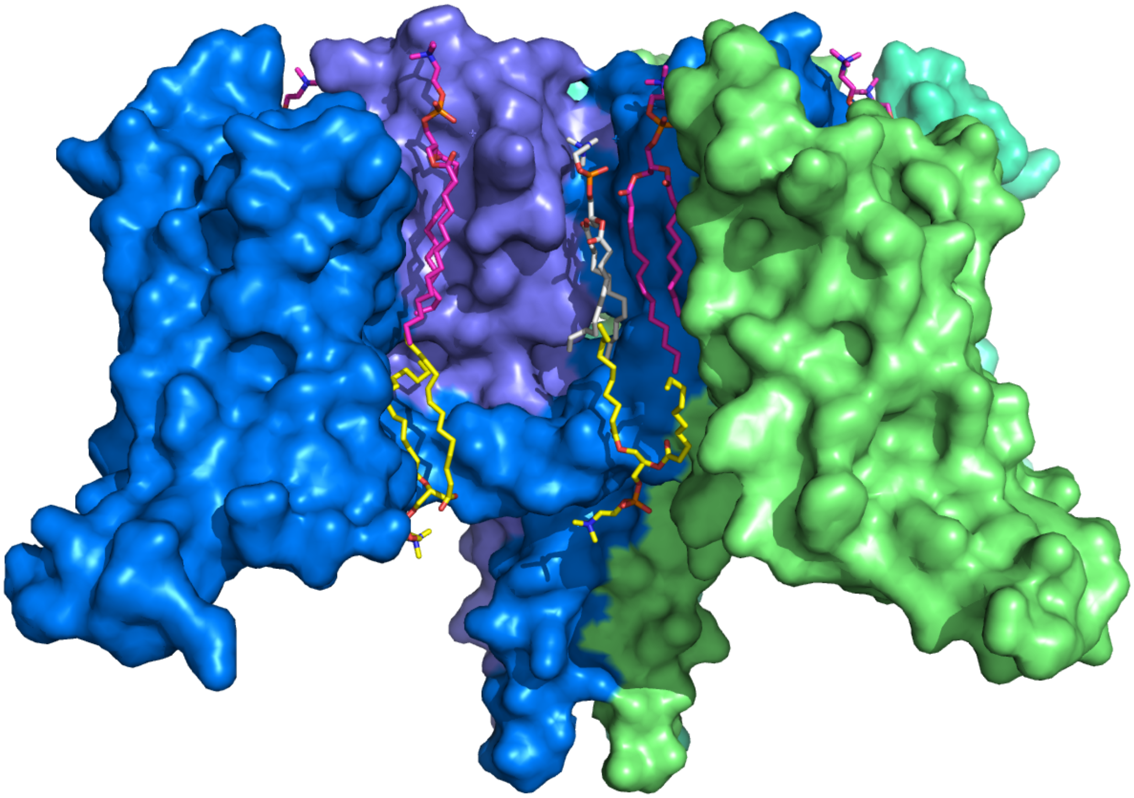

**Figure 5.7: CavAb-d27-D219G demonstrates positions of five resolved DMPC molecules**. Protein shown in surface representation, subunit “A” in purple, subunit “B” in blue, subunit “C” in green and subunit “D” in teal. DMPC molecules shown in sticks. DMPC in DHP binding site in grey, DMPC from extracellular leaflet in magenta and from intracellular leaflet in yellow. Five lipid molecules are present on every side of the protein, for a total of 20 visualized molecules.

# 6 DISCUSSION

## RELEVANCE OF CAVAB STUDIES TO MAMMALIAN CAV CHANNELS

With the recent publication of the rabbit Cav1.1 channel structure solved by cryo-electron microscopy (Wu et al., 2015; 2016) (Figure 6.1), we can directly compare the bacterial and mammalian structures in order to evaluate the true efficacy of our bacterial model. As expected, rCav1.1 is a large and complex structure that contains many regions that CavAb does not because of its homologous domains and multiple subunits. The best resolution achieved for this complex structure is 3.6 Å, which is enough resolution to see some side chain placements, although not all. The rCav1.1 structure contains not only the α1 subunit, but the β, α2δ and γ subunits as well, revealing the first look at the full complex and how the subunits directly interact. Complex loops and parts of the intracellular domain are also present in the cryo-EM structure. Overall, it is easy to see how the rCav1.1 structure is different from the CavAb channel.

However, when examining the transmembrane portions of the α1 subunit, the two channels are surprisingly similar. Structural alignment shows that the pore domains overlap quite well. The voltage-sensing domains of rCav1.1 are shifted a bit from their positions in CavAb, but not outside the realm of what has been observed in other bacterial channels (Figure 6.2). Since the studies in this thesis were focused on the pore domain of calcium channels, this alignment is of most relevance, and at first glance, CavAb looks to be a promising structural model for the rCav1.1 pore domain.

A structural alignment of the rCav1.1 and CavAb selectivity filter residues shows an impressive overlap in the placement of the backbone atoms, as well as the side chains of the amino acids (Figure 6.3). If we use the same nomenclature of Chapters 2 and 3, we can see the strictly conserved tryptophan as the 0 position as well as the -4 conserved threonine are nearly identically placed in both proteins, across all four domains. The backbone of these five amino acids (T and W included) overlap well and support the fact that these are the main determinants in calcium binding and selectivity, as demonstrated in Chapters 2 and 3. It also confirms the relevance of using a symmetrical, bacterial channel to studying the mammalian selectivity filter, despite an asymmetrical amino acid sequence.

An examination of the pore domains shows that again, CavAb provides an impressive model of rCav1.1 (Figure 6.4). All S5 and S6 helices, despite the domain, show only small changes in the position of the helix, meaning that the overall shape of the transmembrane pore domain remains relatively similar between proteins in the observed conformational states. This supports the extrapolation of the drug binding results—both phenylalkylamine and dihydropyridine—to mammalian calcium channels.

Mutations responsible for Timothy Syndrome are found in the activation gate of DI of the human Cav1.2 channel. The rCav1.1 structure shows that this region seems to deviate from the protrusion into the intracellular space in the way the CavAb C-terminal tail does. The bottom of the S6 helices instead kink more and splay open below the level of the membrane, even though the activation gate itself is closed (Figure 6.5). The DI S6 helix remains helical and does not bend until several helical turns after the sites of

Timothy Syndrome mutations, leading to the hypothesis that the helical CavAb S6 is a reasonable model for the mammalian channel in that region.

Interestingly, the DIV shows a drastic bend immediately following the activation gate which essentially ends up tucking the helix between the DI S6 helix and the S4-S5 linker of DIV. While at rest, this bend in the DIV S6 helix is neutral on the side facing the DI S6, it's possible that upon opening, the helix is twisted and the negative side of the helix ends up facing the DI S6. In a channel with a Timothy Syndrome mutation, this negative charge interaction with say, the G406R mutation, could potentially cause a hindrance to the channel inactivating that isn't there in the wild type. This bend in the DIV S6 helix is missing from the CavAb structure, and could explain why these mutations in CavAb did not accurately recapitulate the mammalian function. These differences in structure could explain why the Timothy Syndrome mutations in CavAb did now show changes that easily explain the mammalian disease channels lack of inactivation.

CavAb has proven to be an acceptably accurate model for mammalian channels, despite the numerous differences between bacterial and mammalian channels. From this comparison of the current studies on CavAb and the rCav1.1 cryo-EM structure, we can deduce that the pore domain of CavAb will provide the best model as opposed to other protein regions.

The CavAb crystallization studies presented here represent a compilation of ways bacterial channels can serve as a high resolution structural model for mammalian voltage-gated calcium channels. First, CavAb was a biophysical model to investigate calcium selectivity and answered decade-old questions about how calcium ions permeate through a selectivity filter. Second, CavAb was an effective drug-binding model for anti-arrhythmic and hypertension medications, leading to confirmation of binding sites and potential direction for future structure based drug design. Third, CavAb was used as a disease model to investigate the molecular basis of Timothy Syndrome. Even though CavAb is a distant ancestor to the mammalian calcium channels, it has proven to be a valuable tool for answering classic calcium channel questions.

## 6.1 Figures

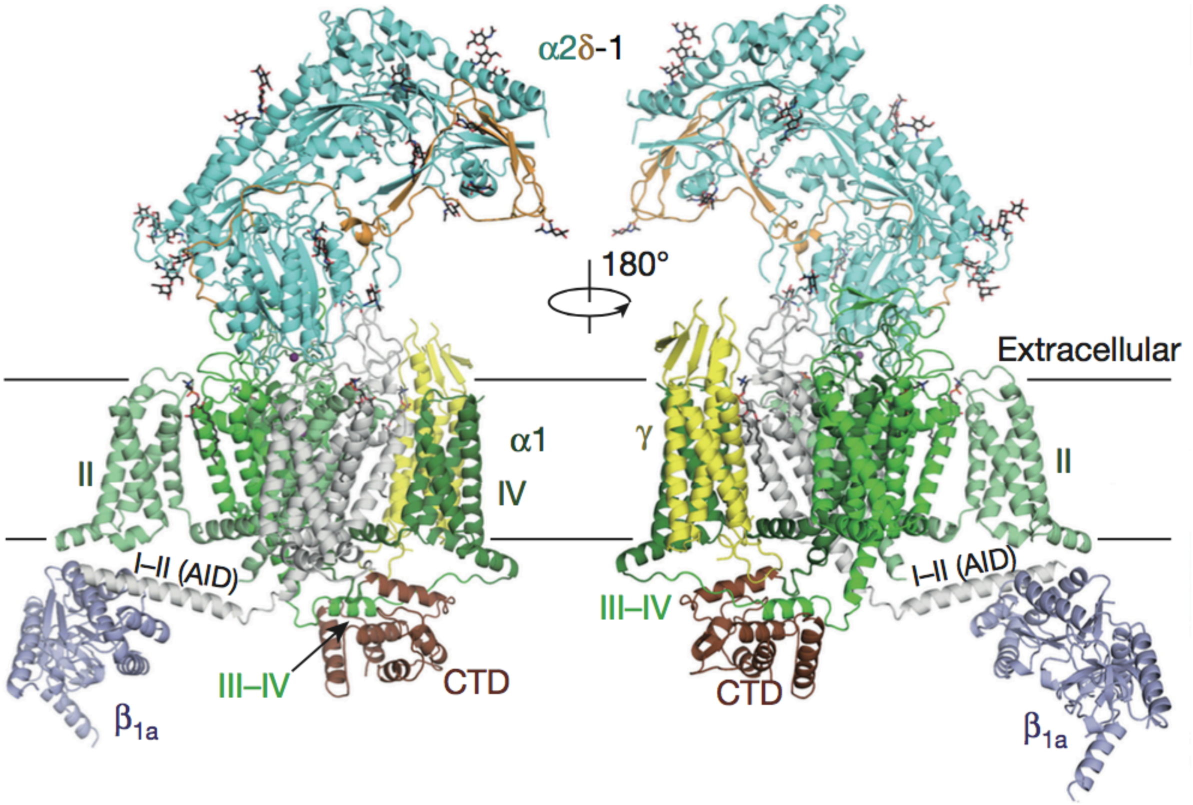

**Figure 6.1: rCav1.1 cryo-electron microscopy structure.** rCav1.1 is a complex structure containing the α1, β, α2δ and γ subunits. At 3.6 Å resolution, some ligand can be visualized as well, such as lipids and sugar moieties. Domains and subunits are each colored differently here, for ease of representation. Figure adapted from Wu, J., Yan, Z., Li, Z., Qian, X., Lu, S., Dong, M., et al. (2016). Structure of the voltage-gated calcium channel Cav1.1 at 3.6 Å resolution. *Nature*, *537* (7619), 191–196.

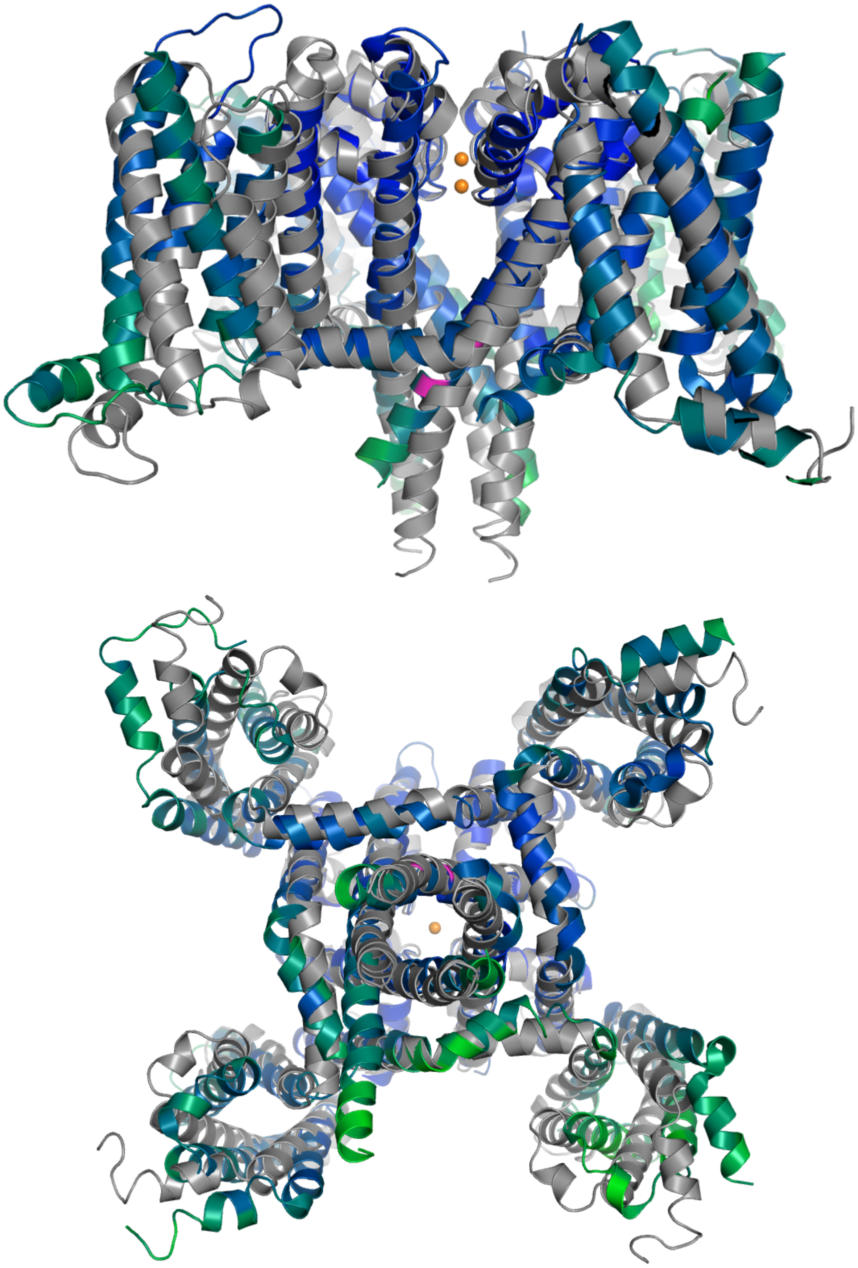

Figure 6.2: Transmembrane alignment of rCav1.1 and CavAb. CavAb and rCav1.1 (PDB 5GJW) transmembrane portions align quite well, when aligned by the pore domain. *Top:* View from the membrane. *Bottom:* View from the intracellular side shows slight difference in positions of the voltage-sensing domains. rCav1.1 α1 subunit colored in blue and green, CavAb-d27 D219G colored in grey. Ca$^{2+}$ ions from the rCav1.1 structure colored in orange spheres. Intracellular and extracellular domains removed for clarity. Pink residues are position of Timothy Syndrome mutations on DI S6.

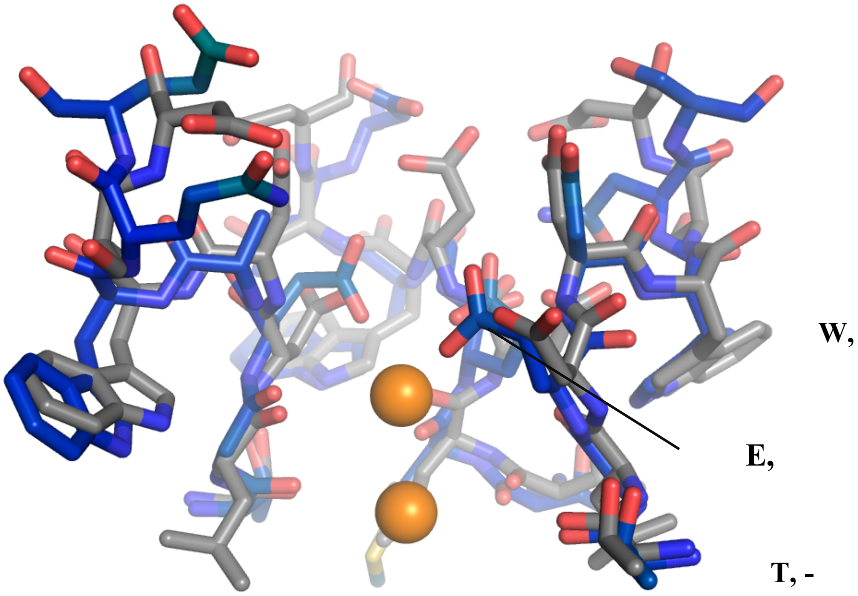

**Figure 6.3: Selectivity filter alignment of rCav1.1 and CavAb.** Backbones of the residues threonine -4 to tryptophan 0 of the selectivity filter align well. Catalytic EEEE motif has been modeled to point more towards the center of the pore than the equivalent DDDD motif in CavAb. rCav1.1 shown in blue, CavAb in grey. $Ca^{2+}$ ions from rCav1.1 structure shown in orange spheres. DIII omitted for clarity.

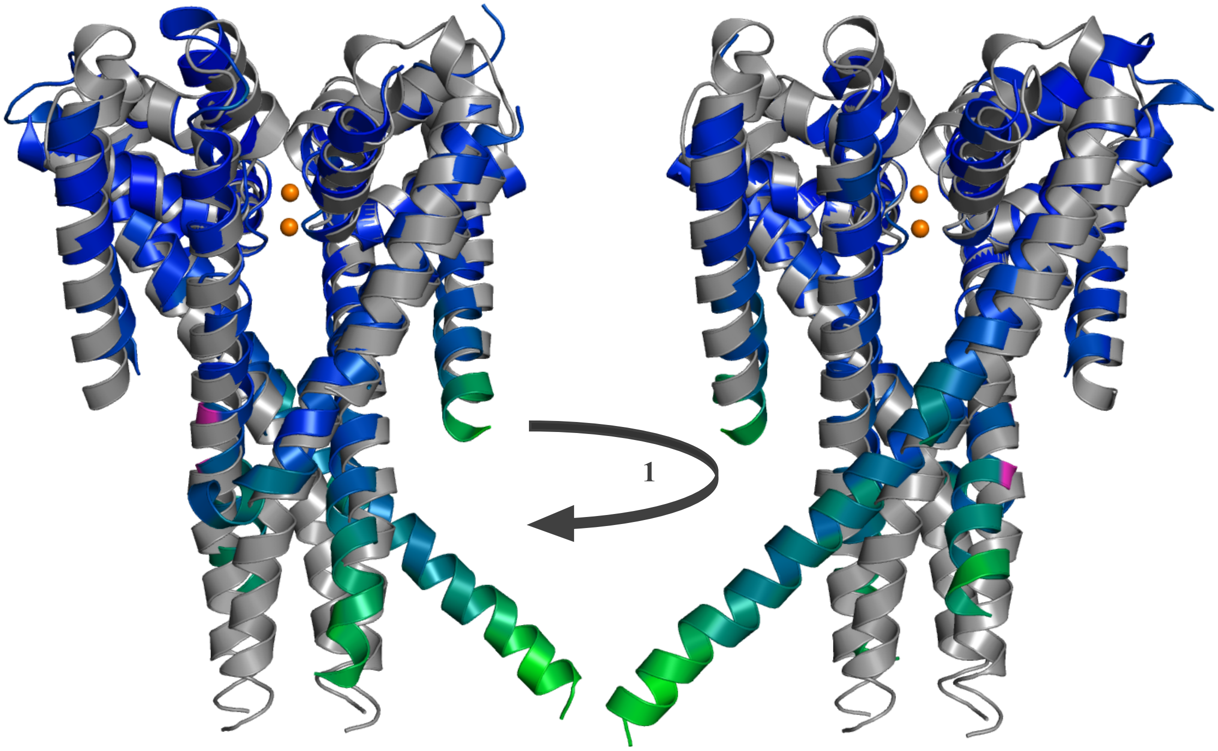

**Figure 6.4: Pore domain alignment of rCav1.1 and CavAb.** Pore structures of bacterial and mammalian structures show large similarities, which diverges when analyzing the bottom of the S6 helices. The largest deviation is seen in DIV S6, as seen by the large helix bent out to the side. rCav1.1 α1 subunit colored in blue and green, CavAb-d27 D219G colored in grey. $Ca^{2+}$ ions from the rCav1.1 structure colored in orange spheres. Voltage-sensing, intracellular and extracellular domains removed for clarity. Pink residues are position of Timothy Syndrome mutations on DI S6.

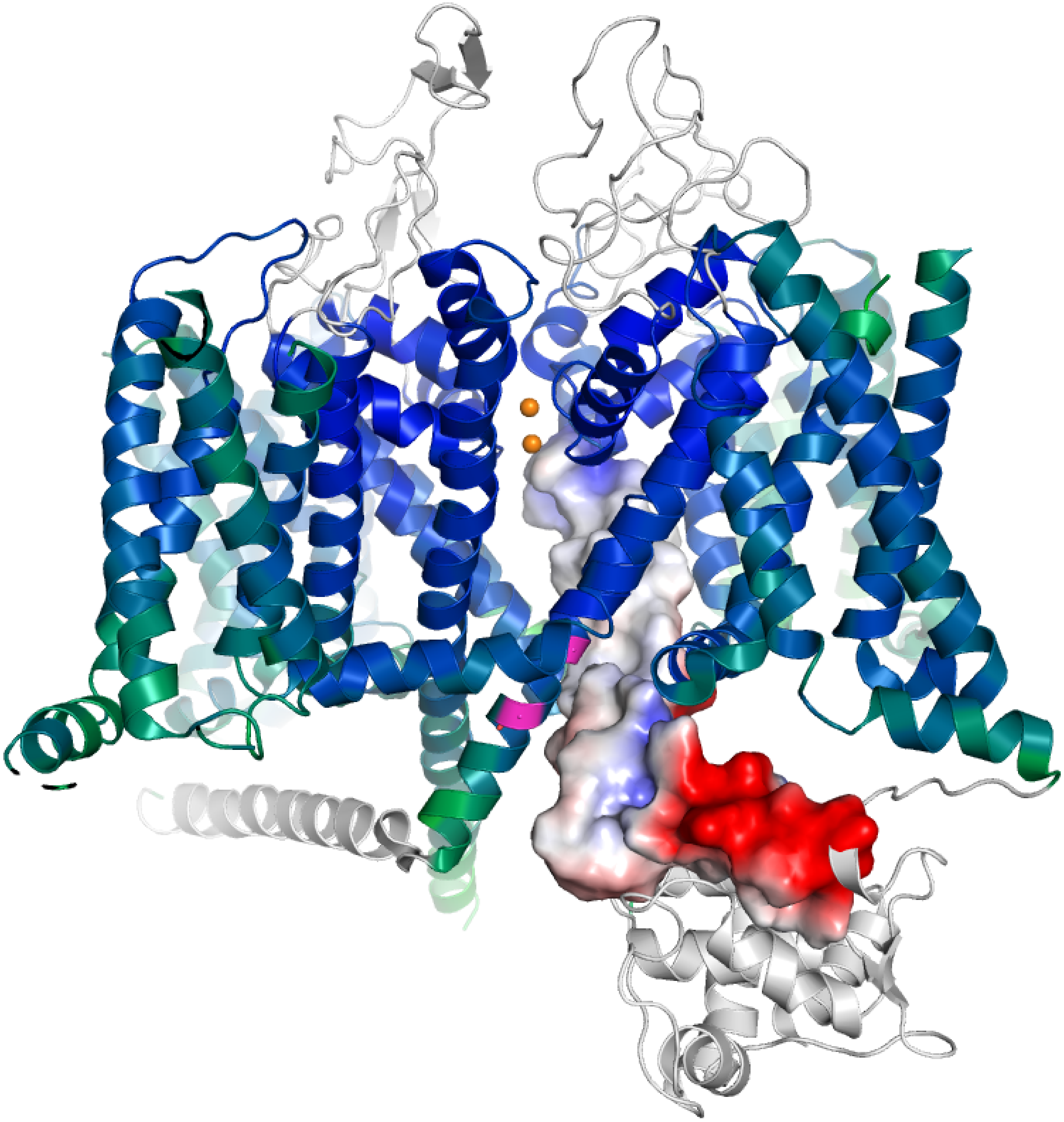

**Figure 6.5: Activation gate of rCav1.1.** Positions of Timothy Syndrome mutations (pink) may interact with DIV S6 helix (surface electrostatic representation) when the channel opens. rCav1.1 α1 subunit colored in blue and green, intracellular and extracellular domains colored in white. $Ca^{2+}$ ions colored in orange spheres.

# 7 Appendices

## 7.1 MATERIALS AND METHODS

### *7.1.1 CavAb expression and purification*

Mutations and truncations of CavAb were made using the site-directed mutagenesis QuikChange method (Invitrogen). Truncations were accomplished by mutating desired position to a stop codon. Baculovirus containing the gene of interest was made by the Bac to Bac system (Invitrogen). Adherent *Trichoplusia ni* ovarian cells, Hi5 cells (Invitrogen), were infected for 72 hours with baculovirus for CavAb-FLAG fusion protein expression. CavAb mutants were purified by FLAG affinity chromatography using buffer containing 10 mM Tris pH 8.0, 100 mM NaCl and 0.12% digitonin (CalBioChem). Concentrated protein of ~16-24 mg/mL was mixed in a 1:5 ratio with CHAPS/DMPC bicelles for a final protein concentration of ~2 mg/mL. CavAb/bicelle mix stored at 4°C. For drug binding experiments, all phenylalkylamines were ultimately dissolved in DMSO and mixed with protein before addition to bicelles at concentrations appropriate for desired dilutions.

### *7.1.2 Bicelle Preparation*

Mix 2.5% (w/v) CHAPS detergent with 10 mM Tris pH 8, 100 mM NaCl buffer. Mix .075g DMPC lipid with 1mL detergent/buffer solution and invert overnight at 4°C. The next day, warm to room temperature and cool to 4°C repeatedly until bicelle solution until clear. Store at 4°C. Warm/cool at least three times (or until clear) before mixing with protein.

### *7.1.3 Protein crystallization*

Crystals of all CavAb constructs were grown at 4°C by hanging drop vapor diffusion method. Protein/bicelle solution was mixed 1:1 with well buffer which contained 100mM sodium acetate pH range 4.6-5.4 (Hampton Research) and ammonium sulfate (Hampton Research) concentration of 1.7-2.4 M. Phenylalkylamines were not added to well buffer. Crystals were cryo-protected in a stepwise manner, initially being transferred to a solution of 100 mM sodium acetate pH 4.8, 2.0 M ammonium sulfate and 6% glucose for at least 10 minutes. Crystals were further transferred to solutions of 12, 18, 24 and 30% glucose for at least 10 minutes each. Phenylalkylamines or ions were added to all cryo-protectant solutions at their final concentrations. Protected crystals were dunked in liquid nitrogen and directly placed in storage pucks.

### *7.1.4 Data collection and structure determination*

Crystal data sets were collected at beamlines 8.2.1 and 8.2.2 at the Advanced Light Source at the Lawrence Berkeley National Laboratory and beamline 19ID at the Structural Biology Center at the Advanced Photon Source at Argonne National Laboratories. Indexing, integration and scaling of reflections was done with the HKL2000 software (Otwinowski et al, 1997). Molecular replacement and refinement were done in the PHENIX software suite (Adams et al, 2002) and protein models were manually adjusted in COOT (Emsley et al 2010). Successive rounds of refinement and manual adjustment were done until acceptable R factors were achieved. PyMol (Schrodinger, LLC) was used to analyze structures and design figures.

## 7.2 DRUG STRUCTURES

### *7.2.1 Phenylalkylamines*

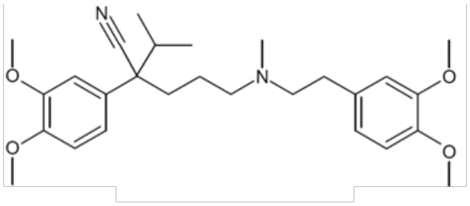

Verapamil

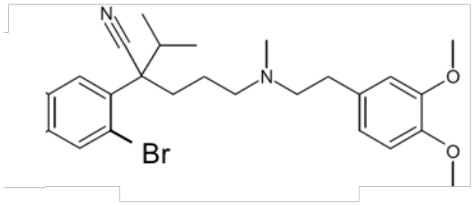

Bromoverapamil

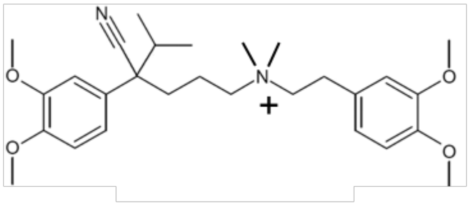

D890

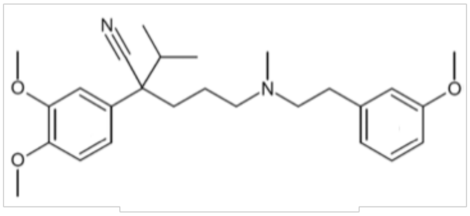

D888 - Devapamil

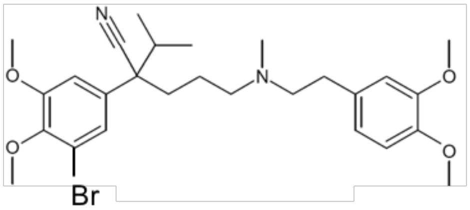

Bromoverapamil A

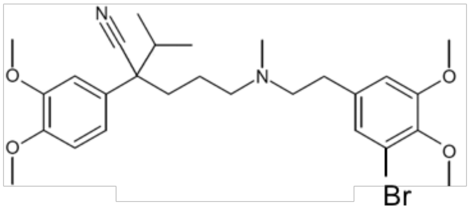

Bromoverapamil B

### *7.2.2 Dihydropyridines*

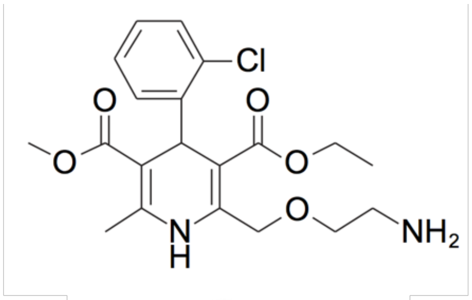

Amlodipine

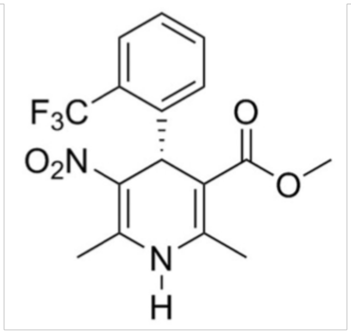

± BayK8644

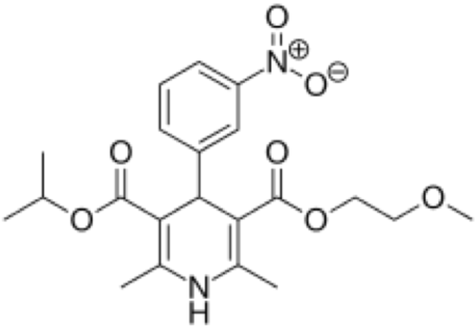

Nimodipine

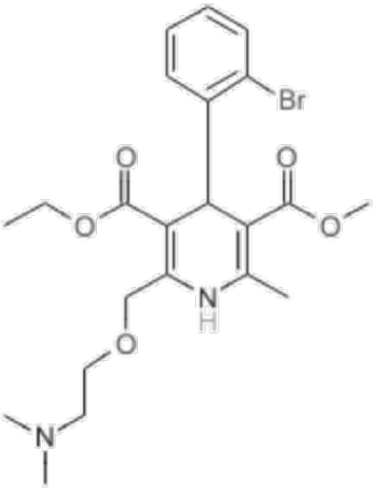

UK-59811

### 7.2.3 *Benzothiazepines*

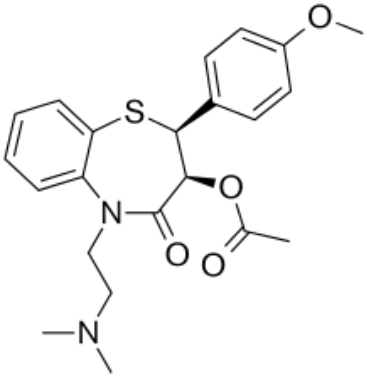

Diltiazem

### 7.2.4 *Other Compounds*

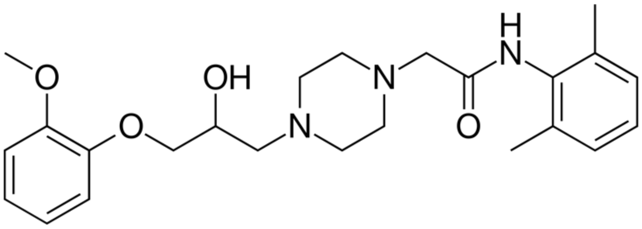

Ranolazine

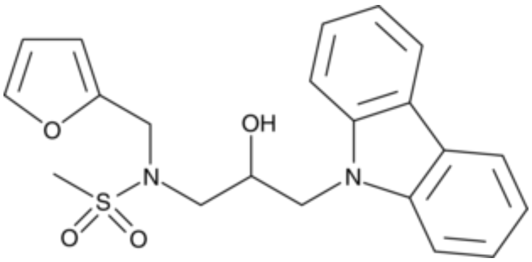

KL001

## 7.3 DATA DOCUMENTATION

All data sets collected are recorded in the data tables found on the hard drives labeled TMSDATA and were collected by myself at a wavelength of 1.0 Å, unless otherwise noted. Published data and/or collected by other colleagues can be found at the end of the relevant chapters. Missing data reflects the fact that not all datasets were refined to completion for a variety of reasons including, but not limited to, insufficient resolution, completeness, or difficult twinning complications. Most data sets were processed and at times refined in multiple space groups to assist in correct space group assignment or to investigate the nature of electron densities along a crystallographic symmetry axis. These tables summarize only the most successful or furthest along refinement attempts for each dataset. Only the most basic information is supplied there.

All crystallographic data, including existing diffraction images as well as processing attempts, can be found on the external hard drive labeled TMSDATA, located in the Catterall Lab. Data is organized in directories by date collected and directory label found in the data tables. Along with the raw data, a more complete spreadsheet is included on the hard drive, which details many more statistics for each data set then shown here. This includes detailed outputs from HKL2000, twinning statistics, molecular replacement, refinement and notes on the protein model in its current state of refinement.

Any additional data collected, but not discussed in this thesis is also documented on the external hard drives.

## 7.4 BIBLIOGRAPHY

Almeida, D. M. (2011). Dockthor: Implementao, Aprimoramento e Validao de um Programa de Docking Receptor-Ligante.

Almers, B. Y. W., & Mccleskey, E. W. (1984). Non-selective conductance in calcium channels of frog muscle: calcium selectivity in a single-file pore, *353*, 585–608.

Almers, W., Mccleskey, E. W., & Palade, P. T. (1984). A non-selective cation conductance in frog muscle membrane blocked by micromolar external calcium ions, *353*, 565–583.

Bader, P. L., Faizi, M., Kim, L. H., Owen, S. F., Tadross, M. R., Alfa, R. W., et al. (2011). Mouse model of Timothy syndrome recapitulates triad of autistic traits. *Proceedings of the National Academy of Sciences*, *108* (37), 1–6. http://doi.org/10.1073/pnas.1112667108

Bagnéris, C., DeCaen, P. G., Hall, B. A., Naylor, C. E., Clapham, D. E., Kay, C. W. M., & Wallace, B. A. (2013). Role of the C-terminal domain in the structure and function of tetrameric sodium channels. *Nature Communications*, *4*, 2465. http://doi.org/10.1038/ncomms3465

Barrett, C. F., & Tsien, R. W. (2008). The Timothy syndrome mutation differentially affects voltage-and calcium-dependent inactivation of CaV1. 2 L-type calcium channels. … *Of the National Academy of Sciences*.

Beneski, D. A., & Catterall, W. A. (1980). Covalent labeling of the Na+ channel with a photoactivable derivative of scorpion toxin.

Berjukov, S., Aczel, S., Beyer, B., Kimball, S. D., Dichtl, M., Hering, S., & Striessnig, J. (1996). Extra- and intracellular action of quaternary devapamil on muscle L-type $Ca^{2+}$-channels. *British Journal of Pharmacology*, *119* (6), 1197–1202. http://doi.org/10.1111/j.1476-5381.1996.tb16022.x

Berjukov, S., Kimball, S. D., Striessnig, J., & Hering, S. (1994). Quaternary devapamil blocks L-type calcium channels from the extracellular side. Naunyn-Schmiedeberg's Arch ….

Bers, D. M. (2002). Cardiac excitation|[ndash]|contraction coupling. *Nature*, *415* (6868), 198–205. http://doi.org/10.1038/415198a

Brauns, T., Cai, Z.-W., Kimball, S. D., Kang, H.-C., Haugland, R. P., Berger, W., et al. (2002). Benzothiazepinone Binding Domain of Purified L-Type Calcium Channels: Direct Labeling Using a Novel Fluorescent Diltiazem Analog. *Biochemistry*, *34* (10), 3461–3469. http://doi.org/10.1021/bi00010a039

Catterall, W. A. (1980). Neurotoxins that act on voltage-sensitive sodium channels in excitable membranes. *Annual Review of Pharmacology and Toxicology*.

Catterall, W. A. (2005). International Union of Pharmacology. XLVII. Nomenclature and Structure-Function Relationships of Voltage-Gated Sodium Channels. *Pharmacological Reviews*, *57* (4), 397–409. http://doi.org/10.1124/pr.57.4.4

Catterall, W. A. (2011). Voltage-Gated Calcium Channels. *Cold Spring Harbor Perspectives in Biology*, *3* (8), a003947–a003947. http://doi.org/10.1101/cshperspect.a003947

Catterall, W. A. (2012a). Voltage-Gated Sodium Channels at 60 : Structure , Function , and Pathophysiology.

Catterall, W. A. (2012b). Voltage-gated sodium channels at 60: structure, function and pathophysiology. *The Journal of Physiology*, *590* (11), 2577–2589. http://doi.org/10.1113/jphysiol.2011.224204

Cheng, R. C. K., Tikhonov, D. B., & Zhorov, B. S. (2009). Structural Model for Phenylalkylamine Binding to L-type Calcium Channels. *Journal of Biological Chemistry*, *284* (41), 28332–28342. http://doi.org/10.1074/jbc.M109.027326

de Magalhães, C. S., Almeida, D. M., Barbosa, H. J. C., & Dardenne, L. E. (2014). A dynamic niching genetic algorithm strategy for docking highly flexible ligands. *Information Sciences*, *289*, 206–224.

de Magalhães, C. S., S Barbosa, dos, C. H., Almeida, D. M., & Dardenne, L. E. (2012). Improving Differential Evolution Accuracy for Flexible Ligand Docking Using a Multi-solution Strategy. In *Intelligent Data Engineering and Automated Learning - IDEAL 2012* (Vol. 7435, pp. 688–698). Berlin, Heidelberg: Springer Berlin Heidelberg. http://doi.org/10.1007/978-3-642-32639-4_82

El-Din, T. M. G., Martinez, G. Q., Payandeh, J., Scheuer, T., & Catterall, W. A. (2013). A gating charge interaction required for late slow inactivation of the bacterial sodium channel NavAb. *The Journal of General Physiology*, *142* (3), 181–190.

Ferry, D. R., Goll, A., Gadow, C., & Glossmann, H. (1984). (–)-3H-desmethoxyverapamil labelling of putative calcium channels in brain: autoradiographic distribution and allosteric coupling to 1,4-dihydropyridine and diltiazem binding sites. *Naunyn-Schmiedeberg's Archives of Pharmacology*, *327* (2), 183–187. http://doi.org/10.1007/BF00500915

Galizzi, D. P., & Borsotto, M. (n.d.). Barhanin, I., Fosset, M. & Lazdunski, M. (1986) Characterization and photoaffinity labeling of receptor sites for the Ca'+ channel inhibitors d-cis-diltiazem, (± .... *J. BioI. Chern*

Galizzi, J.-P., Fosset, M., & Lazdunski, M. (1984). Properties of receptors for the $Ca^{2+}$-channel blocker verapamil in transverse-tubule membranes of skeletal muscle. *The FEBS Journal*, *144* (2), 211–215. http://doi.org/10.1111/j.1432-1033.1984.tb08451.x

Galizzi, J.-P., Fosset, M., & Lazdunski, M. (1985). Characterization of the $Ca^{2+}$ coordination site regulating binding of $Ca^{2+}$ channel inhibitors d-cis-Diltiazem, bepridil and (-)desmethoxyverapamil to their receptor site in skeletal muscle transverse tubule membranes, *132* (15), 49–55.

Hering, S., Hughes, A. D., & Timin, E. N. (1993). Modulation of calcium channels in arterial smooth muscle cells by dihydropyridine enantiomers. *The Journal of General* ....

Hess, P., & Tsien, R. W. (1984). Mechanism of ion permeation through calcium channels. *Nature*, *309* (5967), 453–456. http://doi.org/10.1038/309453a0

Hille, B. (1992). Ionic Channels of Excitable Membranes. Sinauer Associates Incorporated.

Hockerman, G. H., & Johnson, B. D. (1997). Molecular determinants of high affinity phenylalkylamine block of L-type calcium channels in transmembrane domain IIIS6 and the pore region. BIOPHYSICAL ....

Hockerman, G. H., Dilmac, N., Scheuer, T., & Catterall, W. A. (2000). Molecular determinants of diltiazem block in domains IIIS6 and IVS6 of L-type Ca ($^{2+}$) channels. *Molecular Pharmacology*, *58* (6), 1264–1270. http://doi.org/10.1124/mol.58.6.1264

Hockerman, G. H., Johnson, B. D., Abbott, M. R., Scheuer, T., & Catterall, W. A. (1997a).

Molecular determinants of high affinity phenylalkylamine block of L-type calcium channels in transmembrane segment IIIS6 and the pore region of the alpha1 subunit. *Journal of Biological Chemistry*, *272* (30), 18759–18765. Retrieved from http://www.ncbi.nlm.nih.gov/pubmed/9228049

Hockerman, G. H., Peterson, B. Z., Johnson, B. D., & Catterall, W. A. (1997b). Molecular determinants of drug binding and action on L-type calcium channels. *Annual Review of Pharmacology and Toxicology*, *37* (1), 361–396. http://doi.org/10.1146/annurev.pharmtox.37.1.361

Hockerman, G. H., Peterson, B. Z., Sharp, E., Tanada, T. N., Scheuer, T., & Catterall, W. A. (1997c). Construction of a high-affinity receptor site for dihydropyridine agonists and antagonists by single amino acid substitutions in a non-L-type $Ca^{2+}$ channel. *Proceedings of the National Academy of Sciences*, *94* (26), 14906–14911.

Hodgkin, A. L., & Huxley, A. F. (1952a). A quantitative description of memberane potential on sodium conductance in the giant axon of loligo. Journal of Physiology.

Hodgkin, A. L., & Huxley, A. F. (1952b). Currents carried by sodium and potassium ions through the membrane of the giant axon of Loligo. *The Journal of Physiology*.

Hodgkin, A. L., & Huxley, A. F. (1952c). The dual effect of membrane potential on sodium conductance in the giant axon of Loligo. *The Journal of Physiology*.

Johnson, B. D., Hockerman, G. H., Scheuer, T., & Catterall, W. A. (1996). Distinct effects of mutations in transmembrane segment IVS6 on block of L-type calcium channels by structurally similar phenylalkylamines. *Molecular Pharmacology*, *50* (5), 1388–1400. http://doi.org/10.1002/ (ISSN)2052-1707

Kraus, R., Reichl, B., Kimball, S. D., Grabner, M., Murphy, B. J., Catterall, W. A., & Striessnig, J. (1996). Identification of Benz (othi)azepine-binding Regions within L-type Calcium Channel α1 Subunits. *Journal of Biological Chemistry*, *271* (33), 20113–20118. http://doi.org/10.1074/jbc.271.33.20113

Lansman, J. B., Hess, P., & Tsien, R. W. (1986). Blockade of current through single calcium channels by $Cd^{2+}$, $Mg^{2+}$, and $Ca^{2+}$. Voltage and concentration dependence of calcium entry into the pore. *The Journal of General Physiology*, *88* (3), 321–347. http://doi.org/10.1085/jgp.88.3.321

Leblanc, N., & Hume, J. R. (1989). D 600 block of L-type $Ca^{2+}$ channel in vascular smooth muscle cells: comparison with permanently charged derivative, D 890. *The American Journal of Physiology*, *257* (4 Pt 1), C689–95.

Mccleskey, E. W., & Almers, W. (1985). The Ca channel in skeletal muscle is a large pore. *Proceedings of the National Academy of Sciences*, *82* (20), 7149–7153.

McCusker, E. C., Bagnéris, C., Naylor, C. E., Cole, A. R., D'Avanzo, N., Nichols, C. G., & Wallace, B. A. (2012). Structure of a bacterial voltage-gated sodium channel pore reveals mechanisms of opening and closing. *Nature Communications*, *3*, 1102. http://doi.org/10.1038/ncomms2077

Moosmang, S., Lenhardt, P., Haider, N., Hofmann, F., & Wegener, J. W. (2005). Mouse models to study L-type calcium channel function. *Pharmacology & Therapeutics*, *106* (3), 347–355. http://doi.org/10.1016/j.pharmthera.2004.12.003

Nangle, S., Xing, W., & Zheng, N. (2013). Crystal structure of mammalian cryptochrome in complex with a small molecule competitor of its ubiquitin ligase. *Cell Research*, *23*

(12), 1417–1419. http://doi.org/10.1038/cr.2013.136

Navarro, B., Xu, H., Yue, L., Shi, Q., & Clapham, D. E. (2001). A prokaryotic voltage-gated sodium channel. *Science*.

Opie, L. (2001). Calcium channel blockers in hypertension: reappraisal after new trials and major meta-analyses. *American Journal of Hypertension*, *14* (10), 1074–1081. http://doi.org/10.1016/S0895-7061 (01)02215-4

Opie, L. H. (1997). Calcium channel blockers: Summary and safety issues. *Cardiovascular Drugs and Therapy*.

Payandeh, J., El-Din, T. M. G., Scheuer, T., Zheng, N., & Catterall, W. A. (2012a). Crystal structure of a voltage-gated sodium channel in two potentially inactivated states. *Nature*, *486* (7401), 135–139. http://doi.org/10.1038/nature11077

Payandeh, J., El-Din, T. M. G., Scheuer, T., Zheng, N., & Catterall, W. A. (2012b). Crystal structure of a voltage-gated sodium channel in two potentially inactivated states. *Nature*, 1–6. http://doi.org/10.1038/nature11077

Payandeh, J., Scheuer, T., Zheng, N., & Catterall, W. A. (2011a). The crystal structure of a voltage-gated sodium channel. *Nature*, *475* (7356), 353–358. http://doi.org/10.1038/nature10238

Payandeh, J., Scheuer, T., Zheng, N., & Catterall, W. A. (2011b). The crystal structure of a voltage-gated sodium channel. *Nature*, *475* (7356), 353–358. http://doi.org/10.1038/nature10238

Peterson, B. Z., & Catterall, W. A. (2006). Allosteric Interactions Required for High-Affinity Binding of Dihydropyridine Antagonists to CaV1.1 Channels Are Modulated by Calcium in the Pore. *Molecular Pharmacology*, *70* (2), 667–675. http://doi.org/10.1124/mol.105.020644

Peterson, B. Z., Johnson, B. D., Hockerman, G. H., Acheson, M., Scheuer, T., & Catterall, W. A. (1997). Analysis of the Dihydropyridine Receptor Site ofl-type Calcium Channels by Alanine-scanning Mutagenesis. *Journal of Biological Chemistry*, *272* (30), 18752–18758. http://doi.org/10.1074/jbc.272.30.18752

Ptasienski, J., McMahon, K. K., & Hosey, M. M. (1985). High and low affinity states of the dihydropyridine and phenylakylamine receptors on the cardiac calcium channel and their interconversion by divalent cations. *Biochemical and Biophysical Research Communications*, *129* (3), 910–917. http://doi.org/10.1016/0006-291X (85)91978-3

Sather, W. A., & McCleskey, E. W. (2003). Permeation and Selectivity in Calcium Channels. *Annual Review of Physiology*, *65* (1), 133–159. http://doi.org/10.1146/annurev.physiol.65.092101.142345

Shaya, D., Findeisen, F., Abderemane-Ali, F., Arrigoni, C., Wong, S., Nurva, S. R., et al. (2014). Structure of a Prokaryotic Sodium Channel Pore Reveals Essential Gating Elements and an Outer Ion Binding Site Common to Eukaryotic Channels. *Journal of Molecular Biology*, *426* (2), 467–483. http://doi.org/10.1016/j.jmb.2013.10.010

Splawski, I., Timothy, K. W., Decher, N., Kumar, P., Sachse, F. B., Beggs, A. H., et al. (2005). Severe arrhythmia disorder caused by cardiac L-type calcium channel mutations. *Proceedings of the National Academy of Sciences*, *102* (23), 1–8.

Splawski, I., Timothy, K. W., Priori, S. G., & Napolitano, C. (1993). Timothy syndrome.

Splawski, I., Timothy, K. W., Sharpe, L. M., Decher, N., Kumar, P., Bloise, R., et al. (2004).

CaV1.2 Calcium Channel Dysfunction Causes a Multisystem Disorder Including Arrhythmia and Autism. *Cell*, *119* (1), 19–31. http://doi.org/10.1016/j.cell.2004.09.011

Striessnig, J., Grabner, M., Mitterdorfer, J., Hering, S., Sinnegger, M. J., & Glossmann, H. (1998). Structural basis of drug binding to L $Ca^{2+}$ channels. *Trends in Pharmacological Sciences*, *19* (3), 108–115. http://doi.org/10.1016/S0165-6147 (98)01171-7

Striessnig, J., Knaus, H. G., & Glossmann, H. (1988). Photoaffinity-labelling of the calcium-channel-associated 1, 4-dihydropyridine and phenylalkylamine receptor in guinea-pig hippocampus. A 195 kDa polypeptide …. *Biochemical Journal*.

Tang, L., El-Din, T. M. G., Payandeh, J., Martinez, G. Q., Heard, T. M., Scheuer, T., et al. (2014). Structural basis for $Ca^{2+}$ selectivity of a voltage-gated calcium channel. *Nature*, *505* (7481), 56–61. http://doi.org/10.1038/nature12775

Thomas Brauns, Heino Prinz, S David Kimball, Richard P Haugland, Jörg Striessnig, A., Hartmut Glossmann. (1997). L-Type Calcium Channels:  Binding Domains for Dihydropyridines and Benzothiazepines Are Located in Close Proximity to Each Other†. *Biochemistry*, *36* (12), 3625–3631. http://doi.org/10.1021/bi9613584

Tikhonov, D. B., & Zhorov, B. S. (2012). Architecture and Pore Block of Eukaryotic Voltage-Gated Sodium Channels in View of NavAb Bacterial Sodium Channel Structure. *Molecular Pharmacology*, *82* (1), 97–104. http://doi.org/10.1124/mol.112.078212

Tsien, R. W., Hess, P., & Mccleskey, E. W. (1987). Mechanisms of selectivity, permeation, and block. *Annual Review of ….*

Watanabe, E., Fujikawa, A., & Matsunaga, H. (2000). Nav2/NaG channel is involved in control of salt-intake behavior in the CNS. *The Journal of ….*

Wu, J., Yan, Z., Li, Z., Qian, X., Lu, S., Dong, M., et al. (2016). Structure of the voltage-gated calcium channel Cav1.1 at 3.6 Å resolution. *Nature*, *537* (7619), 191–196. http://doi.org/10.1038/nature19321

Wu, J., Yan, Z., Li, Z., Yan, C., Lu, S., Dong, M., & Yan, N. (2015). Structure of the voltage-gated calcium channel Cav1.1 complex. *Science*, *350* (6267), aad2395–aad2395. http://doi.org/10.1126/science.aad2395

Yu, F. H., & Catterall, W. A. (2004). The VGL-chanome: a protein superfamily specialized for electrical signaling and ionic homeostasis. *Science's STKE : Signal Transduction Knowledge Environment*, *2004* (253), re15–re15. http://doi.org/10.1126/stke.2532004re15

Yue, L., Yue, L., Navarro, B., Ren, D., Ramos, A., & Clapham, D. E. (2002). The Cation Selectivity Filter of the Bacterial Sodium Channel, NaChBac. *The Journal of General Physiology*, *120* (6), 845–853. http://doi.org/10.1085/jgp.20028699

Zhang, X., Ren, W., DeCaen, P., Yan, C., Tao, X., Tang, L., et al. (2012). Crystal structure of an orthologue of the NaChBac voltage-gated sodium channel. *Nature, 486* (7401), 130–134. http://doi.org/10.1038/nature11054

Zhou, Y., & MacKinnon, R. (2003). The Occupancy of Ions in the K+ Selectivity Filter: Charge Balance and Coupling of Ion Binding to a Protein Conformational Change Underlie High Conduction Rates. *Journal of Molecular Biology*, *333* (5), 965–975. http://doi.org/10.1016/j.jmb.2003.09.022

## 7.5 VITA

Teresa was a born and bred Midwesterner who received her B.S. in Biochemistry/ Molecular Biology from the University of Wisconsin-Eau Claire before moving to Seattle to pursue her Ph.D. in Pharmacology at the University of Washington. The journey has changed her into a west-coast city slicker with a thirst for change. Her career goals center around the desire to bring scientific knowledge and critical thinking to everyone around her and beyond. She firmly believes that the effective communication of that knowledge is crucial to the future of any scientific endeavors, and society as a whole.

# Publications

Swanson TM, Zheng N, Catterall WA. (2017) Catalytic water molecules in the ion selectivity filter of a voltage-gated calcium channel. In preparation.

Swanson TM, Gamal El-Din TM, Zheng N, Catterall WA. (2017) Conformational change in Timothy Syndrome mutants of a voltage-gated calcium channel. In preparation.

Tang L, Gamal El-Din TM, Swanson TM, Pryde DC, Scheuer T, Zheng N, Catterall WA. (2016) Structural basis for inhibition of a voltage-gated $Ca^{2+}$ channel by $Ca^{2+}$ antagonist drugs. *Nature* 537:117-121. PMID: 27556947.

Catterall WA, Swanson TM. Structural basis for pharmacology of voltage-gated sodium and calcium channels. (2015) *Mol Pharmacol.* 88:141-150. PMCID: PMC4468632.

Tang L*, Gamal El-Din TM*, Payandeh J, Martinez GQ, *Heard TM*, Scheuer T, Zheng N, Catterall WA. (2014) Structural basis for $Ca^{2+}$ selectivity of a voltage-gated calcium channel. *Nature* 505:56-61. PMCID: PMC3877713.

Bandow N, Gilles VS, Freesmeier B, Semrau JD, Krentz B, Gallagher W, McEllistrem MT, Hartsel SC, Choi DW, Hargrove MS, *Heard TM*, Chesner LN, Braunreiter KM, Cao BV, Gavitt MM, Hoopes JZ, Johnson JM, Polster EM, Schoenick BD, Umlauf AM, DiSpirito AA. (2012). Spectral and copper binding properties of methanobactin from the facultative methanotroph Methylocystis strain SB2. *J. Inorg. Biochem* 110:72-82

*“Let us step out into the night and pursue that flighty temptress, adventure.”*

*-Albus Dumbledore*